TECHNOLOGICAL EDUCATIONAL INSTITUTE OF CRETE

SCHOOL OF APPLIED SCIENCES

DEPARTMENT OF ENVIRONMENTAL AND NATURAL RESOURCES ENGINEERING

THESIS

Robust Satellite Techniques (RST) for monitoring possible thermal anomalies related to seismic activity in Greece

Student

Alexandros Eleftheriou

Supervisors/Professor

Dr. Teodosio Lacava

Dr. Nicola Genzano

Prof. Filippos Vallianatos

Chania 2014

Acknowledgments

This work was supported by the THALES Program of the Ministry of Education of Greece and the European Union in the framework of the project entitled "Integrated understanding of Seismicity, using innovative Methodologies of Fracture mechanics along with Earthquake and non-extensive statistical physics – Application to the geodynamic system of the Hellenic Arc. SEISMO FEAR HELLARC".

Dedicated to my Family and Friends

Αφιερωμένο στην Οικογένεια και τους φίλους μου

ACKNOWLEDGEMENTS

Behind these pages, there is the effort of a large number of people that helped me not only fulfill this thesis but also to achieve my current state of knowledge and without them knowing, the influence I got for my way of life. This study was made during my Erasmus Placement in Potenza, Italy, working with the scientific groups from the Institute of Methodologies for Environmental Monitoring (IMAA) and University of Basilicata (LADSAT Laboratory team). I'm glad to have this opportunity to express my sincere thanks for and appreciation of all the assistance that I have received.

I would like to express my deepest gratitude and appreciation to my professors from Technological Educational Institute of Crete – School of Applied Sciences, Department of Natural Resources and Environmental Engineering: Filippo Vallianato, Panteli Soupio, Ilia Papadopoulo, Maria Kouli and all the others that for four years they offered me their knowledge and for giving me the opportunity to fulfill my studies for the last semester in Italy.

I would like to give my sincere thanks to Dr. Vincenzo Lapenna and Dr. Teodosio Lacava who accepted my application for my placement. My deepest gratitude to my supervisor, Teodosio Lacava, that first of all offered me all I needed to have a great stay in Potenza and for his continuous help, advise and inspiration for this study all this time. I'm really grateful. My thanks also go to all the people that we worked together all these months: Dr. Nicola Pergola, Alfredo Falconieri, Francesco Marchese, Giuseppe Mazzeo, Maria-pia Faruolo, Irina Coviello, Valeria Satriano, Emanuele Ciancia and especially Mariangela Liuzzi and Carmine Di Polito, who helped me so much.

I would like to express my sincere thanks and appreciation to Prof. Valerio Tramutoli, for giving me the opportunity to attend his lessons on remote sensing and the summer school in Leicester University, for his guidance in various topics and his hospitality.

I am really thankful to Nicola Genzano, who his help and support, result to fulfil my thesis. His guidance helped me overcome any difficulties and he was always there to answer my questions. My thanks also goes to all the LADSAT team, Carolina Filizzola, Rossana Paciello, Rosita Corrado, Mariano Lisi, Gian Canio Sileo.

Furthermore, I would like to thank my colleagues from TEI of Chania: Maria Charlotte Goniotaki, for giving me the influence to study, who without her support all these years I wouldn't achieve anything. Ntina Orfanou, Mike Konstantakis, George Tsakaloudis, Dimitris Makris, George Kouroumpalis, George Bougioukos, Rafail Antoniou, Vasilis Masmanidis and many others that all these years we exchanged ideas and helped each other. It was a great experience.

Finally, and most important, I would like to express my deepest gratitude to my parents for all their support over the years and for being there whatever I needed. For trusting me and for loving me no matter what.

I'm glad to meet all these people and I consider my stay in Potenza as a journey in knowledge and life experience. Thank you everyone.

Table of Contents

INTRODUCTION

Among natural hazards, Earthquake are one of the most dangerous because they can produce huge disaster in a very short time, without any “evident” warning signal. Mainly for this reason such a phenomena have been largely studied since ancient times. Among the different aspects which characterize the complex system at the basis of Earthquake occurrence, their prediction has been the topic which attracted the attention of many scientists. In this regards, different methods and ‘precursors’ signals have been proposed so far. Up to now, no single measurable parameter and/or no observational methodology have been able to provide useful information to make some kind of possible Earthquake prediction.

Generally speaking, different precursor classes can be defined, for example collecting together all those signals achieved by ground-based measurements, such as seismic wave velocities, seismic electric signals and ground deformation. On the other hand, there are other parameters related to Earthquake occurrence which can be observed by satellite remote sensing techniques, such as electromagnetic phenomena, bathymetry, anomalies in ionosphere, etc.

Among these last ones, also the fluctuations of Earth’s thermally emitted radiation detected by satellite sensors in the thermal infrared (TIR) spectral range have been considered as one of the observable parameter. Although a large number of studies has been performed on this topic since the 80's, sustaining a possible relation between observed thermal anomalies and Earthquake occurrence, the scientific community does not really accept them mainly for the insufficiency of the validation data-sets and the scarce importance related to other causes (e.g. meteorological) that could be responsible, rather than Earthquake activity, of the observed thermal anomalies.

Recently to overcome the above mentioned elements of criticism, a statistical approach named Robust Satellite Technique (RST) has been used as a suitable tool for study the anomalous fluctuation of satellite TIR signals in seismically active areas. By analyzing time series of thermal infrared images acquired by various satellite packages (polar and/or geostationary) this approach has been already tested in different seismically active regions around Earth with various geo-tectonic settings and different Earthquake magnitudes, providing significant results in terms of the presence of an effective relationship between observed TIR anomalies and Earthquake occurrence.

In this study, the RST approach is applied over a long time series of satellite data to investigate Greece, the area with the highest level of seismicity in Europe. In particular, 10 years of data (2004-2013) acquired by the Spinning Enhanced Visible and Infrared Imager (SEVIRI) on board the

Meteosat Second Generation (MSG) satellite have been analyzed looking for possible relationship between TIR anomalies and Earthquake with M≥4. The RST approach has been validated on whole time series of satellite TIR observations, rather than in a short time period (monthly analysis), using pre-established rules (in the space-time domain) in order to find possible relations among the Earthquake occurrence and persistent significant TIR anomalies. In this way, it was possible to evaluate the relations among particular features of TIR anomalies (e.g. space-time extension and intensity) and Earthquake (e.g. magnitude, depth, focal mechanism), in order to obtain more indications about the genetic process of the thermal anomalies associable to seismic events.

The thesis is organized in four chapters.
The first chapter will provide a brief introduction on seismic risk as well as on the state of the art of Earthquake precursors moving from ground-based to satellite-based measurements respectively. Then, the different satellite techniques based on thermal infrared data for Earthquake precursors will be reported in the second chapter, furnishing a detailed description of the RST approach. In the third chapter, the seismicity of Greece will be first presented and then the RST procedure that was followed during the thesis will be discussed step by step. In the last chapter the achieved results will be analyzed and discussed in detail.

Chapter 1

The seismic risk and Earthquake precursors

Earthquake are one of the most dramatic natural hazard that are likely to cause heavy human losses and destroy entire cites on a scale of a minute. This is why Earthquake has been largely studied so far, in an effort to understand each one of the aspects of this phenomenon. In particular, the prediction of seismic events has been one of the topics widely investigated. In this chapter, after a short discussion on Earthquake's nature and the associated hazard, the possible sources of precursory signals will be presented on the basis of their observation type i.e. if it is based on ground or satellite observations.

1.1 The nature of Earthquake

Earthquake is a natural phenomenon that is the result of a sudden release of energy somewhere in the Earth. Before going ahead with the analysis of seismic hazard, in the following, the general aspects concerning the generation of an Earthquake will be briefly summarized.

To better understand the nature of Earthquake (USGS, 2014), it should be stressed that the internal structure of the Earth may be represented as a four layer sphere: the inner core, outer core, mantle and crust (Figure 1.1).

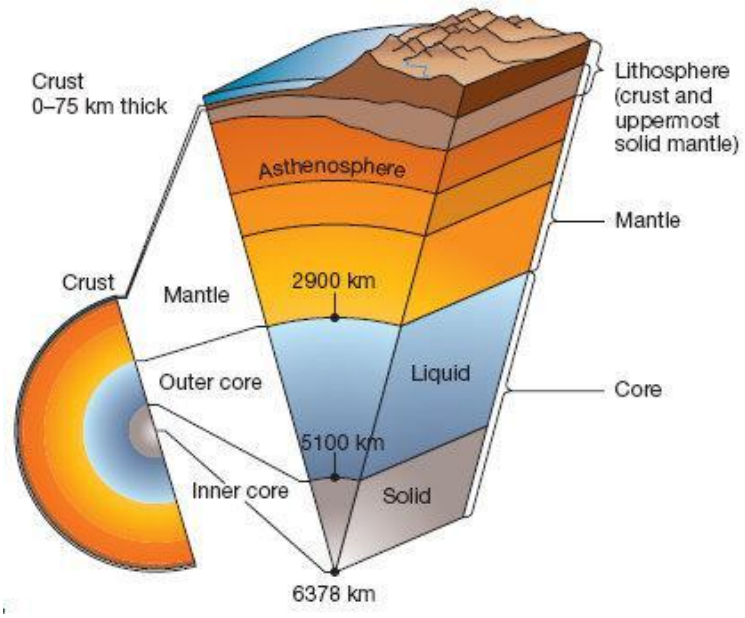

Figure 1. 1 The internal structure of the Earth (USGS, 2014)

The crust and the top of the mantle make up a thin skin on the surface of our planet. This skin is not all in one piece – it is made up of many pieces like a puzzle covering the surface of the Earth which

keep slowly moving around, sliding past one another and bumping into each other. These puzzle pieces are the tectonic plates (Figure 1.2), and the edges of the plates are called the plate boundaries (Figure 1.3).

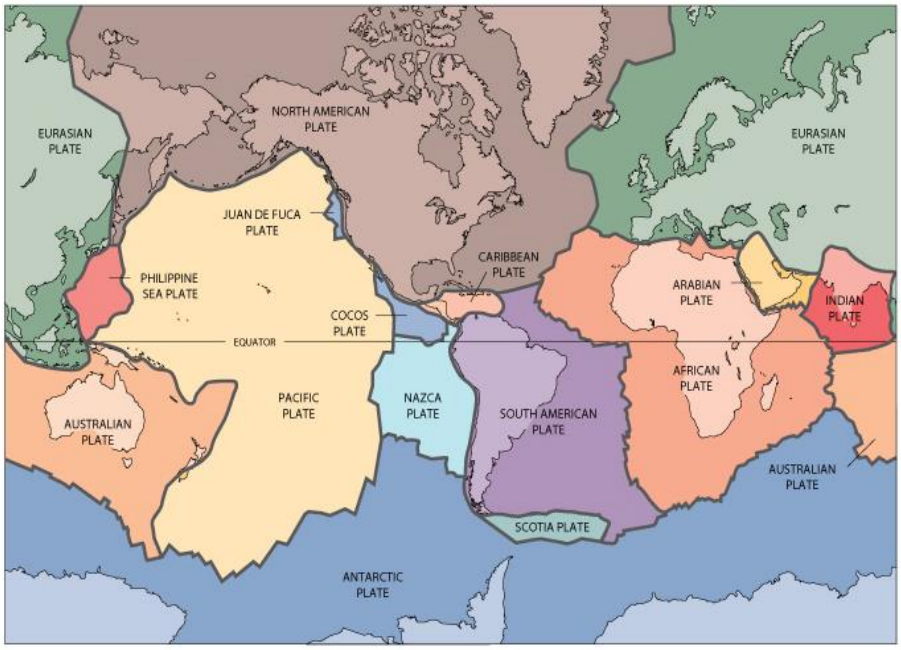

Figure 1. 2 The tectonic plates (USGS, 2014)

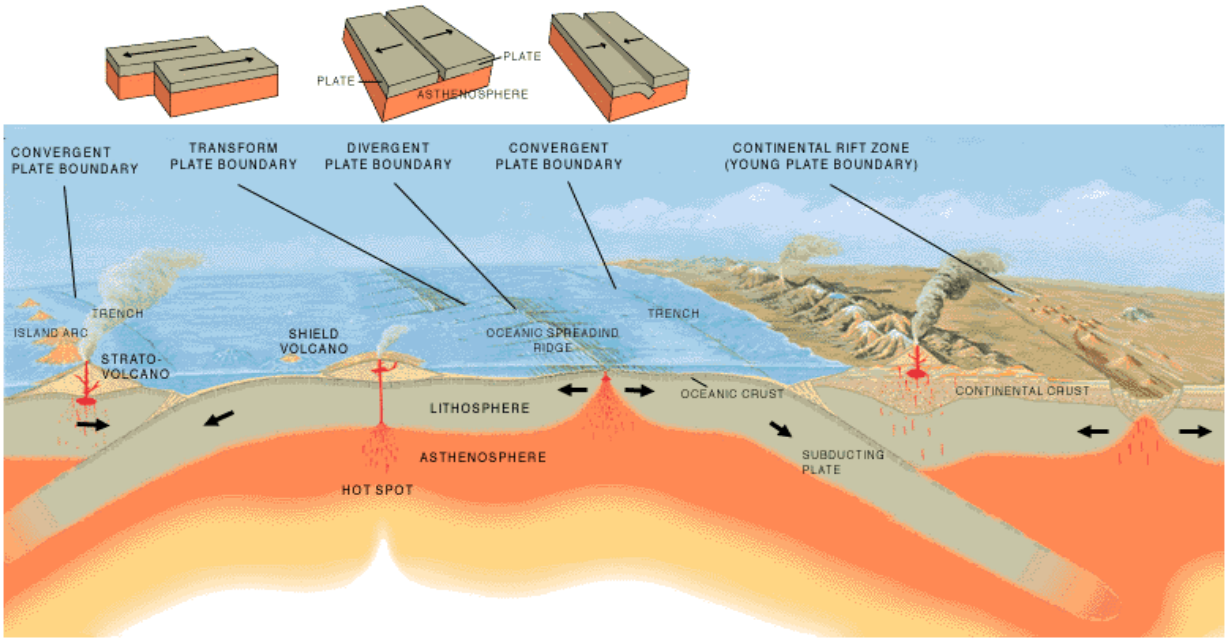

Figure 1. 3 Main types of plate boundaries (USGS, 2014)

The plate boundaries are made up of many faults and most of the Earthquake around the world occurs on these faults. Since the edges of the plates are rough, they get stuck while the rest of the plate keeps moving. Finally, when the plate has moved far enough, the edges unstick on one of the faults and there is an Earthquake. Rupture of rocks, causing an Earthquake, begins at a certain place and spreads on seismic fault with certain speed until it stops. The space that disruption begins may be considered as a point. This point is called micro-seismic foci or micro-seismic hypocenter and the location directly above it on the surface of the Earth is called the epicenter (Papazachos et al., 2005) (Figure 1.4).

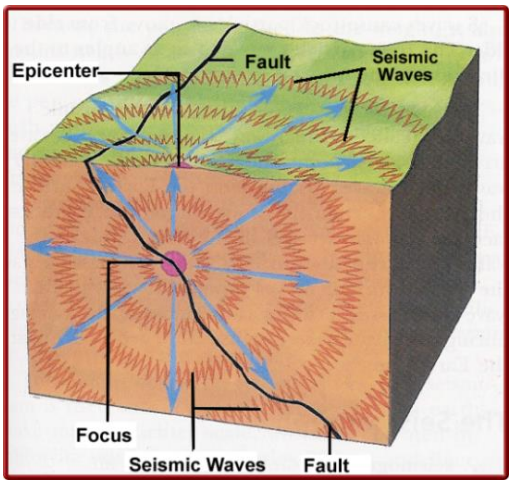

Figure 1. 4 Main elements of an Earthquake

While the edges of faults are stuck together, and the rest of the block is moving, the energy that would normally cause the blocks to slide past one another is being stored up. When the force of the moving blocks finally overcomes the friction of the jagged edges of the fault and it unsticks, all that stored up energy is released. The energy radiates outward from the fault in all directions in the form of seismic waves. Seismic waves are elastic waves that propagate within the Earth. The two main types of waves are, body waves and surface waves. Body waves propagate through the interior of a body. There are two types of seismic body waves: compressional or longitudinal (P-wave), and shear or transverse (S-wave) (Papazachos et al., 2005). Primary waves (P-waves) are compressional waves that are longitudinal in nature. P-waves are pressure waves that travel faster than other waves through the Earth. These waves can travel through any type of material, including fluids, and can travel at nearly twice the speed of S-waves. During propagation of the longitudinal waves in an elastic medium, the particles oscillate in a direction parallel to the direction of propagation of the wave (Figure 1.5).

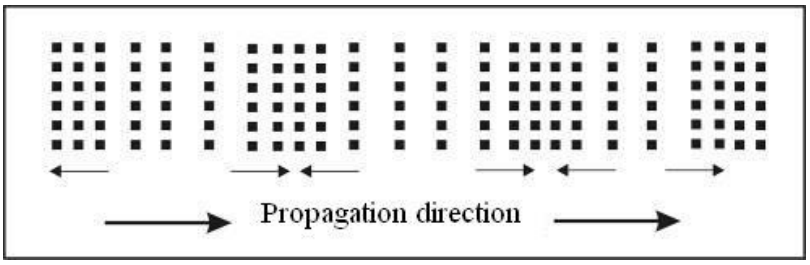

Figure 1. 5 Movements of particles in the longitudinal wave propagation

The velocity of P-waves can be calculated from the elastic constant of material through which the wave is traveling:

$$V_P = \sqrt{\frac{K+\frac{4}{3}\mu}{\rho}} \qquad \text{(Equation 1.1)}$$

Where K is the bulk modulus, μ the shear modulus and ρ is the density.

S-waves, or shear waves, are seismic body waves that shake the ground back and forth perpendicular to the direction the wave is moving. Transverse seismic waves do not propagate in fluids. During propagation of transverse waves in elastic medium, material points oscillate perpendicular to the direction of propagation of the wave, in such a way that the medium gets only shear elastic deformation (Papazachos et al., 2005) (Figure 1.6).

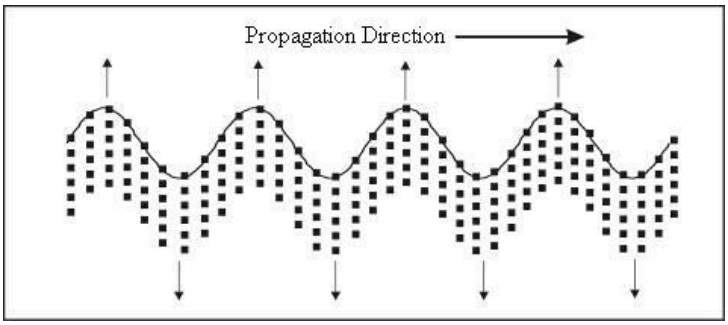

Figure 1. 6 Movements of particles in the transverse wave propagation

The velocity of S-waves is given by the formula:

$$V_S = \sqrt{\frac{\mu}{\rho}} \qquad \text{(Equation 1.2)}$$

Being the elastic constants are all interrelated the Poisson's ratio (ν) can be determined from the P and S wave velocities via the following equation:

$$V_P/V_S = \sqrt{\frac{2(1-\nu)}{1-2\nu}} \quad \text{And} \quad \nu = \frac{Vp^2 - 2Vs^2}{2(Vp^2 - Vs^2)} \qquad \text{(Equation 1.3)}$$

Poisson's ratio theoretically ranges between 0 and 0.5 and for most rocks lies around 0.25, so typically V_P/V_S ratio is about 1.7 (http://appliedgeophysics.berkeley.edu/, 2014).
Seismic properties (V_P and V_P/V_S) of a study area could reflect the properties of rocks, fluid and gas content, and lithology although they are influenced by variations of pressure, temperature, saturation, fluid type, porosity, and pore type in a complex way (Muksin et al., 2013).

The second type of seismic waves is the surface waves that propagate along the surface of a body or along its subsurface interface. There are two types of seismic surface waves: Rayleigh waves and Love waves (both named after their discoverers). Generally, the surface waves are associated with space-time vibration of soil particles "close" on a surface.
Love waves, (SH) are surface waves having a horizontal motion that is transverse (or perpendicular) to the direction the wave is traveling. They are generated under the condition that a layer of finite thickness overlies a half-space (Figure 1.7). Love waves are characterized as the fastest surface waves.

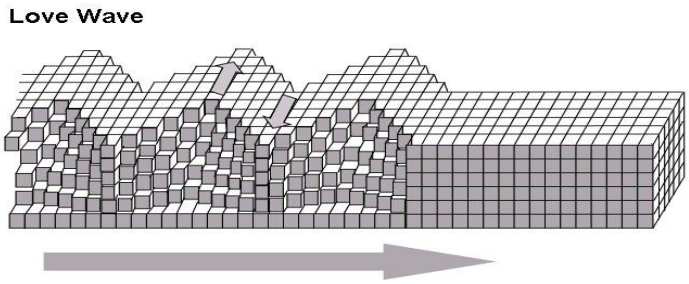

Figure 1. 7 Schematic illustration of Love Waves

Rayleigh surface waves propagate along the free surface of half-space (homogeneous or not), the existence of which is also the basic condition for the creation of such waves. A Rayleigh wave rolls along the ground just like a wave rolls across a lake or an ocean. Because it rolls, it moves the ground up and down and side-to-side in the same direction that the wave is moving (Figure 1.8). Most of the shaking felt from an Earthquake is due to the Rayleigh wave, which can be much larger than the other waves.

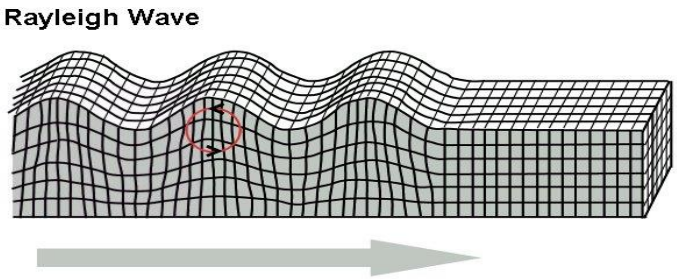

Figure 1. 8 Schematic illustration of Rayleigh Waves

Seismic waves are recorded by instruments called seismographs (Figure 1.9).The seismograph has a base that sets firmly in the ground, and a heavy weight that hangs free. When an Earthquake causes the ground to shake, the base of the seismograph shakes too, but the hanging weight does not. Instead the spring or string that it is hanging from absorbs all the movement (USGS, 2014). The difference in position between the shaking part of the seismograph and the motionless part is what is recorded and reported in a seismogram (Figure 1.10).

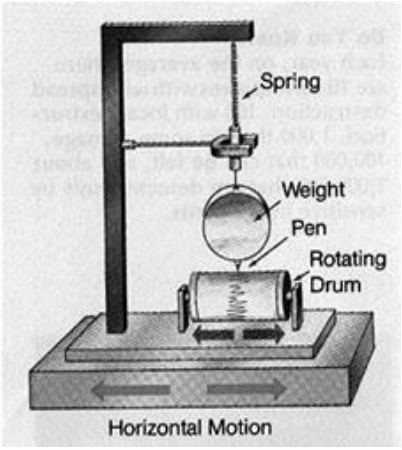

Figure 1. 9 A seismograph

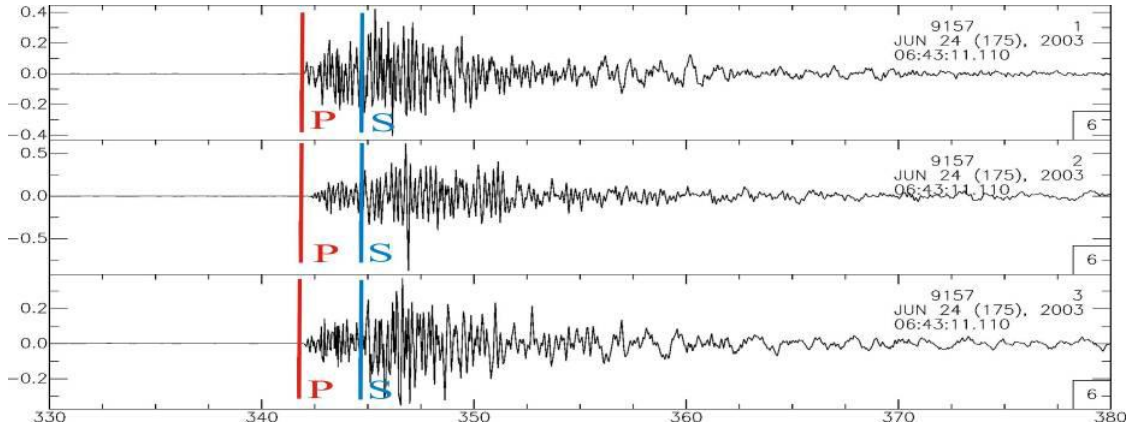

Figure 1. 10 An example of seismogram and identification of P and S waves

There are different ways to classify the power of an Earthquake. Intensity is the rating of the effects of Earthquake vibrations at a specified place (Lee, 2003). Intensity is not based on instrumental measurements but is a rating assigned by an observer using a descriptive scale, with grades from I for not perceptible to XII for total destruction. Magnitude is a quantity intended to measure the size of Earthquake and is independent of the place of observation. Richter magnitude (M_L) was originally defined in 1935 as the logarithm of the maximum amplitude of seismic waves in a seismogram written by a Wood–Anderson seismograph at a distance of 100 km from the epicenter. Empirical tables were constructed to reduce measurements to the standard distance of 100 km, and the zero of the scale was fixed arbitrarily to fit the smallest Earthquake then recorded. Many types of magnitudes exist, such as body-wave magnitude (m_b), surface-wave magnitude (M_S), and moment magnitude (M_W). Earthquake is classified in terms of magnitude (M) as major if $M \geq 7$, moderate if M ranges from 5–7, small if M ranges from 3–5, and micro if $M < 3$. A foreshock is a small Earthquake that occurs shortly before and near a large Earthquake. Mainshock is the largest or principal shock in a sequence of Earthquake and aftershock is an Earthquake that follows a larger Earthquake (a mainshock) and occurs near the larger event. Generally, large Earthquake (magnitude$\geq$6) are followed by many aftershocks that decrease in number and magnitude with time. After the pioneering work of Richter (1935), concerning the concept of Earthquake magnitude, it has been revealed that Earthquake are not uniformly distributed in time, space and magnitude. Distribution of Earthquake with respect to magnitudes exhibits scale invariability which appears to be self-similar and obeys a power law or fractal scaling (Kulhanek, 2005). This implies the absence of a characteristic event size (theoretical limits on the maximum Earthquake size).

An empirical formula,

$\text{Log}N(>M) = a - b*M$ and $N(>M) = 10^a - b*M$ (Equation 1.4)

known as the Gutenberg and Richter (1942) relation, defines the distribution of Earthquake with respect to the magnitude. For a certain region and time interval, this relation, provides the number of Earthquake, N, with magnitude, M, where a and b are positive, real constants. The parameter a, describes the seismic activity. It is determined by the event rate and for certain region depends upon the volume and time window considered. Factor b, known as b-value, is typically close to 1 and is a tectonic parameter describing the relative abundance of large to smaller shocks. It seems to represent geotectonic properties of the seismic medium in some respect, like stress and/or material conditions in the focal region. The relation mentioned above, is usually referred to as the Gutenberg-Richter (G-R) magnitude-frequency relationship (MFR).

1.2 The Seismic Hazard and Risk

Generally speaking seismic risk refers to the risk of damage from Earthquake to a building, system, or other entity. Seismic risk has been defined, for most management purposes, as the potential economic, social and environmental consequences of hazardous events that may occur in a specified period of time. A building located in a region of high seismic hazard is at lower risk if it is built to sound seismic engineering principles. On the other hand, a building located in a region with a history of minor seismicity, in a brick building located on fill subject to liquefaction can be as high or higher risk.
Following the UNESCO recommendations (Unesco, 1972), the risk associated to an Earthquake can be formally defined as:

Seismic Risk = (Seismic Hazard) x (Vulnerability) x (Value) (Equation 1.5)

Where:
- The Seismic Hazard for a particular area is the probability of seismic shaking reaching or exceeding a certain magnitude during a reference period;
- Value is the number of lives or the monetary value of goods at risk in a seismic area;
- Vulnerability is the percentage of lives or goods likely to be lost because of a given seismic event.

It is clear that the seismic hazard is an inherent feature of a specific area and cannot be changed. Ground shaking will vary over an area due to such factors as topography, bedrock type, and the location and orientation of the fault rupture. Hence, to reduce the seismic risk it is fundamental working on the reduction of the Earthquake vulnerability. Humans perceive the Earthquake at the

surface as part of the energy transferred there by the seismic waves. An Earthquake may cause injury and loss of life, road network damage and collapse of buildings. The aftermath may bring disease, despair and panic to the people. The real dangers to people are being crushed in a collapsing building, drowning in a flood caused by a broken dam or levee, getting buried under landslides, or being burned in fires. Among the natural disasters, Earthquake has a great impact on loss of people life. In Table 1.1, the largest yearly Earthquake occurred around the world in the period 1990-2012 are listed.

Table 1. 1 Largest and Deadliest Earthquake (adapted from USGS, 2014)

Largest Earthquakes				
YEAR	DATE	MAGNITUDE	FATALITIES	REGION
1990	07/16	7,7	1621	Luzon, Philippine Islands
1991	04/22	7,6	75	Costa Rica
1991	12/22	7,6	0	Kuril Islands
1992	12/12	7,8	2519	Flores Region, Indonesia
1993	08/08	7,8	0	South of Mariana Islands
1994	10/04	8,3	11	Kuril Islands
1995	07/30	8	3	Near Coast of Northern Chile
1995	10/09	8	49	Near Coast of Jalisco Mexico
1996	02/17	8,2	166	Irian Jaya Region Indonesia
1997	10/14	7,8	0	South of Fiji Islands
1997	12/05	7,8	0	Near East Coast of Kamchatka
1998	03/25	8,1	0	Balleny Islands Region
1999	09/20	7,7	2297	Taiwan
2000	11/16	8	2	New Ireland Region, P,N,G,
2001	06/23	8,4	138	Near Coast of Peru
2002	11/03	7,9	0	Central Alaska
2003	09/25	8,3	0	Hokkaido, Japan Region
2004	12/26	9,1	227898	Off West Coast of Northern Sumatra
2005	03/28	8,6	1313	Northern Sumatra, Indonesia
2006	11/15	8,3	0	Kuril Islands
2007	09/12	8,5	25	Southern Sumatera, Indonesia
2008	05/12	7,9	87587	Eastern Sichuan, China
2009	09/29	8,1	192	Samoa Islands region
2010	02/27	8,8	507	Offshore Maule, Chile
2011	03/11	9	20896	Near the East Coast of Honshu, Japan
2012	04/11	8,6		Off the west coast of northern Sumatra

Within minutes or even seconds of shaking, seismic event reveals the vulnerabilities of a region. Such a catastrophic event has an impact in physical, social and financial components. It is a

phenomenon that cannot be avoided but can consciously be faced. The consequences expose flaws, in governance and planning, construction and land use in Earthquake prone areas. It reveals the influence in culture and way of life, on the capacity of the community to be prepared for an Earthquake hazard. The community has to develop engineering solutions to protect buildings and infrastructure, and improve survival rates as well as provide to the decision-makers vulnerability assessment maps that especially focuses on generating integrated risk scenarios and area-specific prevention measures.

Herein, an integrated system of monitoring should be implemented to try to mitigate Earthquake hazard. The most important element of such a system should be the ability to understand the physical processes progression of such a phenomenon and eventually find precursor signals in order to timely take adequate decisions to avoid big losses. Scientists, in order to detect, that an Earthquake is about to occur (and inform the people that they are going to deal with emergencies that would arise from a potential Earthquake), developed different techniques to identify the signs (i.e. precursors) that indicate the impending event. Make a prediction of an Earthquake means providing an indication that an Earthquake is about to occur in a region within a timeframe and with specified magnitude. According to the prognostic time window (National Academy of Sciences, 1996), it is distinguished as: long-term prediction, referring to a time window of some decades of years, medium-term, referring to a time window of a few years (2-3) and short-term, referring to a time window of the order of up to a couple of months, while sometime the term "immediate" is used when the time window is of the order of a few days. In the next paragraphs the main kind of Earthquake precursor signals will be introduced and discussed.

1.3 Earthquake precursors - A short review

Since 70's an increasing number of scientists started to investigate Earthquake precursors with the final goal to predict strong Earthquake with a sufficient precision (Tsuboi et al., 1962; Whitcomb et al., 1973). An Earthquake precursor is an anomalous phenomenon that might give significant information about an impending seismic activity. The IASPEI Sub-Commission for Earthquake prediction defined a precursor as "*a quantitatively measurable change in an environmental parameter that occurs before mainshocks and that is thought to be linked to the preparation process for this mainshock* (Geller, 1997)".

The implementation of the prediction of a strong Earthquake depends on the capability to observe/measure the appropriate precursors before its occurrence. These precursors must convey or

must be capable of providing, probably after appropriate processing, at least one of the prognostic parameters of the pending Earthquake (Thanassoulas, 2007).

Therefore, in the course towards a successful prediction, it will be necessary to use different types of precursors and/or different analyzing procedures, as well as different physical models that will be interrelated, so that a valid prediction may be achieved. Several methods have been applied by different scientists trying to identify impending Earthquake. In the following a brief report will be made in order to summarize these methods for Earthquake precursor analysis.

1.3.1Ground-based measurements

The observation and acquisition of Earthquake data is available through measurements in seismic stations. As already said, the V_P/V_S along with other factors like, the b-value of G-R law, provides determination of the focal parameters of an Earthquake, (i.e. depth, location and time of occurrence). Small-scale laboratory experiments have shown that the ratio of these two velocities, changes when rock is near the point of fracturing. Changes in geophysical parameters as seismic velocity, seismicity and b-value have been proposed as possible Earthquake precursors (Weeks et al., 1978). Several scientists have reported changes in the V_P/V_S ratio before Earthquake (Aggarwal et.al., 1973; Semenov, 1969; Whitcomb et al., 1973; VanWormer et al., 1975), but for a number of Earthquake the search for such changes has been unsuccessful or ambiguous (Allen and Helmberger, 1973; Boore et al., 1975; Lockner et al., 1977). It should be understood that such changes may not occur in all seismic prone areas. In the case of b-values, it is necessary to include a large number of Earthquake in the calculation in order to obtain meaningful results. Laboratory experiments (Brace et al., 1966) show that rock under uniaxial compression undergoes a volume expansion just prior to fracture. This is due to opening or widening of cracks and has been termed dilatancy. Incipient tensile cracks can also be expected to generate prior to complete failure in rock under tension (Anderson and Whitcomb, 1973). Developed in the 1970's, the dilatancy-diffusion theory of Earthquake prediction is based on fluid pressure and micro-cracks within the supporting material. Dilatancy is a term for the increase in the volume of a rock during deformation, it can occur via an increase in pore volume, a change in the crack and pore distribution, and the rotation of grains or micro-fracturing. As reported by Whitcomb et al., (1973), the premonitory effect is due primarily to a decrease in compressional velocity, suggests that pore pressure changes associated with dilatancy may be responsible for V_P/V_S drop observed before some Earthquake. Thus, study of dilatancy might be important in Earthquake prediction because, it changes the V_P/V_S ratio, ground level and ground water level.

As a consequence of continental plate movement, the Earth's surface near active faults deforms before, during and after Earthquake. Crustal deformation can be observed as relative movement of points on the Earth's surface, ground tilt, ground strain and fault slip. Global Position Systems (GPS) can be used to monitor over medium-long period this movement with a high level of accuracy (within 5mm or less), providing information about ground deformation (USGS, 2014). The Earth's surface reveals complex deformations largely studied with geodetic methods (Moreau and Dauteuil, 2013). This deformation results from several processes that act from some seconds to millions of years and over areas ranging from meters to hundreds of kilometers. Such depth deformations are mainly studied at plate boundaries where the strain is very important and where sudden events like Earthquake can have large impacts on humans. Away from plate boundaries, the deformation of the Earth's surface has lower rates and smaller amplitudes, without any dominant process. Several processes (tectonic, atmospheric loading, post-glacial rebound, volcanic inflation/deflation, volcano isostasy, mass transfer due to sedimentation and erosion, Earth tides, ocean tide loading, hydraulic head) can act with their own temporal and spatial characteristics (Biessy et al., 2011). It can be obtained the accurate 3-D displacement of the Earth's surface changes by GPS observations. The changes of the Earth's surface displacement field observed by GPS are the direct response about Earth's interior stress field in the ground. It is important in science research which used ground-based observations to study the changes in crustal stress field and seismic activity (Wang Yong et al., 2011). Monitoring deformation on several years may be significant and provide more information in the study of Earthquake hazard.

A method proposed as seismic precursor analysis is VAN method (named after P. Varotsos, K. Alexopoulos and K. Nomicos). In this method, Varotsos and Alexopoulos (1984a) showed that the electric field variations of the Earth, occurring before Earthquake is measurable and it is based on the detection of seismic electric signals (SES). SES are emitted by rocks under the stress, caused by stress within the Earthquake focus (Varotsos and Alexopoulos, 1984a). The electric field is determined by measuring the potential difference between two electrodes that constitute a line. The two lines (E-W and N-S) allow the determination of the total electric field at the site of a station. Pair of electrodes are buried in the soil at a depth of 2 m and at a distance L, ranging between 30 and 200 m. The potential difference V is measured after amplifying and filtering out frequencies higher than 0.3 Hz and the result is displayed on a strip chart recorder for each line separately. Many hours before an Earthquake the potential difference V of one line (or simultaneously of both lines) shows a variation, that lasts for a time r and then recovers its initial value. The value ΔV of this variation for a line of $L = 50$ m ranges from a few tenths of a millivolt up to 10 mV depending on the station, on the magnitude of the impending Earthquake and on the epicentral distance.

Analyzing the electrical field variations, significant results about the occurrence of Earthquakes can be made (Lazaridou-Varotsos, 2013). A very interesting SES signal claimed, is the one that preceded the Earthquake in East Kythira, in Greece (2006 M=6.9), visible in Figure 1.11. Actually, this signal was recorded by the Athens (ATH) station, for almost 1.5 hours before the Earthquake and lasted for almost the same time after it.

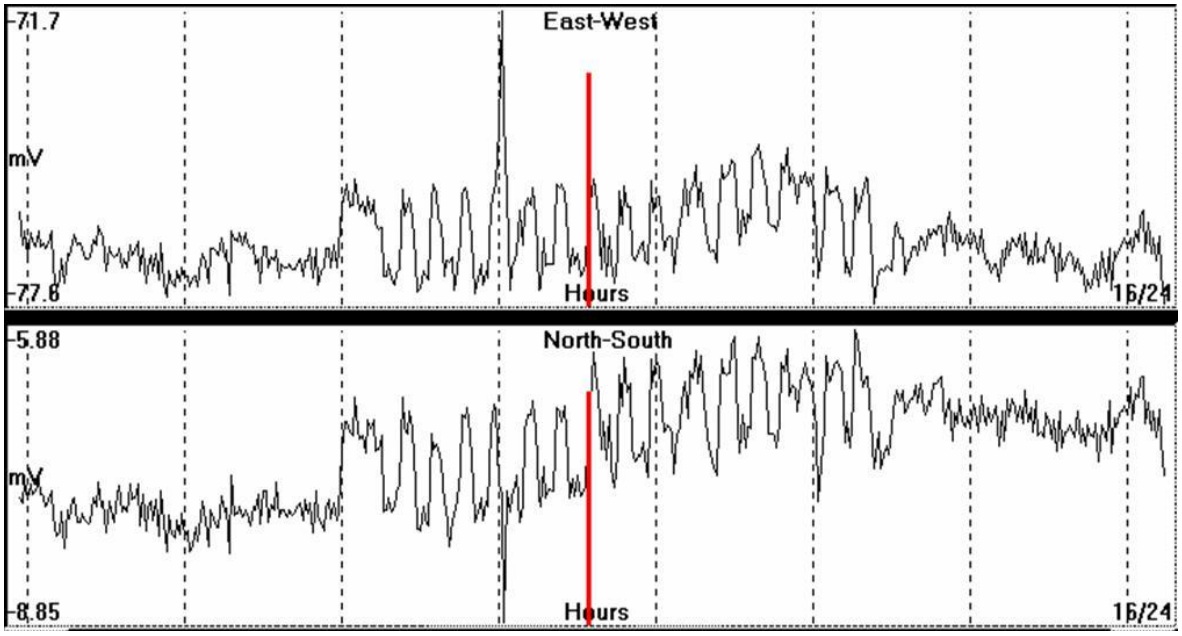

Figure 1. 11 SES recorded by ATH, almost concurrently with East Kythira, Earthquake (red bar, M = 6.9) in Greece (2006)

Lastly, the observation of anomalies in radon (Rn) concentration, in soil gas and ground water before Earthquake initiated systematic investigations on Earthquake precursor phenomena (Singh et al., 2010). Radon emissions have been considered as another Earthquake precursor. The first evidence of a correlation between radon and Earthquake occurrence came from observation of radon concentration in well water, prior to Tashkent Earthquake of 1966 (Ulomov and Mavashev, 1967). Besides being contained in most rocks, it is also radioactive, easily detected and its short-life (3.8 days) makes it sensitive to short-term fluctuations. Walia et al. (2006), monitored radon in soil-gas and groundwater by using the emanometry technique. An emanometer is used to measure the alpha emanation rate from radon in the gas fraction of a soil or water sample by pumping the gas into a scintillation chamber using a closed circuit technique (Ghosh and Bhalla, 1966). This technique gives instant values of radon concentration and is highly suitable for a quick radon survey. In their study (Walia et al., 2006) reported the Uttarkashi Earthquake of 7.0 M_s (m_b = 6.6) with epicenter at 30.78°N,78.80°E occurred on 20th October, 1991, founding an increase of radon concentration just before the event (Figure 1.12).

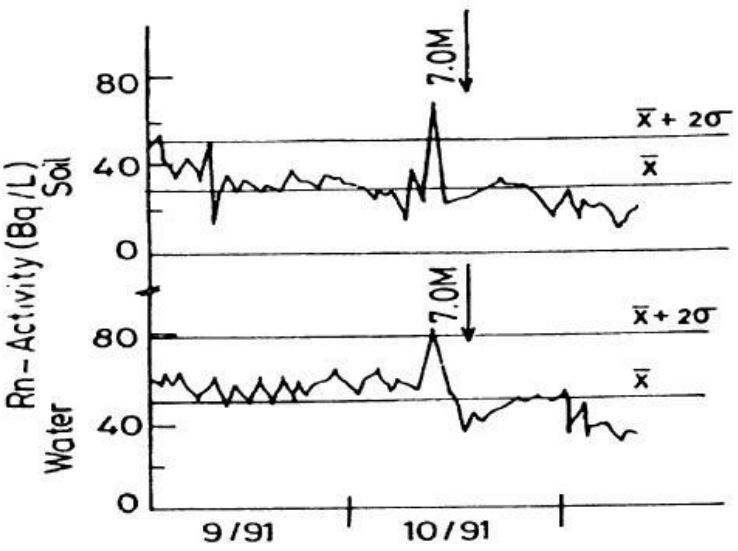

Figure 1. 12 Temporal variations of radon in soil-gas and groundwater recorded from September to October 1991 at Palampur as a precursor to the Uttarkashi Earthquake

As shown, ground-based methods may provide useful information about few signals that, in several circumstances have been recognized as real Earthquake precursors. Main limit of ground-based techniques is that is not possible to cover with a network of specific sensors the whole Earth, and that often the measurement devices risk to be involved by the event itself. This is why, in the last years the use of satellite techniques has grown mainly thanks to specific advantages of these methods respect to the traditional ones, such as the synoptic view and the high sampling frequency with spatial resolution adequate to monitor seismic event. In the following, a brief report will be made in order to summarize the most important satellite techniques that are used today, for Earthquake precursor analysis.

1.3.2 Satellite-based measurements

Satellite measurements acquired in different region of the electromagnetic spectrum can be used to detect Earthquake precursor. Since the ionosphere is a dispersive medium, scientists are able to evaluate the Earthquake ionospheric effect with measurement of the modulations on carrier phases and phase codes recorded by dual-frequency receivers (Leick, 1995). Using ground-based GPS receivers in accordance with a system of satellites is possible to make atmospheric measurements that can have some relation to Earthquake, such as Total Electron Content (TEC) measurements. TEC is an important descriptive quantity for the ionosphere which is characterized by observing

carrier phase delays of received radio signals transmitted from satellites located above the ionosphere. Pre-seismic electric field and its polarity cause the electrons in the F-layer to penetrate to lower layers and therefore, to create anomaly in the ionospheric parameters. The thin layer of particles created before Earthquake due to ions radiation from the Earth has a main role in transferring electric field to above atmosphere and then to the ionosphere (Akhoondzadeh and Saradjian, 2011). TEC is the integrated number of the electrons within the block between the satellite and receiver on the surface. The GPS satellites transmit two frequencies of signals (f_1= 1575.42 MHz and f_2= 1227.60 MHz). The received GPS signals in ground stations contain many effects such as ionosphere, troposphere, instrumental and random errors. Akhoondzadeh and Saradjian (2011) used three different filter methods (interquartile, wavelet and Kalman), to surpass ionospheric disturbances and unknown variations in order to detect pre-seismic anomalies, reporting that continuity in detected anomalies during several hours in each day before Earthquake indicates that observed anomalies with a longer time period is unusual and might be related to impending Earthquake. Their case study was the Earthquake occurred in Haiti (12 January 2010, M_w7.0) and in Samoa Islands (29 September 2009, M_w8.1) and it has been shown that the detected anomalies using all applied methods, can be related to the two strong Earthquake, since the variations of plasma parameters represented by TEC data clearly shows the anomalies a few days prior to Haiti and Samoa Islands Earthquake, over the regions of impending Earthquake.

Liu et al. (2001) using Chung-Li ionosonde[1] measurements (foF2[2]) and a network of GPS receivers for TEC measurements in Taiwan area, found 1–4 days of ionospheric precursors, corresponding to Chi-Chi Earthquake (M_w = 7.7) in Taiwan.

Detection of Electro-Magnetic Emissions Transmitted from Earthquake Regions (DEMETER) is an ionospheric micro-satellite, launched on June 29, 2004 on a polar orbit at an altitude of 710 km. Its scientific payload allows to measure electromagnetic waves and plasma parameters. Electromagnetic phenomena related to Earthquake, might be of a large importance, because some of them are claimed to occur shortly (up to several days) before the time of the main shock and could therefore potentially serve as short-time precursors. Němec et al. (2008) analyzed DEMETER data

[1]An ionosonde is a special radar for the examination of the ionosphere.

[2]F2 layer is the highest region of the ionosphere, extending at night from about 190 to 400 kilometers and during the day from about 145 to 400 kilometers above the Earth. foF2 is the critical frequency of the F2 layer. It is the maximum frequency which can be supported by the F2 layer when a wave is vertically incident upon the layer. It is continuously varying, based on solar activity, and what part of the Earth the Sun is over.

from more than 2.5 years of the satellite observations, altogether representing about 11500 hours of observations organized in about 20000 half-orbits and the USGS catalog, and about 9000 Earthquake with magnitude larger than or equal to 4.8 occurred all over the world, separating the results in two groups respect to the depth of the Earthquake and the day/night time. Finally they statistically demonstrated that a significant decrease in wave intensity is observed in night-time data shortly before the main shock of large surface Earthquake.

Geodetic data, obtained by ground or space based techniques, can be used to infer the distribution of slip on a fault acting during an Earthquake (Massonnet et al., 1993). Synthetic Aperture Radars (SAR) produce all weather and all day, high resolution images of the Earth's surface providing useful information about the physical characteristics of the ground and of the vegetation canopy, such as surface roughness, soil moisture, tree height and bio-mass estimates (NASA, 2014). By combining two or more SAR images of the same area, it is also possible to generate elevation maps and surface change maps with unprecedented precision and resolution. This technique is called SAR interferometry (InSAR). The launch of the ERS-1 satellite in 1991 significantly promoted the development of InSAR techniques and applications. InSAR related research in the 1990s can be grouped into three categories: deformation mapping, DEM generation, and landscape characterization. InSAR was first applied to map the ground surface displacement caused by the 1992 Landers Earthquake (Massonnet et al., 1993). Using a pair of SAR images, one before the Earthquake and the other after the Earthquake, early research focused on mapping the co-seismic deformation with InSAR. Surface displacement data are extraordinarily useful for understanding slip distribution and rupture dynamics during Earthquake, and InSAR has made an indispensable contribution to seismology by providing Earthquake location, fault geometry and rupture dynamics from the measured co-seismic deformation field. In the late 1990s, studies using InSAR to map ground surface deformation immediately after an Earthquake (i.e., post-seismic deformation) yielded important clues to infer the properties of the Earth’s crust and upper mantle (Lu et al., 2007). Radar data also provides information on lineaments[3] due to its oblique look angles. Increase of lineament system evidence during the Earthquake preparation can be determined from time series satellite data in visible (VIS) and infrared (IR) range from systems like Landsat TM/ETM, MODIS, and IKONOS etc. This increase begins 2–3 months before an Earthquake and reaches its maximum about 20 days before it. After an Earthquake the intensity of lineament evidence decreases gradually and after 2-3 months reaches its usual conditions. The possibility of using such an analysis results is based on the assumption that lineament systems in a satellite image are closely connected to the

[3] Lineaments are straight or gently curving features on the Earth’s surface that are commonly expressed topographically as ridges, depressions, or aligned depressions (Shake and McHone, 1986).

systems of seismogenic irregularity and respond to deformation scheme change which is caused by change in Earth's crust stress field (Zoran, 2009). To monitor processes preceding Earthquake, it is better to use imagery having good spatial resolution. Due to such generalization it is possible to see the dynamics of wide lineament zones corresponding to fault systems (Zoran, 2009).

To overcome observational problems like the presence of cloud, fog, snow and rain, which limit mainly observation in the optical band, passive microwave (0.1-100 cm spectral range) systems can be used in order to observe Earth regardless of weather conditions. Besides, the penetrating power of microwave into natural vegetation, artificial camouflage, soil and rock enables microwave remote sensing to detect and discover the target underneath. Fang et al. (2013) reveals that experiments with rock samples in laboratory by quickly loading until the sample fractured, led to the result that the rock's microwave radiant energy varies with pressure. They report also that heat accumulation is formed inside the rock sample after quick loading, resulting in a temperature rise of the sample by 3–6 Kelvin. According to physics laws, material's microwave radiance is an electromagnetic wave radiated when the jump of the molecular rotational level takes place. The prerequisite for the passive microwave remote sensing (PMRS) technology to be used in Earthquake prediction is that mechanical energy excites molecular rotational level to jump. Their study showed that this can be realized by mechanical energy when the material is under the action of a certain mechanical force. As a result, the microwave radiant energy changes with the mechanical force. By using isothermal loading Fang et al., (2013) resulting that the microwave radiant energy of the rock varies sharply with the change of pressure, which proves that the mechanical energy can directly excite the material's molecular rotational level to jump without any intermediate physical process for heat generation. This discovery directly associates the stress with the variance of the material's microwave radiant energy. It is a new promising approach for applying satellite microwave remote sensing technology to the observation of the crustal stress field's distribution, evolution and ground temperature anomaly as well as seismological prediction.

An attempt to use microwave sensors to discover pre-seismic thermal anomalies has been proposed by Saraf and Choudhury (2005) using the data from Special Sensor Microwave Imager (SSMI) onboard of Defense Meteorological Satellite Program (DMSP), near-polar orbiting satellite, were able to observe pre-seismic thermal anomalies (2-10 K of excesses in the measured Brightness Temperatures[4]) in the same week of the Izmit (17 August 1999, M_S=7.8) and of Hindukush (25 March 2002, M_W=6.1) Earthquake and the week before the Kalat event occurred in Pakistan (4 March 1990, M_W=6.1). In their work Saraf and Choudhury (2005) weekly averages of the measured microwave signal were computed and the presence of anomalies evaluated by a simple visual comparison with the mean climatological temperature values computed for the same week in the past 14 years.

Other applications are using anomalous variations of the Earth's thermal emission in relation with Earthquake occurrence. Outgoing Long-wave Radiation (OLR, 4-30 μm spectral range) is the energy leaving the Earth as infrared radiation at low energy into Space. Studying the thermal radiation flux with satellite sensors is possible to analyze the status of the surface temperature variation in the observation region. For example, (Ouzounov et al., 2007) analyzed OLR products, based on NOAA/AVHRR infrared data. The authors using monthly and daily OLR mean values (about six year of data, 1999-2004), studied various seismic events occurred in different part of the world (e.g. Sumatra Earthquake, 26 December 2004, M_W9.0). Calculating the daily zonal OLR anomaly over the epicentral area (1°×1°) and then the zonal mean in the area (10°) over the epicenter, a zonal OLR anomaly was introduced as deviation of the current zonal mean from the multiyear mean zonal values around the Earthquake epicenter resulting to various anomalies prior to different Earthquake (Figure 1.13).

[4] The apparent temperature of the surface assuming a surface emissivity of 1.0. Setting the emissivity to one is equivalent to assuming the target is a blackbody, so the brightness temperature is defined as the temperature a blackbody would be in order to produce the radiance perceived by the sensor. Brightness Temperature is a descriptive measure of radiation in terms of the temperature of a hypothetical blackbody emitting an identical amount of radiation at the same wavelength. The brightness temperature is obtained by applying the inverse of the Planck function to the measured radiation. Depending on the nature of the source of radiation and any subsequent absorption, the brightness temperature may be independent of, or highly dependent on, the wavelength of the radiation (NASA, 2014).

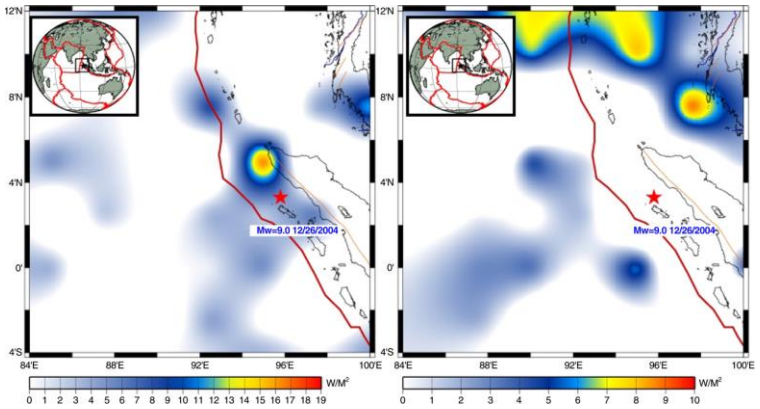

Figure 1. 13 Map of OLR bi-monthly variations for October-November 2004 (a) OLR monthly December 2004 (b) for M9.0 Sumatra Andaman Island, Northern Sumatra of December 26, 2004. Epicenter (3.09N/94.26E) is marked with red star, tectonic plate boundaries with red line and major faults with brown color (Ouzounov et al., 2007)

Guo et al., (2010) used a Wavelet transformation to analyze OLR products of the geostationary satellites Fēngyún, launched on May 2004 and on December 2008 respectively (FY-2C and FY-2E). Studying the Wenchuan (China) Earthquake (12 May 2008, M_S=8.0) and other five Earthquake with $M_S \geq 6$ in the Mainland of China, Guo et al., (2010) report on OLR power spectrum anomaly over areas extended from thousands to ten thousand square kilometers, with a duration of power spectrum amplitude anomaly (relative change rate more than 2 times) between 20 and 80 days (mostly 40~50 days).

Another approach using sensors onboard satellites to identify Earthquake precursors was made by Singh et al., (2006) where remote sensing data of the ocean coasts lying near the epicenters of different Earthquake (e.g. Gujarat, January 26, 2001) analyzed. Singh et al., (2006) analyzed data of ocean parameters choosing Earthquake that differ in proximity of the epicenters to the ocean, tectonic settings and bathymetry. In order to identify Chlorophyll-a[5] (Chl-a) concentration and sea surface temperature (SST), they used satellite data from MODIS level 3 products based on a semi-analytical bio-optical remote sensing algorithm. For analyzing surface latent heat flux (SLHF) they used data from the National Center for Environmental Prediction (NCEP) to study the characteristics of SLHF prior and after the Earthquake (Figure 1.14). Concluding that, the thermal energy released prior to the Earthquake is transported to the surface altering the ambient thermal structure of the water. The latter, results in increase in SST and SLHF and enhances upwelling, which in turns brings nutrient-rich water near the ocean surface giving rise to the Chl-a blooming.

[5]Chlorophyll-a (Chl-a) is the indicator of the primary productivity of phytoplankton biomass in the ocean, which can be monitored from space accurately by ocean color sensors (Sathyendranath et al., 1991).

Anomalous increase in SLHF simultaneously associated with the increase in SST is found due to the buildup of stress in the epicentral regime of an Earthquake.

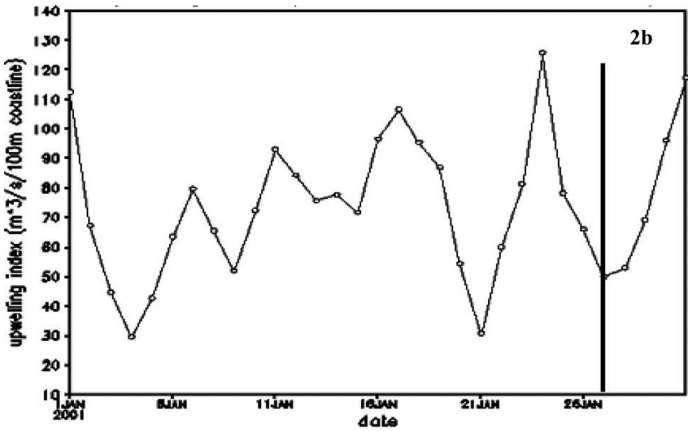

Figure 1. 14 Daily averaged upwelling index for Gujarat Earthquake showing maximum rise three days prior to the main event

More studies have focused on investigating the potential of the thermal infrared (TIR) signals emitted from the Earth to provide Earthquake precursors. Such an approach is at the basis of this thesis, whose main topic is the recognition of possible TIR anomalies and its association as precursors to seismic activity in Greece. In particular, data coming from Spinning Enhanced Visible and Infrared Imager (SEVIRI) in the vicinity of Hellenic Arc onboard Meteosat Second generation (MSG) satellite will be analyzed. To this direction, the next chapter will focus primarly on the origin of TIR signals, moving then to the different approaches used to analyze TIR observations for different regions around the world and finally to the specific application of the method used.

Chapter 2

Thermal infrared data Satellite-based techniques for the Earthquake precursor study

Remote sensing data have demonstrated its promising potential in the field of the Earthquake precursor research. Among the different satellite-based parameters claimed as possible seismic precursors, the fluctuations of Earth's thermally emitted radiation detected by satellite sensors in the thermal infrared (TIR) spectral range have been considered as one of the observable parameter. In this chapter, the fundamental theory, in which based this approach will be firstly described, together with the currently state of art on this topic. After that the advanced techniques used in the frame of this thesis, namely the Robust Satellite (RST) approach, will be introduced. Finally its specific application to SEVIRI-MSG data for Earthquake precursors detection will be presented.

2.1 The origin of Thermal infrared (TIR) anomalies

A number of studies have been performed in the past years using satellite data acquired in TIR (thermal infrared radiation band, 8-14 μm) which indicate the existence of a relation between "anomalous" space-time TIR signal fluctuations (given in units of Kelvin of Brightness Temperature) and Earthquake occurrence.

Generally speaking, the edges of plates boundaries (i.e. fault zones, as in Figure 1.3) can serve as pathways for the seepage of gases (e.g. CO_2, CH_4, Rn) to the surface, formed by changes in permeability of these zones resulting from tectonic movement (Jones and Drozd, 1983). Extensive field works performed by Jones and Drozd (1983) provided information for using geochemical signatures over fault planes as a predictor of tectonic activity. They concluded that faults can serve both as migration paths and as seals. Faults can be compared to a critical orifice that acts as a partial seal, allowing gases to build-up behind the fault zones, but allow leakage to occur when a critical pressure is exceeded. Several models have been proposed to justify a possible relation between anomalous variations of Earth's TIR emission and Earthquake occurrence. The most important are:

- Increased degassing activity particularly for optically active gases like CO_2 and CH_4 (Qiang et al., 1991; Tramutoli et al., 2001, 2005, 2013).

- Near-ground air ionization due to enhanced radon (Rn) emission leading to the condensation of water vapor and, hence, the release of latent heat (Pulinets and Ouzounov 2011).
- Activation of positive-hole pairs in rocks under stress (Freund, 2007a; Ouzounov and Freund, 2004).

Concerning the first model, it is well known that Earth's degassing activity (and particularly of optically active gases like CO_2 and CH_4) is more intense near seismogenic faults (Irwin and Barnes, 1980). Abrupt variations of such gases in near-surface atmospheric layers could result in a local greenhouse effect (Figure 2.1) that increases near-surface temperature and, consequently TIR emission (Qiang et al., 1991; Tramutoli et al., 2001, 2005). The accumulation or the dispersion of gases in the air depends on many factors such as the molecular weight of a gas, the gas emission rate, the morphology of the emission area, the meteorological conditions and the local wind speed. The TIR transients affect areas of several thousand square kilometers and could appear up to several hundred kilometers far away from the Earthquake epicenter zone. Such a spatial distribution is consistent with atmospheric gas dispersion. Moreover, thermal anomalies appear from some days to almost one month before of a seismic event and can last for some time (a few days) afterwards (Tramutoli et al.,2013). When the stress field locally becomes as high as to close the cracks and Earthquake occurrence is approaching, all the above processes (and then the measured TIR emission) are expected to reduce up to the time of Earthquake occurrence. At this time, as a consequence of major cracks opening in the rupture zone, a new increase of degassing activity (and related phenomena) and TIR emission is expected before a gradual return to normality.

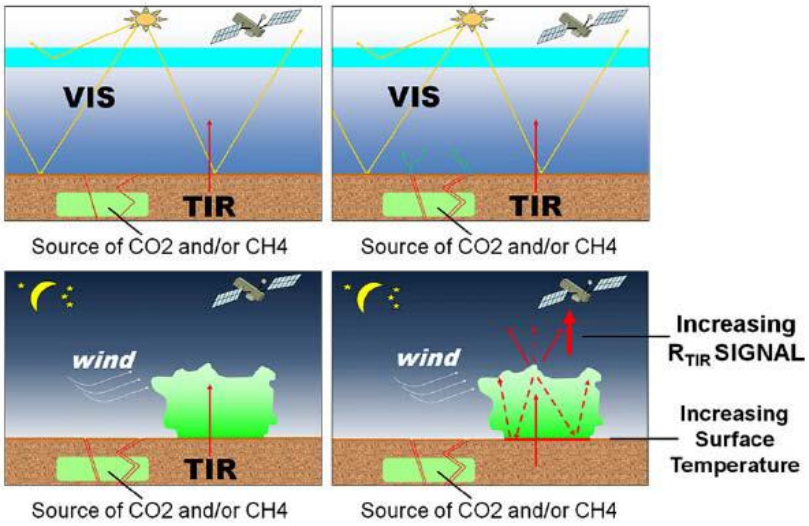

Figure 2. 1 The different phases of the TIR anomaly appearances. In the preparatory phases of an Earthquake, greenhouses gases, like CO_2 and CH_4, can reach the lower part of the atmosphere as consequence of their migrations through the fractures. These can locally operate like greenhouse gases, this way producing an increase of TIR signal which is emitted by the Earth and measured by satellite sensors (adapted from Tramutoli et al., 2013)

Respect to the theory of near-ground air ionization due to enhanced Rn emission, using data analysis in laboratory experiments Freund et al. (2009) described that massive air ionization can take place at the surface of rocks, which are being stressed at one end. The build-up of stress within the Earth's crust prior to major Earthquake may likewise lead to processes at the Earth's surface, including massive air ionization, which can be expected to cause ionospheric perturbations and a host of other phenomena. Another approach explaining the observed atmosphere and ionosphere parameter variations around the time and place of strong Earthquake is using a mechanism that is based on the physical and chemical processes taking place in the atmosphere as a result of action of ionizing radiation by Rn gas over active tectonic faults and tectonic plates boundaries (Pulinets, 2009).

Concerning Freund (2011) positive-hole pairs activation, most crustal rocks contain dormant electronic charge carriers in the form of peroxy defects, ($O_3Si/^{OO}\backslash SiO_3$). When rocks are stressed, peroxy links break, releasing electronic charge carriers, known as positive holes. The positive holes are highly mobile and can flow out of the stressed sub-volume. P-holes are electronic charge carriers normally inactive in rocks, in the form of positive-hole pairs (PHP). When PHPs become activated (e.g. during a rock deformation) they release p-holes, which propagate from the source volume into the surrounding rock. When p-holes arrive at the rock surface, they recombine and release energy, which in turn leads to an enhanced IR emission (Tramutoli et al., 2013).

2.2 Various TIR approaches

As mentioned above, the relation between the occurrence of TIR anomalies and Earthquake has been largely investigated so far. One of the first references in TIR anomaly observations in relation to Earthquake was made by Gorny et al. (1988) who found some short lived thermal anomalies from satellite image before an Earthquake in central Asia.

Generally speaking, the methodologies used for the study of satellite TIR anomalies can be divided in three main approaches, i) the analysis of single TIR image, ii) analysis based on a comparison between TIR imagery and iii) approaches using time series of TIR imagery. In the following the most relevant of these methods are described in detail, while in table 2.1 the list of all the main studies and algorithms for pre-seismic TIR anomalies identification is reported (Genzano, 2014).

Table 2. 1 Main studies and algorithms for pre-seismic TIR anomalies identification. In black color are identify approach based on single image analysis, in green approach based on comparison images methodology and in red approach based on analysis of time-series (Genzano, 2014)

Authors	Satellite/sensors	Thermal Anomaly Definitions/Indices	Reported Anomaly Intensities	Relation with EQ epicenter and time of occurrence		EQ Magnitude	Validation\ Confutation
				Affected area (km^2)	Time-lag		
(Qiang and Dian, 1992; Qiang et al., 1997, 1991, 1992)	MFG/ MVIRI	$\Delta T(x,y,t)=T(x,y,t)-\mu_T(t,H)$	2-10K	100-50k	3 days before	M 5,1 - 7	V
(Huang and Luo, 1992)	NOAA/ AVHRR	$\Delta T(x,y,t)=T(x,y,t)-\mu_T(t,A)$	- - - -	- - - -	- - - -	- - -	C
(Tronin, 1996, 2000; Tronin et al., 2002, 2004)	NOAA/ AVHRR	$\Delta T(x,y,t)=T(x,y,t)-\mu_T(t,H)$	$\Delta T(x,y,t)>2\sigma_T(t,H)$	35k	6–24 days before 7 days after	M 4,7 - 7,3	V
(Xu et al., 2000)	GMS	$\Delta T(x,y,t)=T(x,y,t)-\mu_T(t,H)$	>2K	600k	10 day before	Ms 7,6	V
(Lü et al., 2000)	NOAA/ AVHRR	$\Delta T(x,y,t) = T(x,y,t) - T(x,y,t')$ with $t'<t$	8K	40k	1-2 days before	Ms 6,2	V

(Di Bello et al., 2004; Tramutoli et al., 2001)	NOAA/ AVHRR	$\otimes_{\Delta V}(x,y,m)= \mu_{\otimes}(x,y)$ $V(x,y,t)= T(x,y,t)$ $V(x,y,t)= LST(x,y,t)$	$\otimes_{\Delta V}(x,y,m)$ >0,6 $\otimes_{\Delta V}(x,y,m)$ >1	100k	3 days	Ms= 6,9	
(Aliano et al., 2007, 2008a, 2008b, 2009; Bonfanti et al., 2012; Corrado et al., 2005; Filizzola et al., 2004; Genzano et al.,2007, 2009a, 2009b,; Lisi et al., 2010; Pergola et al., 2010; Tramutoli et al., 2005)	NOAA/ AVHRR MFG/ MVIRI GOES/ IMAGER MSG/ SEVIRI EOS/ MODIS	$\otimes_{\Delta V}(x,y,t)=[\Delta V(x,y,t) -\mu_{\Delta V}(x,y)]/\sigma_{\Delta V}(x,y)$ with $\Delta V(x,y,t)=V(x,y,t)-\mu_V(t)$ $V(x,y,t)=T(x,y,t)$ or $V(x,y,t)=LST(x,y,t)$	$\otimes(x,y,t)>$ 1,5÷4 (space/time persistence required)	100 - 500k	1-25 days before 1-5 days after	Ms 4-7,9	V & C
(Ouzounov and Freund, 2004)	EOS/ MODIS	$\Delta LST(t)=LST_{2002}(d)-LST_{2001}(d)$	4K	30k	1-10 days days before	Ms 7,9	V
(Ouzounov et al., 2006)	EOS/ MODIS	$\Delta LST(t_i)=LST_{RMS}(t_i)-LST_{RMS}$				Ms 6,8 - 7,9	
(Choudhury et al., 2006; Rawat et al., 2011; Saraf and Choudhury, 2004, 2005a, 2005b, 2005c; Saraf et al., 2008, 2009, 2012)	NOAA/ AVHRR	Visual inspection	5-7K	50k-250k	1-10 days before and 2-3 days after	Mw 5,8 - 7,7	V & C
(Yoshioka et al., 2005)	NOAA/ AVHRR	$\Delta T(x,y,t)=T(x,y,t)-\mu_T(t,D)$	4-8K	50k	2/3 days before	Mw 6.8	V & C
(Lixin et al., 2006) (Liu et al., 2007)	NOAA/ AVHRR	visual interpretation	4-5K	80k-920k	1-25 days before and 3 days after	Ms 5,9	V

(Panda et al., 2007)	EOS/ MODIS	$\Delta T(x,y,t)=T(x,y,t)-\mu_T(x,y,t)$	5-10K	111k	7 days before	Mw 7,6	V
(Li et al., 2007)	NOAA/ AVHRR	As (Tramutoli et al., 2005) with V(x,y,t)=LST(x,y,t)	$\otimes(x,y,t) > 1,5\text{-}3$	87k	5 days before	Ms 6,2	V
(Halle et al., 2008)	NOAA/ AVHRR	As (Tramutoli et al., 2005) with V(x,y,t)=LST(x,y,t)	$\otimes(x,y,t) > 2\text{-}3$	2k-5k	2-10 days before and 4-7 days after	M =6,4 -7,8	V & C
(Eneva et al., 2008)	EOS/ MODIS	As (Tramutoli et al., 2005) with V(x,y,t)=LST(x,y,t) and with $\mu_{\Delta V}(x,y)$ and $\sigma_{\Delta V}(x,y)$ computed on 31 days before t	$\otimes(x,y,t) > 2,5\div3,5$	- - - -	20 days before - 20 days after	M 4,5 - 6,6	V & C
(Huang et al., 2008)	EOS/ MODIS	Visual inspection	3-5K	- - - -	1 day before	Ms 8	V
(Ouzounov et al., 2006; Bleier et al., 2009)	EOS/ MODIS GOES/ IMAGE R	$T(x,y,t_i)=T_0+at_i$ ($6pm<t_i<6am$)	a>0	- - - -	1-13 days before	Mw 7,7 M 5,4	V
(Piroddi and Ranieri, 2012)	MSG/ SEVIRI	$<T(x,y,t_i)>=T_0+at_i$ ($6pm<t_i<4am$)		10k	7 days before	Mw 6,3	V & C
(Ma et al., 2010)	EOS/ MODIS	Wavelet transform	4-5K	- - - -	15 days after	M >7	V
(Yang and Guo, 2010)	MTSAT	$\Delta T_{year}(x,y,d)=[T_{year}(x,y,d)-T_{year-n}(x,y,d)]-T_{year}(x,y,d-1)$	4-5K	30k	1-14 days before	Ms 6,2	V
(Zhang et al., 2010, 2011)	FY-2C	Wavelet transform	4-10K	10k-600k	Several days to 2 months before	Ms 7,2-9	V

(Saradjian and Akhoondzadeh, 2011)	EOS/ MODIS	interquartile, wavelet transform and Kalman filter method	1-4K	- - - -	1-20 days before	Mw 6,1-6,6	V
(Zoran, 2012)	EOS/ MODIS	ΔLST(x,y,t)=(LST(x,y,t)-<LST>(t))/LST(x,y,t)	10K	30k	15 days before	Mw 9	V
(Akhoondzadeh, 2013)	EOS/ MODIS	As (Tramutoli et al., 2005) with V(x,y,t)=LST(x,y,t)	$\otimes(x,y,t)>1,5$	- - - -	5 days before	Mw 6.4	V
(Xiong et al., 2013)	ESA/ AATSR	As (Tramutoli et al., 2005)	$\otimes(x,y,t)>2\div4$	- - - -	8 days before	Mw 6.3	V & C

T(x,y,t) = TIR signal measured in correspondence of the geographical coordinates (x,y) at the time t

LST(x,y,t)=LST products computed in correspondence of the geographical coordinates (x,y) at the time t

$\mu_T(t,D)$ = spatial average over a seismically unperturbed zone (D) on the same image

$\mu_T(t,A)$ = spatial average over the same area (A) of punctual air temperature data (from meteorological stations and other sources).

$\mu_T(t,H)$ = spatial average over a selected restrict area (H) on the same image (*cloud-free, seismically unperturbed*)

$\otimes_{\Delta V}(x,y,m)=\mu_{\otimes}(x,y)$ = monthly average of daily RETIRA index $\otimes_{\Delta V}(x,y,t)$

$<T(x,y,t_i)>$= average of $T(x,y,t_i)$ on ten days before

$LST_{RMS}(t_i)$ =the square root of the mean value of the quantity $LST^2(x,y,t_i)$ computed in an area of M×N km^2 (in the considered case 100×100 km^2) centered on the epicenter

LST_{RMS} = temporal average computed on the precedent 60 or 90 days

$T(x,y,t) = T_0(x,y) + a(x,y).t$ is the linear regression function computed on the base of 41 MSG-SEVIRI TIR values (41, 15-min slots between 6pm and 4am) $T(x,y,t_i)$ corresponding to the averages on the previous 9 days where a(x,y) is the coefficient of the linear regression $<T(x,y,t)>$ is the average of $T(x,y,t_i)$ computed for each

$LST_y(d)$=spatial average of the LST(x,y,t) image collected night-time on the day d of the year y over an area of M×N km^2 (in the considered case 100×100 km^2) centered on the epicenter

d=Julian day

Qiang et al. (1992) using Meteosat TIR data and combining meteorological data from ground stations, reported the presence of thermal anomalies a few days before Changsu Earthquake (9 February 1990, Ms=5.1) with an anomalous air temperature increase from the Earth surface up to an altitude of 5.5 km (with a maximum around 1.5 km). In a following study, Qiang et al. (1997) reported an increase of temperature measured by Meteosat from 2-4 °C and 5-6 °C maximum, 3 days before the Earthquake in Datong (18 October 1989, M=6.1). Tronin et al. (2002) used NOAA/AVHRR satellite thermal images to indicate the presence of positive thermal anomalies associated with the large linear structures and fault systems of the Earth's crust. In their study, the relation between thermal anomalies and seismic activity was established for Middle Asia on the basis of a 7-year series of thermal images. They concluded: (a) thermal anomalies appeared about

6–24 days before and continued about a week after Earthquake, (b) anomalies were detectable only for crustal Earthquake with a magnitude more than 4.7, (c) the area affected by the presence of anomaly was about 700 km in length and 50 km in width, (d) the amplitude of the anomaly was about 3°C. In all these studies, the single satellite thermal image was compared with ground information to obtain and identify the anomalies.

The second approach is on the core of satellite-based observations since it requires a comparison, by implementing specific techniques, between satellite thermal imagery acquired before and after the Earthquake. One of these methods was proposed by Ouzounov et al. (2006), using data coming from polar and geostationary satellites. In particular, they used data from MODIS land surface/sea surface temperature (LST/SST) products and Meteosat geosynchronous weather satellites for the study of quite recent worldwide strong Earthquake (e.g. Izmit Turkey, 17 August 1999 Mw=7.8 and Bhuj Gujarat, India 26 January 2001 Mw=7.9). The TIR analysis was performed combining two methods: (a) geo-location and co-registration at sub pixel level of the data to acquire measurements closest to the fault lines and (b) applying the split windows technique (for LST and SST) in the near epicentral area (100 × 100 km) to obtain spatial information (with 1 km pixel resolution) about any surface temperature change prior to the Earthquake. The results they achieved demonstrated that the transient TIR anomalies occurred prior to these Earthquake confirming the earlier findings.
Using the GOES satellite IR Imager data, specifically the long wave IR: channel (10.7–12μm), Bleier et al. (2009) analyzed the infrared environment around the greater San Jose area for the Earthquake at Alum Rock, Ca. (30 October 2007, M=5.4). Three years of historical data were used, to calculate the night time cooling curve of the GOES pixel. Daily mapping of the slope associated to each GOES pixel allow the authors to identify anomalous “apparent heating” during night time (i.e. positive slopes of the nocturnal BT(t) linear function) up to 13 days before the seismic event.
Similarly, Piroddi and Ranieri (2012) studied the case of L’Aquila Earthquake (6 April 2009, Mw=6.3) with MSG-SEVIRI LST products. Using night observations with acquisition frequency of 15 minutes (41 samples of 96 daily available), applying a linear regression they obtained thermal anomalies for those pixels showing positive slope for the nocturnal BT(t) linear function, reporting thermal anomalies quite concentrated (i.e., distance< 100km) around the epicenter during all the 8 days preceding the main shock. Saradjian and Akhoondzadeh (2011a), analyzed LST time series to locate relevant anomalous variations prior to the Bam (26 December 2003, Mw=6.6), Zarand (22 February 2005, Mw=6.4) and Borujerd (31March 2006, Mw=6.1) Earthquake. They used MODIS LST data and implemented interquartile, wavelet transformation, and Kalman filter methods to locate the anomalies. They also used Air Temperature data derived from the meteorological stations

close to the Earthquake epicenters in order to exclude LST data from atmospheric effects. Their results indicate that the highest deviations from a normal state that were regarded as anomaly appeared within the time interval 1–20 days before the Earthquake. They also reported that the detected thermal anomalies can be also related to non-seismic events.

Panda et al. (2007) used MODIS/TERRA LST/E (land surface temperature/emissivity) daytime product to generate time series LST map and temperature difference map, to study the development of thermal anomaly associated with Kashmir Earthquake (8 October 2005, M_w=7.6). LST images were divided into 12 classes, each with 4°C interval and different color. First, the average LST images (normal images) for the selected dates (30 September, 2, 7, 9 and 11 October) was generated using the background data (MODIS LST data from 2000–2004). Then, the average images of the selected dates were subtracted from the images of corresponding dates of 2005 to get the LST difference images with reference to the background data. The thermal anomaly images was divided into five classes with 2°C interval and each class was assigned with distinct color, in this way the spatial thermal anomaly pattern could be better discerned in space and time. They reported that thermal anomalies were identified by simple visual inspection of the LST difference images, affecting a quite large area (about 111000 km2) a week before the Earthquake.

As a summary of this paragraph, it should be stressed that the single image approach has as main advantage, its easily applicability: the only requirement is the availability of just one image which can be compared or not with environmental condition to search for a possible thermal anomaly presence. The method based on comparing more imagery of course needs more efforts, as well as the one analyzing historical series of imagery. This last one, with a level of sensitivity that depend on the applied methodology, should be, in principle, less affected by those signal variations which are related to known but also unknown, natural and/or observational factors (natural/observational noise) which may generate false alarm (Table 2.2), especially when the single image approach is used.

Table 2. 2 Main natural and observational factors affecting TIR signal (adapted from Tramutoli et al., 2005)

Main factors contributing to TIR signal variability	Description
a) Surface spectral emissivity	Quite constant (~0.98) on oceans. Over land it is highly variable taking values within 0.90 and 0.98 mainly depending on soil vegetation
b) Atmospheric spectral transmittance	Depends mainly on atmospheric temperature and humidity vertical profiles
c) Surface temperature (temporal variations)	Related to the regular daily and yearly solar cycles but sensitive also to meteorological (and climatological) factors
d) Surface temperature (spatial variations)	Depend on local geographical (altitude above sea level, solar exposition, geographic latitude) factors
e) Observational conditions (spatial variations)	Variations across the same scene of satellite zenithal angles introduce spatial variations of the registered signal not related to real near-surface thermal fluctuations
f) Observational conditions (temporal variations of satellite view angle)[a]	The same location is observed, at each revisiting time, at a different satellite zenithal angle: this introduces a spurious temporal variation of the measured signal due simply to the change in observational conditions (e.g. air mass)
g) Observational conditions (temporal variations of ground resolution cells)[a]	The change of satellite view angle also determines a sensible change in the size of the ground resolution cell. Spurious temporal variations of the measured signal have to be expected then because of the change in size of the ground resolution cell
h) Observational conditions (variations of the time of the satellite pass)[a]	Satellite pass occurs each day at different times falling in a time-slot up to 3 hours around the nominal time of pass. Spurious variations of the measured signal have to be then expected as a consequence of such (time) variability of observation condition

[a] *Only for instrumental packages onboard of polar satellite (not applicable to geostationary platforms)*

This is why the multi-temporal method has to be preferred. Among them, the Robust Satellite techniques (RST) approach (Tramutoli 2005, 2007), in its first version Robust AVHRR Techniques (RAT, Tramutoli 1998) because initially applied on AVHRR data, has demonstrated the best trade-

off between reliability and sensitivity in detecting possible Earthquake precursors (Tramutoli et al., 2001; Filizzola et al., 2004; Aliano et al., 2008a; Genzano et al., 2007). This is why it has been used in this thesis. In the next paragraph more details on this approach will be provided.

2.3 Robust Satellite Techniques (RST) approach

The RAT approach (Tramutoli, 1998) is an innovative multi-temporal scheme of satellite data analysis proposed to study different natural/environmental hazards (e.g. Earthquake, floods, forest fires, oil spill, volcano, etc.).

This approach considers every anomaly in the space-time domain as a deviation from a "normal" state, which may be determined processing cloud-free satellite records, selected on the basis of specific homogeneity criteria (i.e. same sensor, same geographic area, same spectral channel/s, same recording period, e.g. month and acquisition time). Signal measured by satellite depends indeed on several factors, such as the physical properties of the target and the environmental/observational conditions (e.g. land cover, atmospheric conditions, hour of the day, geometry of observation, illumination). Therefore, if the signal variability in space and time domains is taken into account, actual anomalous events should be more effectively identified. An index named ALICE (Absolutely Llocal[6] Index of Change of the Environment) is then computed by RAT to this aim, and defined in its general mathematical formulation as:

$$\otimes_V (x,y,t) = \frac{[V(x,y,t) - V_{REF}(x,y)]}{\sigma_V(x,y)} \qquad \text{(Equation 2.1)}$$

In this equation V(x, y, t) is the signal measured at time t for each pixel (x, y) of the satellite image to process, $V_{REF}(x, y)$ is the expected value (generally expressed as the temporal mean), and $\sigma(x, y)$ is the natural variability of the signal (i.e. the temporal standard deviation). Thus, higher the ALICE index values, stronger the anomaly intensities. The robustness of such an approach is intrinsic, because a signal will be identified as "anomalous" only if it is higher than its expected value, for a specific condition of observation, and only if this deviation (i.e. the numerator in equation 2.1) is significantly higher than the natural signal variability (i.e. the signal fluctuations observed, in the time series, in absence of any perturbing effect).

[6] The double l will be hereafter used to highlight a reference not only to a specific place r but also to a specific time t' (Tramutoli, 1998).

The RAT approach was renamed RST (Robust Satellite Techniques) by Tramutoli (2005) to better emphasize its applicability to whatever satellite sensor data used.

Among its different applications, RST was applied to seismic hazard analysis and in particular, to isolate possible pre-seismic TIR anomalies from the already cited (Table 2.2) signal variations due to natural and/or observational factors (natural/observational noise).

In the case of TIR anomalies possibly associated to seismic events, the Robust Estimator of TIR Anomalies (RETIRA) (Filizzola et al., 2004; Tramutoli et al., 2005) index $\otimes(r, t')$ was introduced:

$$\otimes (r, t') = \frac{[\Delta T(r,t') - \mu_{\Delta T}(r)]}{\sigma_{\Delta T}(r)} \qquad \text{(Equation 2.2)}$$

Where:

- **r**=(x, y) represents pixel coordinates on satellite image;
  - t' is the time of acquisition of the satellite image at hand, with ($t' \in \tau$) where
  - τ defines the homogeneous domain of satellite imagery collected in the
  - same time (hour) of the day and period (month) of the year;
- **$\Delta T(r, t') = T(r, t') - \langle T(t') \rangle$** is the difference between the current (t=t') TIR
  - signal T(r, t') measured at location **r**, and its spatial average <T(t')>,
  - computed in place on the image at hand, discarding cloudy pixels and
  - considering only sea pixels, if **r** is located on the sea, only land pixels, if **r** is located over the land[7].
- **$\mu_{\Delta T}(r)$ and $\sigma_{\Delta T}(r)$** are the time average and standard deviation values of $\Delta T(r, t)$, at location **r**, computed on cloud-free satellite records belonging to selected homogeneous data-set ($t' \in \tau$).

The $\otimes(r, t')$ index gives the spatial-temporal local (llocal) excess of the current ΔT (**r**, t') signal compared with its historical mean value and weighted by its historical variability at the considered location. Both $\mu_{\Delta T}(\mathbf{r})$ and $\sigma_{\Delta T}(\mathbf{r})$ are computed for each location **r**, processing several years of historical satellite records acquired in similar observational conditions. The excess ΔT (**r**, t') – $\mu_{\Delta T}(\mathbf{r})$ then represents the signal (S) which is to be investigated for its possible relation with Earthquake space-time occurrence. It is always evaluated by comparison with the corresponding

[7] The choice of such a differential variable $\Delta T(\mathbf{r}, t')$ instead of $T(\mathbf{r}, t')$ is expected to reduce possible contributions (e.g. occasional warming) due to day-to-day and/or year-to-year Climatological changes and/or season time-drifts.

natural/observational noise (N), represented by standard deviation, $\sigma_{\Delta T}(\mathbf{r})$. In this way, the intensity of anomalous TIR transients can be evaluated in terms of S/N ratio by the $\otimes(r, t')$ index. Tramutoli et al., (2001) reported that, the use of RETIRA index should highlight the presence of thermal anomalies effectively independent from the known sources of natural/observational noise, also in very low intensity.

2.3.1 Examples of RST application for precursors analysis

The first application of RST technique was made in order to observe seismically active areas in the case of Irpinia-Basilicata Earthquake (23 November 1980, M_s=6.9). Tramutoli et al. (2001) used NOAA/AVHRR imagery from 1994 up to 1998 collected in the same month of the year (November) and close to the same local time of the day (6:00 PM) for building the reference fields (i.e. the temporal mean and standard deviation, $\boldsymbol{\mu_{\Delta T}(r)}$ and $\boldsymbol{\sigma_{\Delta T}(r))}$. Following a procedure of radiometric calibration, imagery co-location, imagery geo-reference and the application of RETIRA index, they showed how the $\otimes(r, t')$ index can reduce the dependence on the elevation and vegetation cover around the area of study (Figure 2.2). Finally they reported (Tramutoli et al., 2001) that RST-TIR anomalies (almost absents in quit-seismic periods) were observed before the occurrence of the Earthquake event.

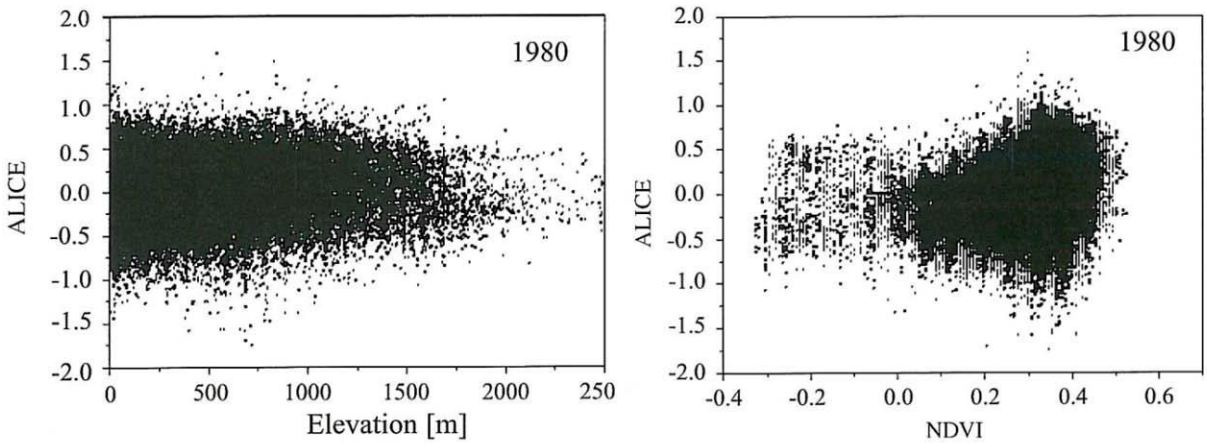

Figure 2. 2 Dependence of RETIRA index on site properties (southern Italy, November 1980). On the left appears the dependence of elevation and on the right the dependence on vegetation cover using NDVI (adapted from Tramutoli et al., 2001)

After this first application, a large number of studies have followed (see references in Table 2.3) where summary of seismic events studied with RST approach is presented.

Table 2. 3 Seismic events studied with the application of RST approach

EVENT (date and magnitude)	RST and references	REFERENCE DATA-SET (sensor, month, years, hour)	S/N ratio
23 November 1980, Irpinia-Basilicata-Italy Ms=6.9	$\otimes_{\Delta T}(x,y,m)$ monthly average (Tramutoli et al., 2001)	NOAA-AVHRR November (1994-1998) 17:00 19:00	0,6
	$\otimes_{\Delta LST}(x,y,m)$ monthly average (Di Bello et al., 2004)		1
7 September 1999, Athens, Greece Ms=5.9	$\otimes_{\Delta LST}(x,y,t)$ daily analysis (Filizzola et al., 2004)	NOAA-AVHRR Aug and Sept (1995-1998) 01:00 04:00	1,5
	$\otimes_{\Delta T}(x,y,t)$ daily analysis (Filizzola et al., 2004)	MFG-MVIRI Aug and Sept (1995-1998) 24:00 GMT	3
17 August 1999, Kocaeli-Izmit, Turkey Ms=7,8	$\otimes_{\Delta T}(x,y,t)$ daily analysis (Tramutoli et al., 2005)	MFG-MVIRI August (1992-1998, 2000) 24:00 GMT	3,5
	$\otimes_{\Delta T}(x,y,t)$ daily analysis (Aliano et al., 2008a)	MFG-MVIRI August (1995-2000) 24:00 GMT	2
28 May 1995 Patras, Greece Mb=4,7			
29 May 1995 Cyprus Mb=5,3			
3 June 1995 Crete, Greece Mb=4,2	$\otimes_{\Delta T}(x,y,t)$ daily analysis (Corrado et al., 2005)	MFG-MVIRI May and June (1992-1999) 24:00 GMT	3
18 June 1995 Crete, Greece Mb=4,3			
4 May 1996			

Erzurum,Turkey Mb=4,3 13 June 1996 Ionian Sea (Southern Greece) Mb= 4.2 16 June 1996 Patras, Greece Mb= 4.3 17 June 1996 Crete, Greece Mb=4.0 29 June 1996 Isparta, Turkey Mb= 5.1			
21 May 2003 Boumerdes Algeria Ms=6,9	$\otimes_{\Delta T}$ (x,y,t) daily analysis (Aliano et al. 2007; 2009)	MFG-MVIRI April and May (1992-1999) 24:00 GMT	3
26 January 2001 Gujarat, India Ms=7.9	$\otimes_{\Delta T}$ (x,y,t) daily analysis (Genzano et al., 2007)	MFG-MVIRI January and February (1999-2004) 24:00 GMT	3
26 September 1997 Umbria- Marche, Italy Ms=5.9 to 6.4	$\otimes_{\Delta T}$ (x,y,t) daily analysis (Aliano et al., 2008b)	MFG-MVIRI September (1992-2000) 24:00 GMT	2
16 October 1999 Hector Mine, California Ms=7,4	$\otimes_{\Delta T}$ (x,y,t)) daily analysis (Aliano et al., 2008a)	GOES (7-9-10) October (1996-1999) 24:00 LT	2,5

23 October 1992 MestiaTianeti, Georgia M=6.3	$\otimes_{\Delta T}$ (x,y,t) daily analysis (Genzano et al., 2009b)	MFG-MVIRI October (1992-1999) 24:00 GMT	3
6 April 2009 Abruzzo, Italy Mw=6,3	$\otimes_{\Delta T}$ (x,y,t) daily analysis (Pergola et al., 2010)	EOS-MODIS March and April (2000-2009) 24:00 GMT	3,5
	$\otimes_{\Delta T}$ (x,y,t) daily analysis (Lisi et al., 2010)	NOAA-AVHRR March and April (1995-2009) 24:00 GMT	3,5
	$\otimes_{\Delta T}$ (x,y,t) daily analysis (Bonfanti et al., 2012; Genzano et al., 2009a;2010)	MSG-SEVIRI March and April (2005-2009) 24:00 GMT	4

Looking at the Table 2.3, it is possible to recognize that RST has been applied in different parts of the Earth, as well as using different satellite packages and signals as well an improvement of S/N ratio through the years is also possible to observe.

Summarizing the achievements of the above applications, it should be stressed that: i) space-time persistence of TIR anomalies is a critical requirement in order to discriminate significant anomalies from residual spurious effects due to simple outliers, geo-location errors or night-time warm cloud shadows (Filizzola et al., 2004; Genzano et al., 2007), ii) an improvement of S/N ratio is possible moving from polar to geostationary satellites, iii) while looking for TIR anomalies related to Earthquake, a threshold of magnitude should be used (i.e. $M \geq 4$) (Tramutoli et al., 2005) and iv) TIR anomalies seems to follow the main tectonic structure and fault system (Genzano et al., 2007; Tramutoli et al., 2013).

Hereafter, the most recent innovative RST approach is implemented following the approach of Genzano, (2014), who applied for the first time a long period analysis over Italy where a few improvements to the standard approach have been done: a) a new robust approach to reduce the cloudy effects has been introduced, b) better identification and discarding of those images that has been identified navigation/co-location error c) the images that has been identified a limited spatial extension of TIR anomalies (i.e. lesser than 10 pixel) have been considered as well as d) those images that has TIR anomalies that are not persistent in space-time domain.

Concerning to this work, that proposed in this thesis further extends its improvements. For the first time, the RST approach has been applied to analyze a long period (2004-2013, ten years) of SEVIRI

data for independently investigate Earthquake precursors occurrence over Greece, the most seismic region of Europe. Besides, a new approach for identifying anomalies/Earthquake correlation has been used, pointing on the anomalies rather than on the epicenter of the Earthquake. In the following chapter, after a brief summary about Greece seismicity, the used approach will be discussed in detail.

Chapter 3

The Hellenic Arc case study

The area investigated in this thesis by implementing the RST approach on SEVIRI data is Greece, the area of highest seismicity in Europe. In this chapter, a description of Greece seismicity will be first provided, followed by a summary of the recent events occurred in the area. Finally the specific implementation of RST to this area will be discussed.

3.1 Seismicity of Greece

The Earth's lithosphere beneath Greece and its vicinity constitutes a broad boundary region between three major tectonic plates, the Eurasia, Africa, and Arabian plates (Figure 3.1). The lithosphere underneath the area also consists of another two microplates, namely the Aegean Sea plate and the Anatolian plate (USGS, 2014). This particular tectonic location makes Greece (i.e. the Hellenic arc and the Aegean) exposed to a large number of Earthquake every year (Bath, 1983).

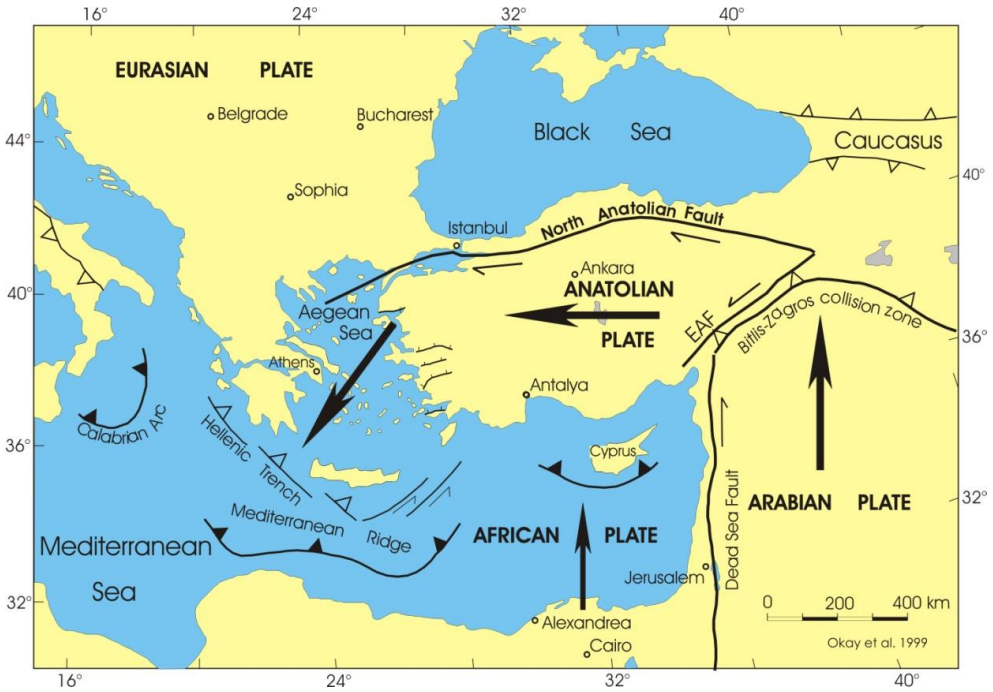

Figure 3. 1 Active Tectonics in East Mediterranean sea, Eurasian plate, Black sea, North Anatolian fault (NAF), Anatolian plate, Arabian plate, Aegean sea, African plate (tectonic movements)

The seismicity of Greece has been evaluated mainly during the 20th century. Based on the historical information available concerning past Earthquake and on the measurements related to recent events, the seismic hazard for Greece has been repeatedly assessed since 1970's, focusing on different

aspects, such as: (a) the spatial distribution of the maximum observed intensity (Galanopoulos and Delibasis, 1972), (b) the maximum expected macroseismic intensity (Papaioannou, 1984), (c) peak ground acceleration (Drakopoulos and Makropoulos, 1983; Papaioannou, 1984), and (d) duration of strong ground motion (Papazachos et al., 1992).

Papazachos et al. (1984), attempted to determine the orientation and other properties of the seismic faults in the Aegean and surrounding area. They concluded that, along western Albania and the western part of Greece a zone of mainly thrust faulting parallel to the coast is present while an area characterized by normal faults is present in eastern Albania-western central Greece (Figure 3.2).

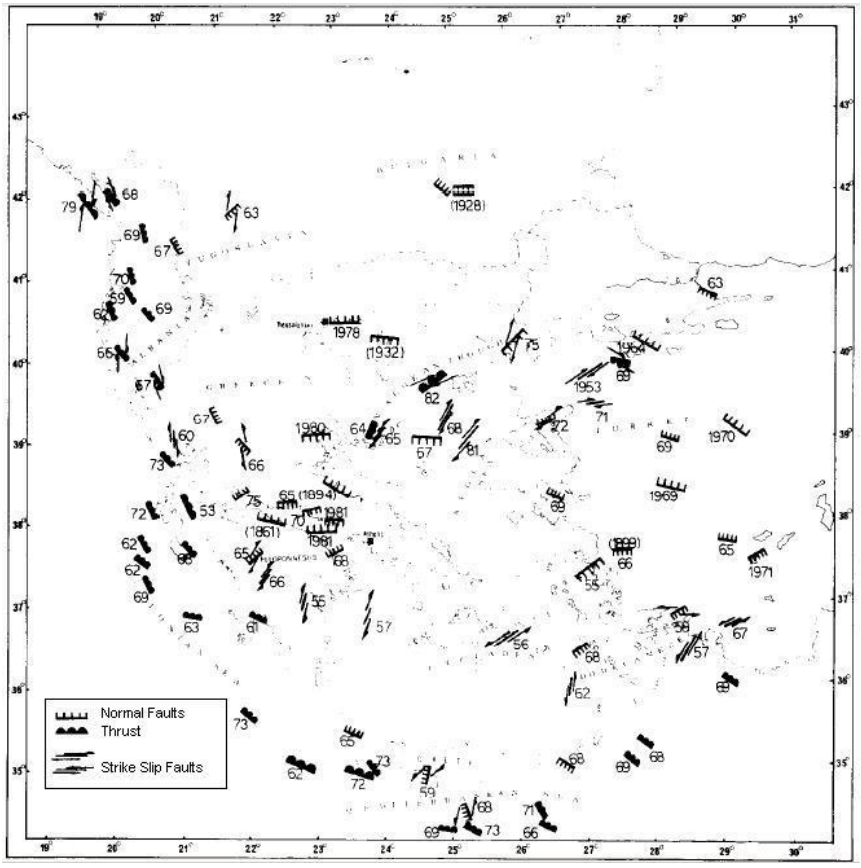

Figure 3. 2 Type of faulting in the Aegean area. The numbers close to each epicenter are the last two digits of the year of occurrence. When the information comes from fault plane solutions and fault traces the whole number of the year is written. Whole numbers of the years in parenthesis mean observations only from fault traces (adapted from Papazachos et al., 1984)

Along the convex side of the Hellenic arc the shallow thrust faults have an almost constant NW-SE strike and the slip vector plunges constantly to NE. This vector is almost normal to the coast in the western part and parallel to the coast in the eastern part. This slip motion is considered as a result of the convergence of the Eastern Mediterranean lithosphere with the Aegean one. They also reported

that, in the southern part of the area (Crete) and just north of the thrust zone, a zone of normal faulting is formed. The slip direction in this zone (SW-NE) is almost parallel to the slip direction in the thrust zone along the convex side of the Hellenic arc. Further north, a zone with strike-slip faulting between central Peloponnesus and southwestern Turkey (Peloponnesus-Cyclades-Dodecanese-southwestern Turkey) was observed.

The slip vector along this zone has the same trend with the slip vector in the thrust zone along the convex side of the Hellenic arc, which shows that this fracture zone is somehow related to the subduction along the Hellenic arc. Central Greece, western Turkey, southern Yugoslavia and southern Bulgaria are dominated by normal faulting with slip vectors oriented in an almost N-S direction (Papazachos et al., 1984).

Another study concerning the seismicity of Aegean and the surrounding area was performed by Papazachos (1990). In that study, the author gave a detailed description of the seismic zones (shallow and intermediate seismic sources). For shallow seismic sources, performed seismic hazard evaluation (i.e. a and b values of the frequency-magnitude relation, maximum Earthquake magnitude, number of shocks larger than certain magnitude per year). In addition for the intermediate seismic sources they provide mean return period, most probable magnitude in a certain time period, moment rate. Papazachos (1990), analyzed instrumental and historical data separated Greece in 36 seismic sources for shallow Earthquake and 6 intermediate depth ones. Resulting that shallow seismicity is highest along the convex side of the Hellenic arc but close to the coast (Ionian Islands, south Peloponnesus, south of Crete, south of Karpathos and Rhodos), in Central Greece (Patraikos-Corinthiakos-Evoikos gulfs, Thessalia) and along a seismic belt which includes the northwestern Anatolia fault zone, the northernmost part of the Aegean Sea and the Serbomacedonia zone. The intermediate depth seismic activity is distributed in two parts of the Benioff zone, which dips from the convex side (Eastern Mediterranean) to the concave side (Aegean Sea) of the Hellenic arc. The one part shows a low dip angle and includes Earthquake with focal depths between 70 km and 100 km. This part has a high seismicity (Earthquake magnitudes up to 8.0) and is situated below the inner slope of the sedimentary part of the Hellenic arc (Eastern Peloponnesus-north of Crete-Rhodos). Based on the fact that this part of the Benioff zone is a continuation of the seismic zone of shallow Earthquake along the Hellenic arc and that both zones have the same seismicity, they concluded that both the areas constitute a continuous seismic belt on which coupling occurs between the subducted eastern Mediterranean lithosphere and the over-thrusted Aegean lithosphere. The other (inner) part of the Benioff zone shows seismicity with a maximum Earthquake magnitude up to7.1, with events of focal depths between 100 km and 180 km. It dips at a mean angle of 38^{o}

below the volcanic arc of the southern Aegean Sea and is the result of the subduction of the front part of the eastern Mediterranean lithosphere without coupling with the Aegean lithosphere (Figure 3.3 and 3.4).

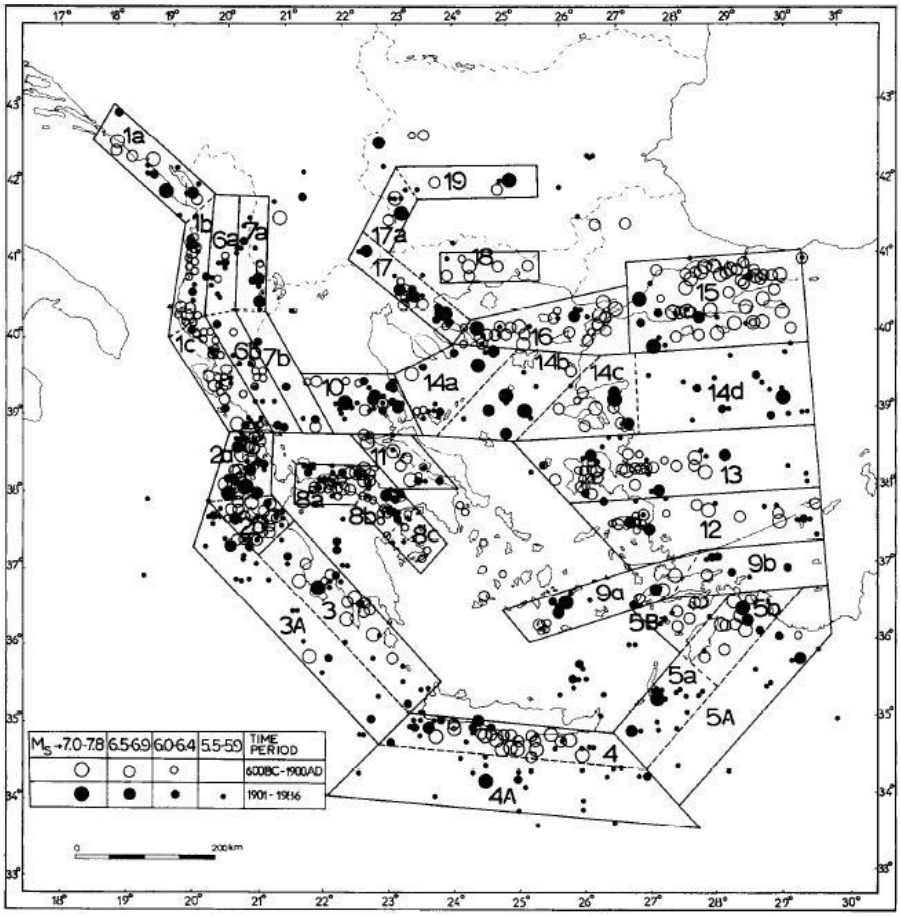

Figure 3. 3 The seismic zones (1, 2,..., 19) and seismic sources (1a, 2b,..., 19) of shallow Earthquake in Greece and the surrounding area (adapted from Papazachos 1990)

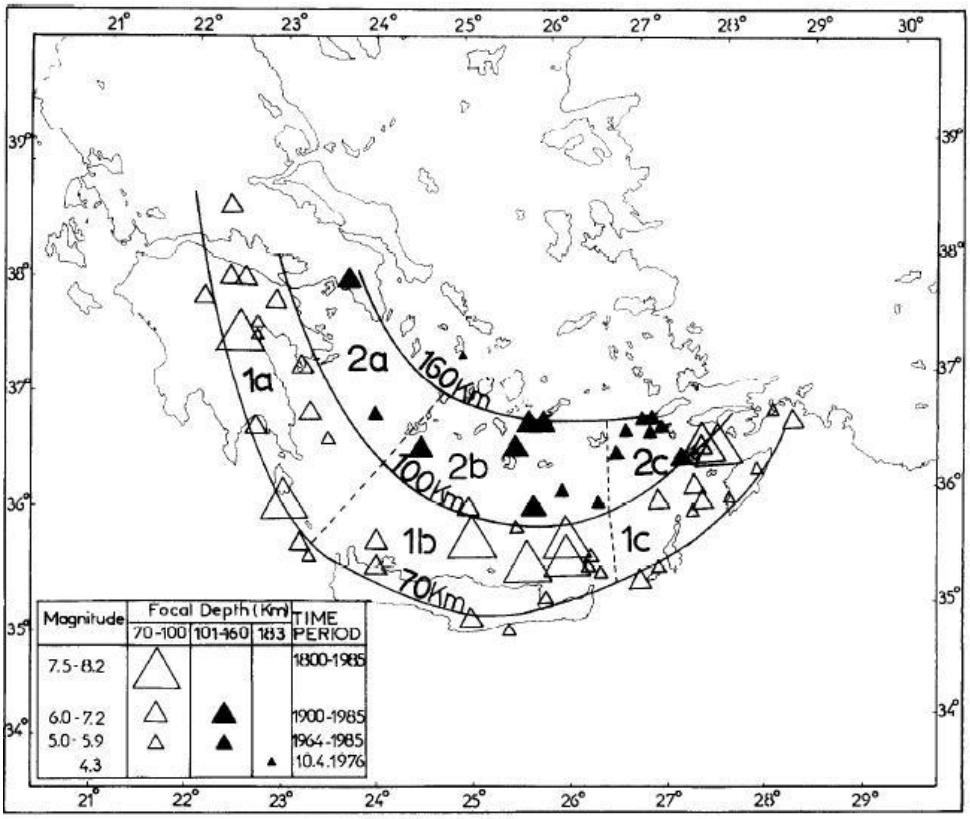

Figure 3. 4 The two seismic zones (1 and 2) and the six seismic sources (la,..., 2c) of intermediate depth Earthquake in Greece (adapted from Papazachos 1990)

The accurate definition of seismic zones or seismogenic areas is important in seismic hazard estimation, which otherwise may cause biased results (Papazachos 1990). Recent studies on seismicity and active tectonics in the Aegean region give new information which is also useful for reliable subdivision of Greece in seismogenic zones (Papaioannou and Papazachos, 2000).

Papaioannou and Papazachos (1997, 2000) divided Greece in 67 seismogenic sources of shallow shocks and 7 seismogenic sources of intermediate depth Earthquake, based on new seismological data and moreover on geological, geomorphological and other information. The quantitative seismicity, in terms of the mean return period T_m in the seismogenic sources of shallow events (Figure 3.5) and the same parameter for the 7 seismogenic sources of intermediate depth Earthquake (Figure 3.6), was then estimated by them.

Figure 3. 5 Quantitative expression of Greek seismicity in terms of mean return period, T_m (in years), in the 67 seismogenic sources of shallow seismicity (adapted from Papazachos and Papaioannou, 1997). Based on the mean return period of events with magnitude M=6.3 (the most probable maximum annual magnitude) the whole area divided in four zones

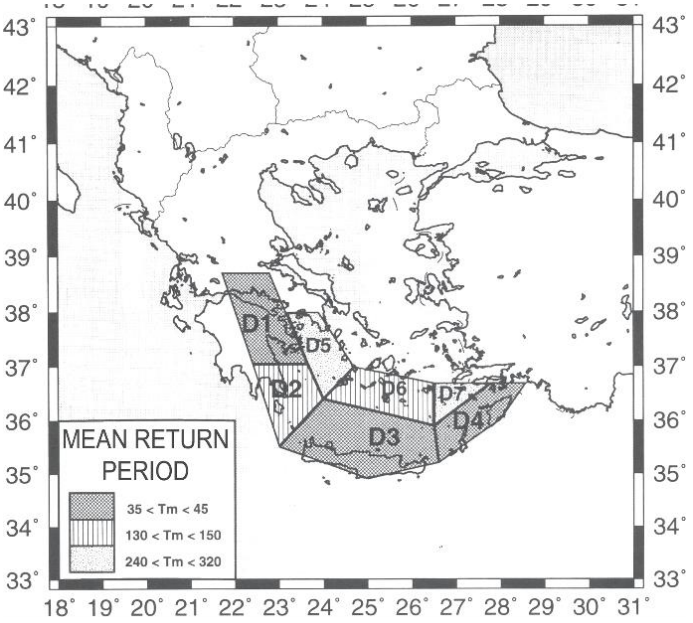

Figure 3. 6 Quantitative expression of Greece seismicity in terms of mean return period, T_m (in years), in the 7 seismogenic sources of intermediate depth seismicity (adapted from Papazachos and Papaioannou, 1997). Based on the mean return period of events with magnitude M=7.0 (most frequently occurring in the Benioff zone of Greece) the whole area divided in three zones

3.2 Recent seismic history and status of operational Earthquake forecasting in Greece

Studying historical seismicity is important for a reliable seismic risk assessment since it offers evidence for long-term Earthquake activity (Papadopulos et al., 2002). In the last six decades, the most lethal Earthquake occurred on the 12 August 1953 (M_S=7.2) in the Ionian Sea and on 7 September 1999 (M_w=5.9) in the capital city of Athens, which killed 476 and 143 people, respectively (Papazachos and Papazachou (1997). Greece is the country of highest seismicity in Europe (Bath, 1983), this is why, its Earthquake has been extensively studied. In Figure (3.7) presented the Earthquake epicenters in Greece during the twentieth century.

Regarding the operational Earthquake forecasting in Greece, as reported in International Commission on Earthquake Forecasting for Civil Protection (ICEF) (2011) by G. Papadopoulos, the anti-seismic policy in Greece is coordinated by the Earthquake Planning and Protection Organization (EPPO), which is a public authority operating under the supervision of the Ministry of Infrastructure, Transportation, and Networks (ITN). EPPO is also responsible for the evaluation of Earthquake forecasting and prediction procedures. However, the immediate response to strong and damaging Earthquake, such as rescue operations, housing, humanitarian and financial support, is coordinated by the General Secretary for Civil Protection (GSCP), and supervised by the Ministry for Citizen's Protection. The national telemetric seismograph system is monitored round-the-clock by the Institute of Geodynamics, National Observatory of Athens (NOAGI) and the collaborating Greek higher education institutes, which is a public research center under the supervision of the General Secretary for Research and Technology of the Ministry of Education and Lifelong Learning (NOAGI, 2014). The Greek Universities contribute to the seismic monitoring by transmitting to NOAGI or exchanging data from their own seismic network in real-time. NOAGI has the statutory responsibility for providing Earthquake information to civil protection agencies and the public. As soon as the source parameters of an $M \geq 4$ Earthquake are determined, the event is publicly announced, and the information is transmitted in parallel to EPPO and GSCP. Earthquake of $M<4$ are not routinely announced unless they cause social concern in local communities.

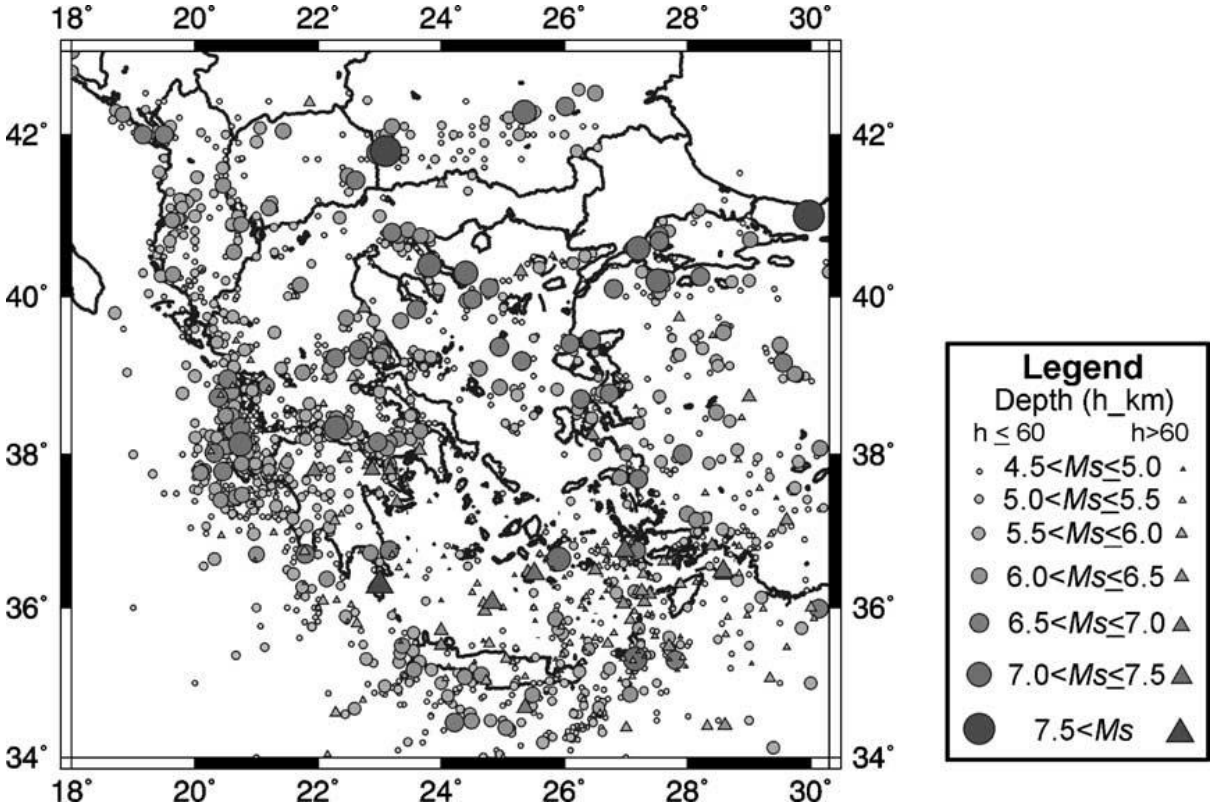

Figure 3. 7 Earthquake epicenters in Greece during the twentieth century (all focal depths) (adapted from Burton et al., 2004)

In this study, in order to find the relation between TIR anomalies and Earthquake occurrence have been considered all seismic events of M≥4, which were taken from NOA catalog for Greece as well as, all Earthquake occurred in the neighboring areas (i.e. 1º×1º) from USGS catalog since 5 April 2004 up to 31 January 2014 (Figure 3.8).

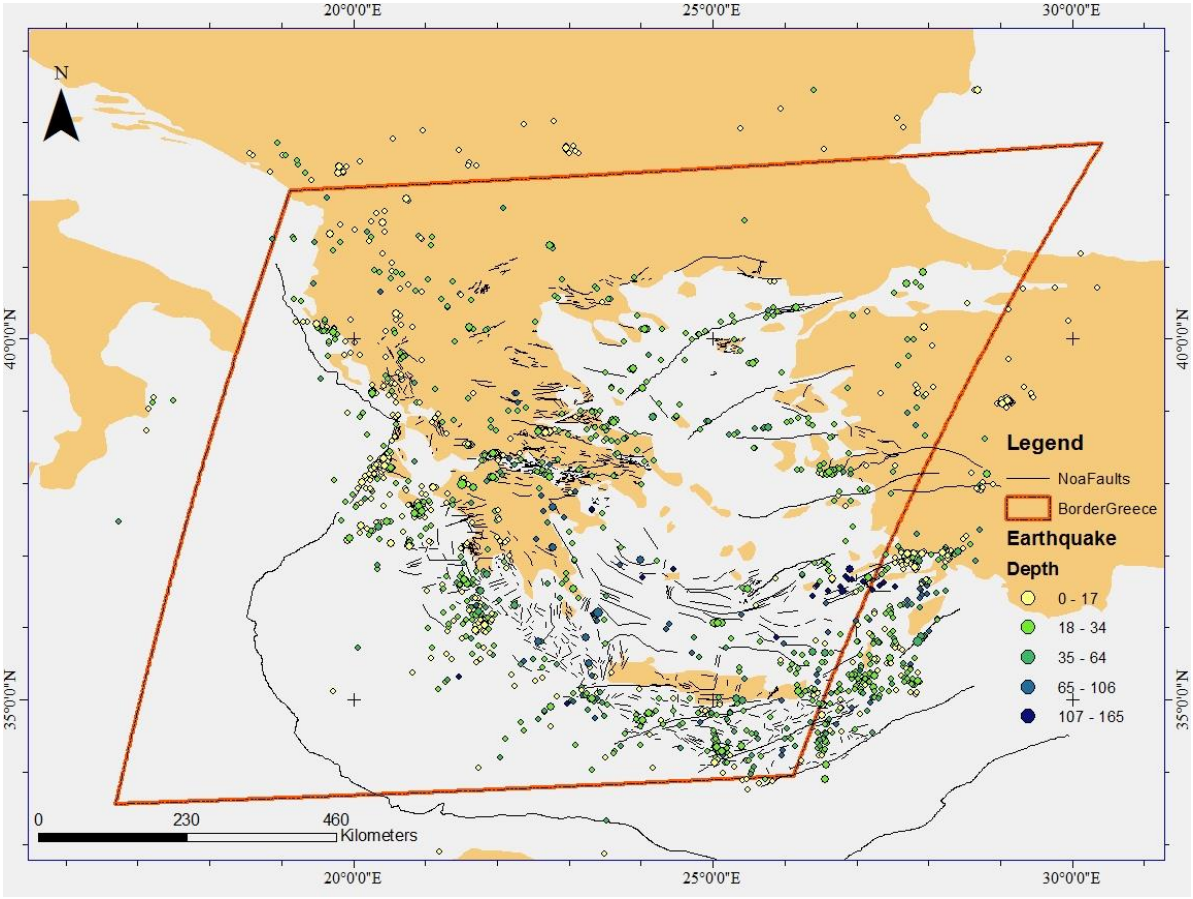

Figure 3. 8 Earthquake (about 1530 events) that occurred from5 April 2004 up to 31 January 2014. The color represents the depth while the radius of the circle represents the magnitude (M≥4), black lines represent the faults and the red rectangle the area under search

3.3 Implementation of RST for studying recent seismicity of Greece

As above mentioned in this thesis the RST approach has been implemented on SEVIRI data to investigate the possible relations among recent seismic events of Greece and abnormal space-time fluctuations of Earth's emitted radiation. After a brief introduction about MSG-SEVIRI mission, all the steps which have been followed in order to find possible relations between TIR anomaly observations and Earthquake activity will be described.

3.3.1 SEVIRI features and Pre-processing phases

MSG is the new generation of geostationary, meteorological satellites developed by the European Space Agency (ESA) in close cooperation with the European Organization for the Exploitation of

Meteorological Satellites (EUMETSAT). The MSG satellites carry a pair of instruments, the Spinning Enhanced Visible and Infrared Imager (SEVIRI), which observes the Earth in 12 spectral channels and the Geostationary Earth Radiation Budget (GERB) instrument, a visible-infrared radiometer for Earth radiation budget studies. Currently, Meteosat-10 (launched from the Guiana Space Centre in Kourou in 2012) is the operational geostationary satellite, positioned at 0 degrees and providing full disc imagery (Figure 3.9) every 15 minutes.

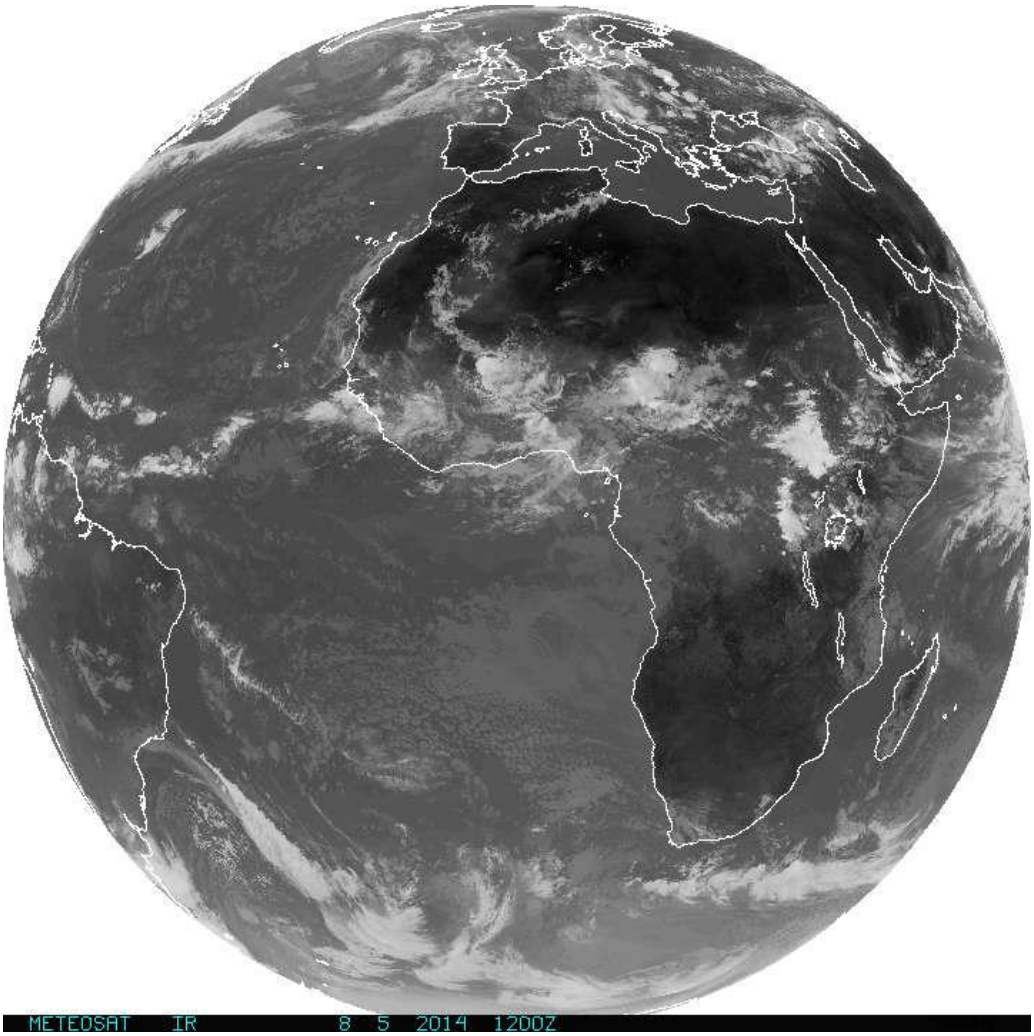

Figure 3. 9 Example of thermal infrared Meteosat 10 full disk image

Besides Meteosat 10, there are other 3 Meteosat satellites currently operational (Table 3.1), each with its specific task.

Table 3. 1 Meteosat Satellites

Current Meteosat Satellites			
Satellite	**Lifetime**	**Position**	**Services**
Meteosat-10 (MSG)	05/07/2012 – Nominal fuel lifetime is until 2022	0°/36,000 km	0º SEVIRI Image Data. Real-time Imagery
Meteosat-9 (MSG)	22/12/2005 – Fuel lifetime is expected to be extended until 2021	9.5° E/36,000 km	Rapid Scan Service from 9 April 2013. Real-time Imagery
Meteosat-8 (MSG)	28/08/2002 – Fuel lifetime is expected to be extended until 2019	3.5° E/36,000 km	Backup service for 0°, plus RSS from 9 April 2013
Meteosat-7 (MFG)	02/09/1997 (IODC since 01/11/2006) – 2016	57° E/36,000 km	Indian Ocean Coverage. Real-time Imagery

The scanning of the Earth disk is obtained by using the satellite spin (100 rpm +/-1%) in the East-West direction and by stepping a flat scan mirror in the South-North direction after each East-West line, to set up the instrument for acquiring the scan of image data. One complete revolution of the satellite lasts 0.6 seconds of which only about 30 milliseconds are available over the Earth disk to acquire one scan. After the 30ms spent imaging the Earth, the remaining 570 ms are used mainly for scan mirror stepping, data transmission and deep space data acquisition for Direct Current Removal. SEVIRI sensor consists of a scan mirror, a three-mirror telescope, and a set of filters and lenses that illuminate a series of infrared and visible light detectors (Figure 3.10).

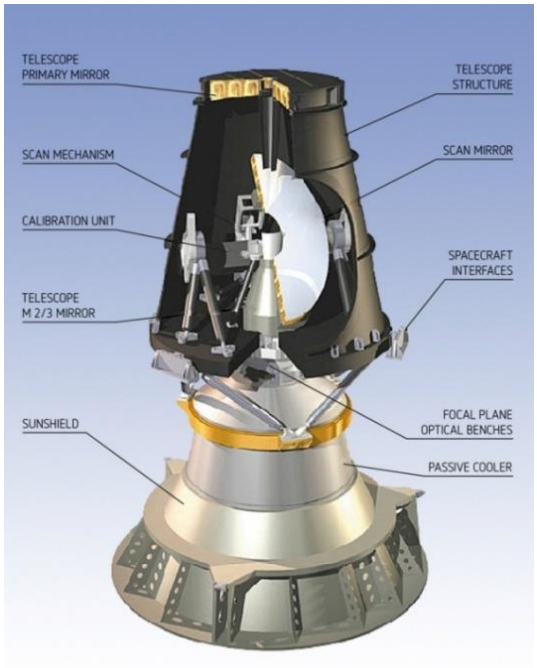

Figure 3. 10 The SEVIRI Instrument main unit (MSG)

SEVIRI with its 12 different spectral channels has unique capabilities in cloud imaging and tracking, fog detection, measurement of the Earth surface and cloud top temperatures, tracking ozone patterns, as well as many other improved performances. In the following the description of the 12 imaging channels is provided:

- Two visible channels VIS 0.6 and VIS 0.8 to provide cloud and land surface imagery during daytime. These bands help in the discrimination of vegetated surfaces from clouds at different periods of the year and in the determination of the vegetation index and aerosol loads.
- The NIR1.6 channel is used to discriminate clouds from snow and water clouds from ice clouds. In combination with the 2 visible channels, it improves the observation of aerosol, soil moisture and vegetation index.
- The HRV Channel is implemented in support of the now-casting.
- IR6.2 and IR7.3 channels are used to determine the water vapour distribution in two distinct layers of the atmosphere. They are also used in combination with the long wave IR window channels for temperature determination of thin clouds and wind determination in cloud free areas.
- The four channels IR3.8, IR8.7, IR10.8 and IR12.0 provide continuous cloud observation along with a temperature estimate of clouds, land and sea surfaces. IR3.8 is especially used at night to detect fog and very low clouds (it is less useful during daytime as the sun illumination is not negligible at this wavelength).
- Channels IR9.7 and IR13.4 are used to meet the Air Mass Analysis mission and improve the Basic Multi-Spectral Imaging, Cloud Motion Vectors and Surface Parameter Performances.
- Channel IR 9.7 belongs as well to the ozone absorption band and is used for the monitoring of the upper atmosphere, mainly tropopause features and stratospheric winds. It may also monitor the total ozone content.
- IR13.4 lies in the CO_2 absorption band and is intended to being used for cirrus discrimination, cloud top pressure evaluation, a cloud track and wind height assignment.

Raw data (Level 1.0 data) coming from the SEVIRI instrument are processed by EUMETSAT's ground segment, that corrects in real-time each received Level 1.0 image for all radiometric and geometric effects and geo-locates it using a standardized projection. So, the Level 1.5 data are derived. Nominally the full Earth disk is covered for all image channels except HRV. For HRV only half Earth coverage in E-W is provided. For all channels except HRV, the nominal Level 1.5 image

size is 3712 lines by 3712 columns (N-S by E-W), the sampling distance defined to be exactly 3 km by 3 km at the sub-satellite point. For the HRV channel, the image size is 11136 lines by 5568 columns (N-S by E-W) with a sampling distance defined to be exactly 1 km by 1 km at the sub-satellite point. The Level 1.5 pixels are the results of the re-sampling of Level 1.0 image data being acquired by several detectors (3 for all channels, except HRV where 9 detectors are used) and their binary representation is 10-bit.

The other instrument onboard of MSG satellites, GERB, makes accurate measurements of the short and long wave components of the radiation budget at the top of the atmosphere. GERB provides valuable data on reflected solar radiation and thermal radiation emitted by the Earth and atmosphere.

Level 1.5 data are finally redistributed to direct broadcast stations. In this thesis data acquired by the EUMETCast station installed at University of Basilicata (LADSAT Laboratory) have been used. Such a station is able every 15 minutes to acquire data in real-time and then to decrypt, decompress and finally transform in raw (in terms of digital counts) images, which are stored in archives (one for each of the twelve SEVIRI channels: Figure 3.11). For this study, in order to identify thermal anomalies, the TIR images acquired by SEVIRI sensor in the IR10.8 channel (spectral bandwidth 9.80-11.80 μm) have been considered.

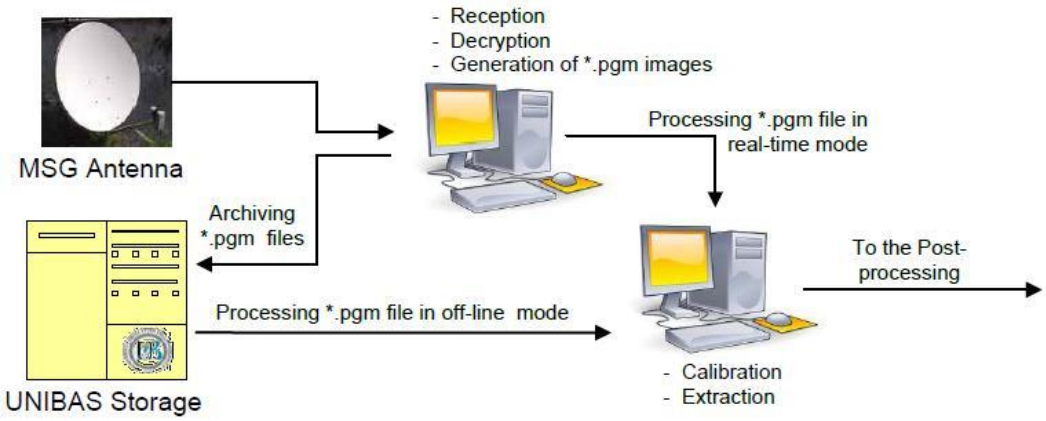

Figure 3. 11 The acquiring/pre-processing system of the LADSAT (University of Basilicata) Laboratory

The pre-processing of Level 1.5 data consists of two main phases:

Calibration: Digital counts of raw images are converted in physical quantities (e.g., spectral radiance, brightness temperature, spectral reflectance, etc.). In order to produce TIR anomaly maps, MSG-SEVIRI channel IR10.8 data are calibrated into brightness temperature (T_{TIR}). Level 1.5 data are representing in a fixed radiometric scale. This scale is provided through two linear scaling

parameters (slope and offset)[8]. The relation between the binary pixel value (the pixel count) and the physical radiance units (expressed in $mWm^{-2}sr^{-1}(cm^{-1})^{-1}$) is defined the relation:

Radiance = Cal_Offset + (Cal_Slope × Pixel Count) (Equation 3.14)

Instead, the relation between effective radiance and equivalent brightness temperature in units Kelvin is defined by the relation:

$$T_b = \frac{C_2 v_c}{\alpha \log\left[C_1 v_c^3 / \bar{R} + 1\right]} - \frac{\beta}{\alpha} \quad \text{(Equation 3.15)}$$

With $C_1=2hc^2$ and $C_2=hc/k$ radiation constants, where c, h, and k are the speed of light, Planck, and Boltzmann constant respectively. The regression coefficients ν_c, α and β are found from a non-linear regression of the pre-calculated lookup table for the different SEVIRI channels (Eumetsat, 2012).

Extraction: a spatial subset of the original full disk (Area of Interest, AOI) of MSG-SEVIRI images, which represent the whole hemisphere centered over Greenwich meridian, is obtained. Accordingly with Tramutoli, (1998), the size, shape, orientation and spatial arrangement of the selected AOI matrixes represent the common spatial support, where the reference fields will be calculated.
For this study, from the full disk image of MSG-SEVIRI (3712 columns × 3712 lines) have been extracted a matrix of (251 columns × 215 lines) which includes the portion of Greece (the area within the red box in Figure 3.12).

3.3.2 Creation of the historical data-sets

The first fundamental step at the basis of RST implementation is the generation of the historical (at least five years) data-set of homogenous (same platform, year, month, etc.) satellite data. For the specific application of this thesis, TIR images acquired at the same hour of day (e.g. midnight, in

[8] "Cal_Slope" and "Cal_Offset" normally not change. They are not related to the calibration process performed to correct the image radiometrically. The radiometric processing from Level 1.0 (raw data) to Level 1.5 is performed in four main steps: 1) Linearization: the non-linearity of the detection chains has been established on ground. This information is used to remove the effects of non-linearity from the measurement. 2) Conversion into radiances: a preliminary conversion is performed to go from counts into radiances. 3) Calibration: the calibration allows correcting the preliminary estimate of the radiance into accurate numbers. 4) Scaling: to store the radiance values in the foreseen 10-bit integer format, a linear scaling is performed using "Cal_Slope" and "Cal_Offset".

order to reduce signal variations due to daily solar cycle), in the same calendar month of the year (e.g. January 2005, January 2006, …, January 2013) to reduce the contribution of annual variability (seasonal variation of the temperature and emissivity, which mainly related to the different vegetations coverage) have been selected. To accomplish this, a User Interface, the Geohazard Observational Tool (Ghost), developed at LADSAT laboratory, was used (Figure 3.12).

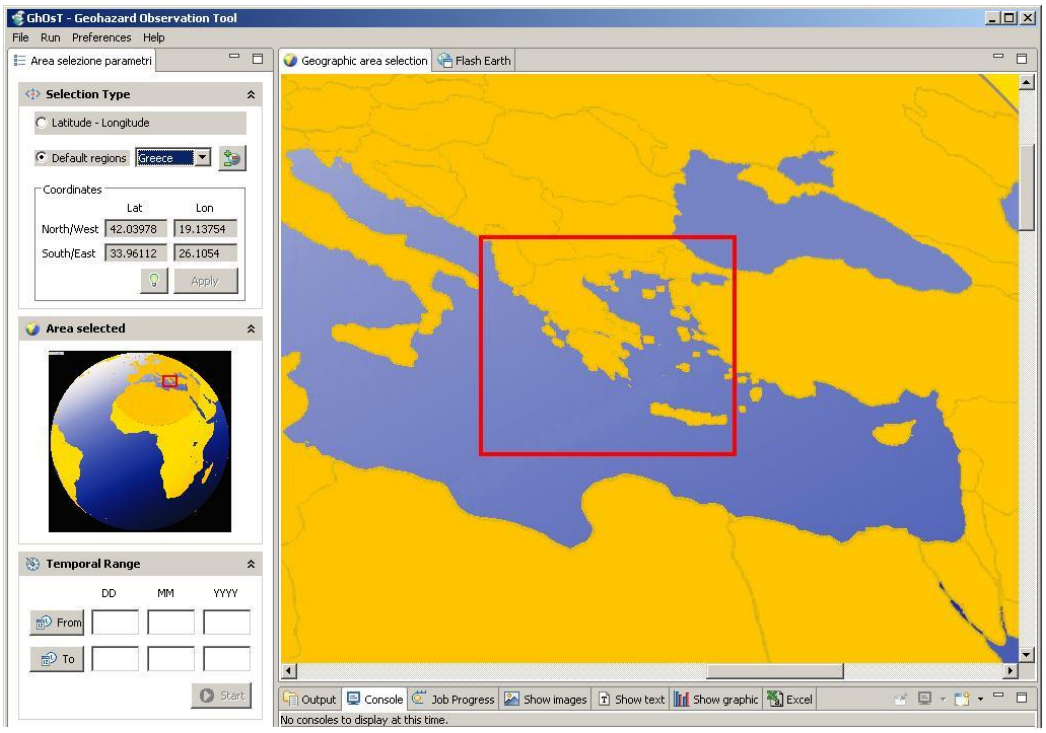

Figure 3. 12 GeoHazard Observational Tool (Ghost)

Through this software, it is possible to define: i) the spatial subset related to the portion of Greece from the full disk image, ii) the period and time of the images and iii) the channel of interest (i.e. channel IR10.8 of MSG-SEVIRI). The data-set used for this study is all TIR images (3151) of UNIBAS archive collected in the first SEVIRI time slot (00:00÷00:15 GMT) from May 2004 to December 2013, namely ten years of data. At the end of this phase, twelve (each for each calendar months, Figure 3.13) data-sets were available.

Figure 3. 13 The homogeneous data-set built following the RST prescriptions. Light blue cells represent the available SEVIRI TIR images (acquired at midnight from May 2004 to December 2013) in LADSAT archive.

3.3.3 Identification of cloudy pixels

By exploiting the above generated satellite data-set, the reference fields were computed. The computation of reference field is made considered only the cloud-free pixels for each image,

because cloudy pixels are not transparent to the passages of the Earth's TIR emission, and not allow the transmission of the radiation toward the satellite sensor. In this study, cloudy pixels have been identified by, the One-channel Cloudy-radiance-detection Approach (OCA, Pietrapertosa et al., 2001; Cuomo et al., 2004), which considers cloudy (i.e. affected by clouds) those satellite radiances that significantly differ from those expected in clear sky conditions. In order to make faster and more reliable the cloud identification, a preliminary filter is applied to all the images, discarding in a first step all those pixels showing very low brightness temperature and probably affected by cloud. Concerning such a threshold value, a visual inspection of several images for each month, allowed identifying it. In this way, for this study, for the months from December to February has been chosen an entry threshold of 269 ºK, for the months from March to May and from September to November has been chosen a threshold of 270 ºK and for the summer months from June to August has been chosen a threshold of 275 ºK.

After that, on the homogeneous historical records selected in the previous step, a iterative 2σ-clipping[9] procedure is applied to eliminate the remaining "cold" pixels. In this way reference images ($\boldsymbol{\mu_R(r)}$ and $\boldsymbol{\sigma_R(r)}$) are then computed only on the time-series elements which have survived at the end of such a clipping procedure. Subsequently, for the image at hand, cloudy pixels are identifying using the following index:

$$\otimes(r,t') = \frac{R_{TIR}(\mathbf{r},t') - \mu_R(\mathbf{r})}{\sigma_R(\mathbf{r})} \qquad \text{(Equation 3.16)}$$

where $R_{TIR}(\mathbf{r}, t')$ is the signal measured at location $\mathbf{r}$ and time t' in TIR spectral band, $\mu_R(\mathbf{r})$ and $\sigma_R(\mathbf{r})$ are the time average and standard deviation values of $R_{TIR}(\mathbf{r}, t')$ at location $\mathbf{r}$. Pixels are declared as cloud when $\otimes_R(\mathbf{r}, t')$ index is lesser of -2.

3.3.4 Computation Differential reference fields

The Earth's thermal monitoring by TIR satellite sensors finds an intrinsic limitation when wide and persistent cloudy coverage dominate the TIR scenes. When the cloudiness is very wide and persistent the scene can be so "obscured" that it is hard to observe the space-time continuity of eventual TIR anomalies over the selected area tests. From the other side, the opacity of the clouds

[9] kσ-clipping is a quite standard statistics method which iteratively updates the population of a time-series R(t) (with mean μ_R and standard deviation σ_R) saving for further processing only those time-series elements having $|R(t)-\mu_R|<k\sigma_R$ (symmetric clipping). At each new step, new μ_R and σ_R values are computed on the time-series elements survived to the previous kσ-clipping step. The process converges when kσ-clipping produces no further elimination. In this study, an asymmetric clipping has been adopted, using the surviving condition $R(t)-\mu_R>-2\sigma_R$.

towards the TIR radiation introduces further problems in the computation of the RETIRA index. In fact, the temporal persistence of clouds over the same area determines a reduction of the population of TIR satellite records usable to build the historical reference fields, influencing in this way the multi-temporal analysis (Aliano et al., 2008; Genzano, 2014). In order to minimize the negative effects of cloudiness on the construction of the RETIRA reference fields, a selection of the TIR scenes to be used in the calculation of the reference fields has been done. The main difficulty in the selection process, and the subsequent exclusion of TIR images from the data-sets, is the choice of criteria able to remove the TIR scenes not significant, without remove a great number of TIR records from the data-set. The large number of data-set used for this study allows excluding those images affected by wide cloudy coverage without significant impact on calculation of reference field. Hence, the usable portions of TIR images have been chosen in accord to the following condition:

$$\boldsymbol{\Sigma} \text{ cloudy pixels} < 80\% \; \boldsymbol{\Sigma} \text{ total pixels}$$

AND

$$(\langle \mathbf{T(t')} \rangle) > (\langle \boldsymbol{\mu}_\mathbf{T} \rangle - 2\langle \boldsymbol{\sigma}_\mathbf{T} \rangle)$$

In this way will be removed from data-sets, those TIR images excessively covered by cloud coverage and affected by unexpected cooling effect at regional scale. These images are identified comparing the mean daily temperature ($\langle T(t') \rangle$) with the monthly mean temperature ($\langle \boldsymbol{\mu}_\mathbf{T} \rangle$). These are removed, from the computations of reference fields (Figure 3.14, 3.15), when $\langle T(t') \rangle$ is smaller than $\langle \boldsymbol{\mu}_\mathbf{T} \rangle$ with a confidence level of 2σ[10]. All the values of reference fields for each month separately for land and sea are presented in Table 3.2.

[10] The standard deviation is computed as the spatial average on the $\sigma_T(\mathbf{r})$ image in the same month of acquisition of the image at hand ($\langle \sigma_T \rangle$).

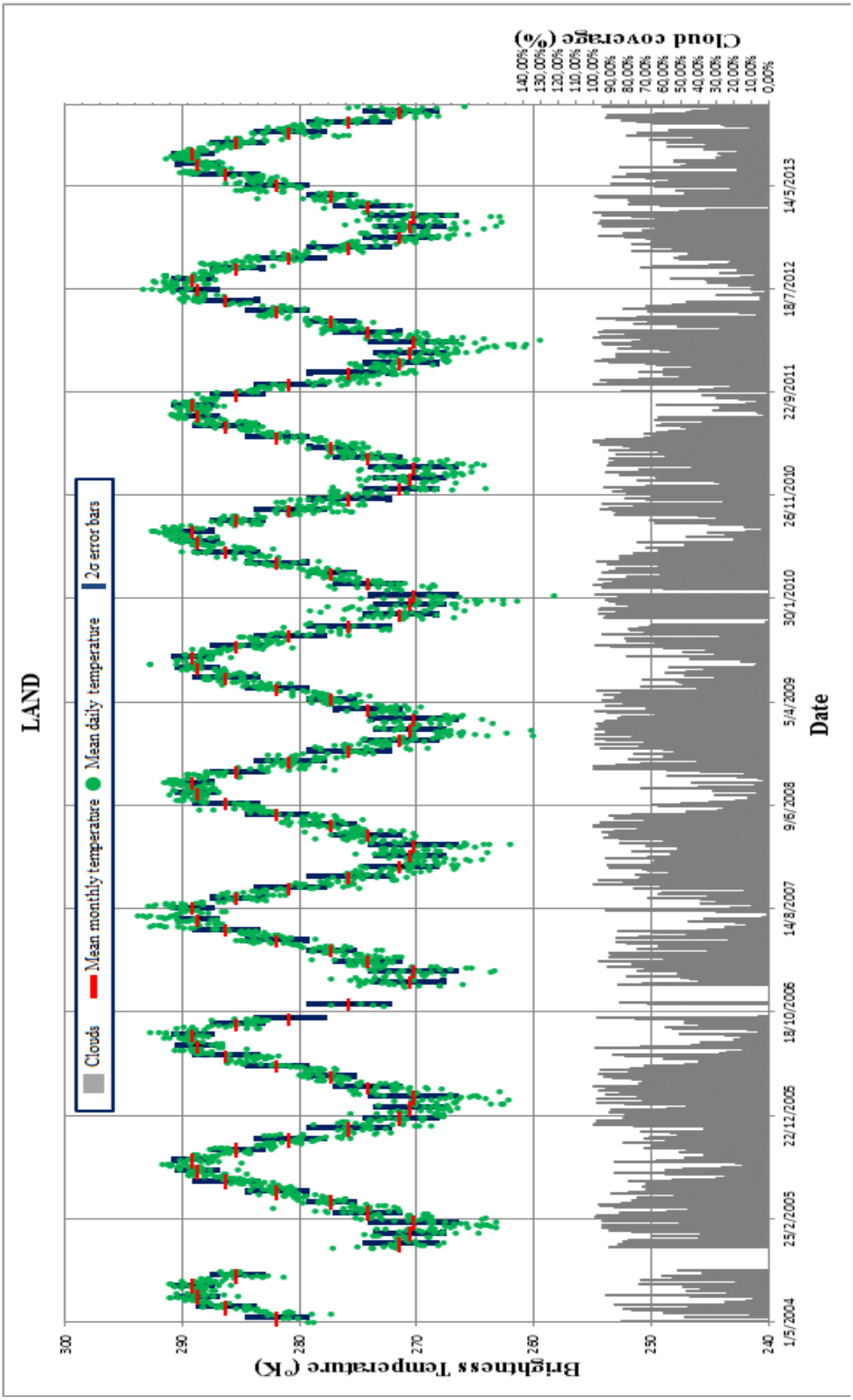

Figure 3. 14 Spatial analysis performed over land to select the TIR records influenced by meteorological effects

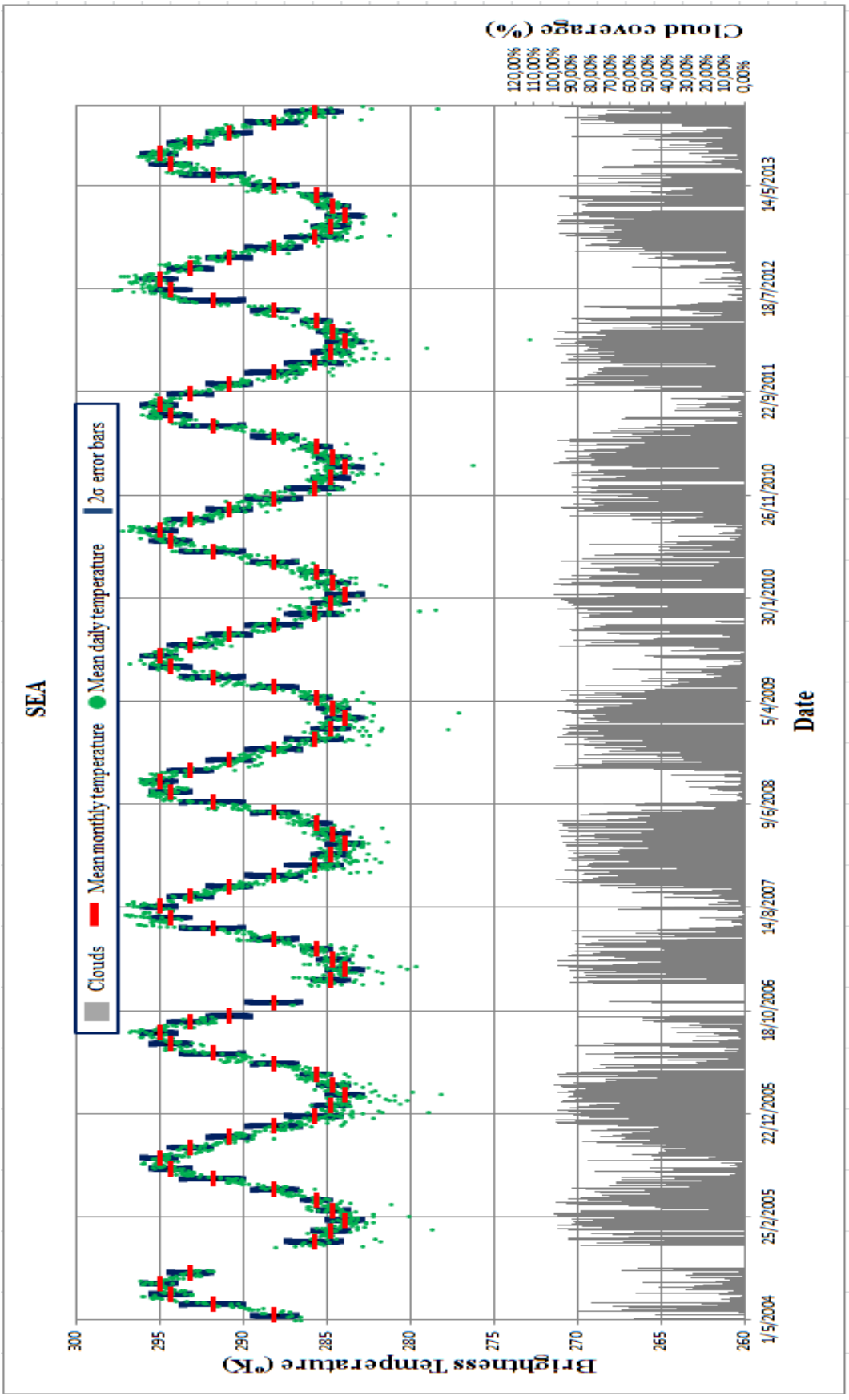

Figure 3. 15 Spatial analysis performed over sea to select the TIR records influenced by meteorological effects

Table 3. 2 Values of reference fields for each month for both class (land and sea)

MONTH	MEAN MONTHLY TEMPERATURE LAND REFERENCE FIELD (ºK)	MEAN MONTHLY TEMPERATURE SEA REFERENCE FIELD (ºK)	SIGMA LAND REFERENCE FIELD	SIGMA SEA REFERENCE FIELD
January	270,58	284,7	2,88	0,97
February	270,26	283,9	3,58	0,97
March	274,15	284,59	2,69	0,79
April	277,3	285,59	1,89	0,72
May	281,9	288,1	2,52	1,26
June	286,23	291,77	2,63	1,75
July	288,74	294,35	1,63	1,05
August	289,17	295	1,59	0,92
September	285,31	293,13	2,15	1,18
October	280,82	290,8	2,88	1,21
November	275,751	288,15	3,38	1,48
December	271,37	285,74	2,99	1,55

In order to attenuate the effects of the missed identifications of cloudy pixels, on the remaining images a spatial buffer (of 2 pixels) representative of the edge of clouds has been created and is shown in Figure 3.16.

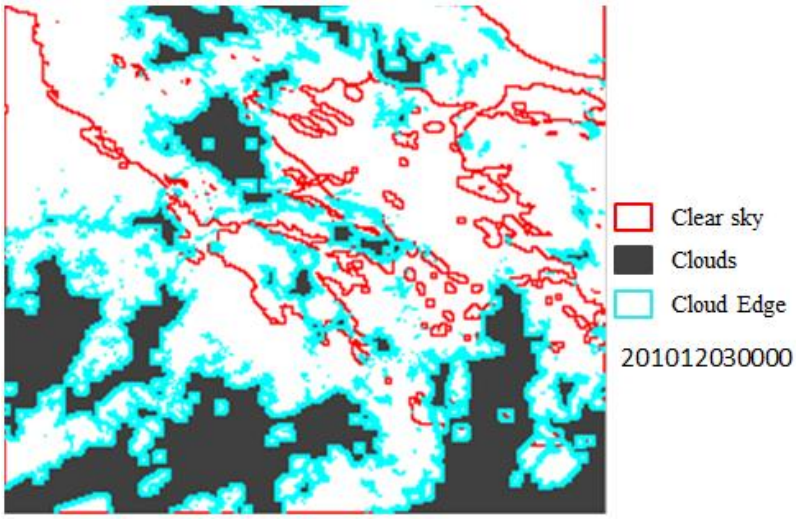

Figure 3. 16 Cloud Edge as light blue, clouds as grey and clear sky as red

So, using only the selected TIR scenes, for the pixels recognized as clear has been computed the spatial averages, considering pixels belonging to the same classes in the investigated area (land or sea) and consequently it have been computed the differential images which are calculated by the

difference between the current TIR signal value T(**r**,t') at location **r** and its spatial average <T(t')> over the image:

$$\Delta T\ (r, t') = T\ (r, t') - \langle T(t') \rangle \qquad \text{(Equation 3.17)}$$

Note again that the choice of such a differential variable $\Delta T(\mathbf{r}, t')$ instead of $T(\mathbf{r}, t')$ is expected to reduce possible contributions (e.g. occasional warming) due to day-to-day and/or year-to-year climatological changes and/or season time-drifts. Finally, for each month the reference fields (time average and standard deviation) have been computed for the difference variable $\Delta T(\mathbf{r}, t')$ so to obtain $\mu_{\Delta T}(\mathbf{r})$ and $\sigma_{\Delta T}(\mathbf{r})$.

3.3.5 Computation of RETIRA indexes

Anomalous thermal values are identified using the RETIRA index (Filizzola et al. 2004, Tramutoli et al., 2005). For each pixel (cloud-free), the brightness temperature excess is obtained comparing the current $\Delta T(\mathbf{r},t')$ signal with its historical mean value $\mu_{\Delta T}(\mathbf{r})$ and weighted by its historical variability $\sigma_{\Delta T}(\mathbf{r})$ at the considered location **r**, as follows:

$$\otimes\ (r, t') = \frac{[\Delta T(r,t') - \mu_{\Delta T}(r)]}{\sigma_{\Delta T}(r)} \qquad \text{(Equation 3.18)}$$

This change detection approach can be considered intrinsically robust as it does not require any specific assumption on data at hands. It's possible to note that, also the knowledge of the historical records of events, as well as a perfect navigation and co-location of imagery, are not really indispensable. In the first case, the lack of information on events will affect only reference fields for mean and standard deviation and its effects should be easily reduced by using an extended data set (eventually defined over a different temporal support). Uncertainties on the navigation and co-location processes will affect all reference fields with a mere effect (enhanced in presence of high signal spatial dynamics) of reduced spatial resolution (to the error maximum attributable to the used navigation-co-location procedure) of the proposed change-detection technique. In both cases and also in the worst conditions, it is expected an increasing of local standard deviation and a consequent reduction of RETIRA values (in modulus).

This could produce only a much more selective identification of over-threshold events and not, that is much more important, a generalized unreliability of change-detection step as could be revealed

by a huge number of erroneous event identifications (false alarms). The processed subset of full disk image in geostationary satellite projection needs to be geo-referenced. To this aim, the matrix with RETIRA value have been re-projected into WGS-84 geographical projection, using EUMETSAT prescriptions (Eumetsat, 1999) about geometric relationship between geographical and image coordinates.

In this way, digital products (Thermal anomaly maps) based on RETIRA index values have been developed in order to obtain similar optical of immediate interpretation (the pixels identified as anomalous have been showed with different colors in accord to the intensity of the RETIRA index value) and easily comparable with others geo-referenced information (e.g. Earthquake positions, tectonic lineaments, geological maps, etc.).

Chapter 4

Validation of RST approach over Greece

In this chapter will be presented in detail the criteria to identify significant TIR anomalies sequences and different examples will be given to better understand the total procedure. Lastly, on the base of pre-established rules, the results of the correlation analysis, which have been performed on the whole data-set of TIR observations (i.e. 10 years), among TIR sequences and Earthquake activity, will be presented.

4.1 Identification of TIR anomalies sequences

In order to discern significant TIR anomalies from outlier, all thermal anomaly maps have been analyzed following these steps:

- identification of TIR anomalies due to meteorological effects. As reported in previous work (e.g. Aliano et al. 2008; Genzano et al 2009) the presence of a wide cloudy coverage and in some cases its particular distribution on the scenes (i.e. on the warmest part of analyzed scene) may cause TIR anomalies. These are all anomalous pixels appeared in the TIR scenes affected by a wide cloudy cover (≥80% of the total pixels of the same class) or in the TIR scenes affected by an asymmetrical distributions of clouds mainly over the warmest portions of a scene (individualized by this condition $\langle T(t') \rangle \leq (\langle \mu_T \rangle - \langle \sigma_T \rangle)$). An example can be seen in the following figure;

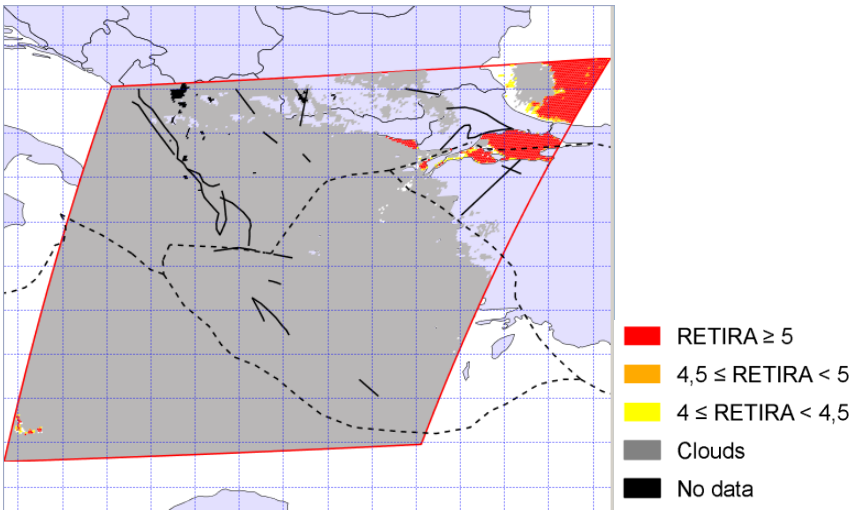

Figure 4. 1 Wide cloudy cover (≥80% of the total pixels of the same class) (200901130000 GMT)

- identification of TIR anomalies due to errors in image navigation/colocation process. In fact, a wrong navigation may cause intense TIR anomalies where sea pixels turn out to be erroneously co-located over land portions. To accomplish this, using also a binary mask representing the land-sea border, all TIR anomalies, which draw the coastline (generally for long traits) have been classified as artifacts due to wrong image navigations. An example can be seen in the following figure;

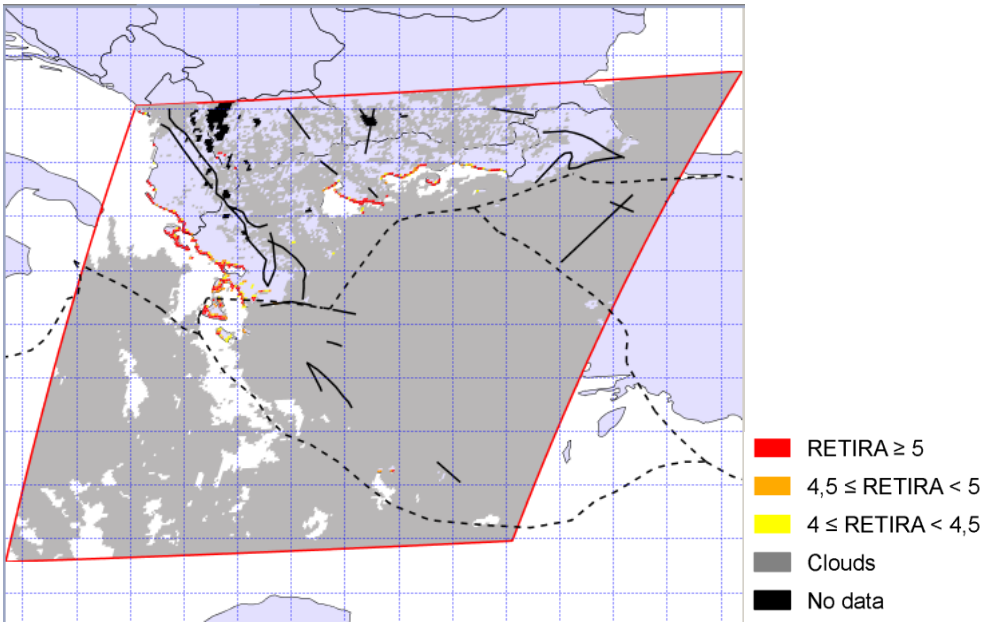

Figure 4. 2 Navigation/co-location error (TIR anomalies following the coastline) (200602080000 GMT)

- identification of short-lived TIR anomalies. These are both TIR anomalies having a limited spatial extension (i.e. less than 10 pixels) and TIR anomalies spatially extended, which have a transitory character in temporal domain, generally limited to the time duration of the connected phenomenon;
- identification of sequences of TIR anomalies persistent in space-time domain. That is anomalous pixels having a considerable spatial extension (at least more than 150 kmq[11]) restricted in the same geographical positions and persistent in a brief temporal period (lesser than 7 days).

In this way, it was possible to identify 62 TIR sequences. The following figures show an example of a TIR sequence.

[11] Considering that the size of SEVIRI pixels in the analyzed scenes is about 3.5 km of longitude and 4.5 of latitude, the minimum spatial extension required is ten SEVIRI pixels.

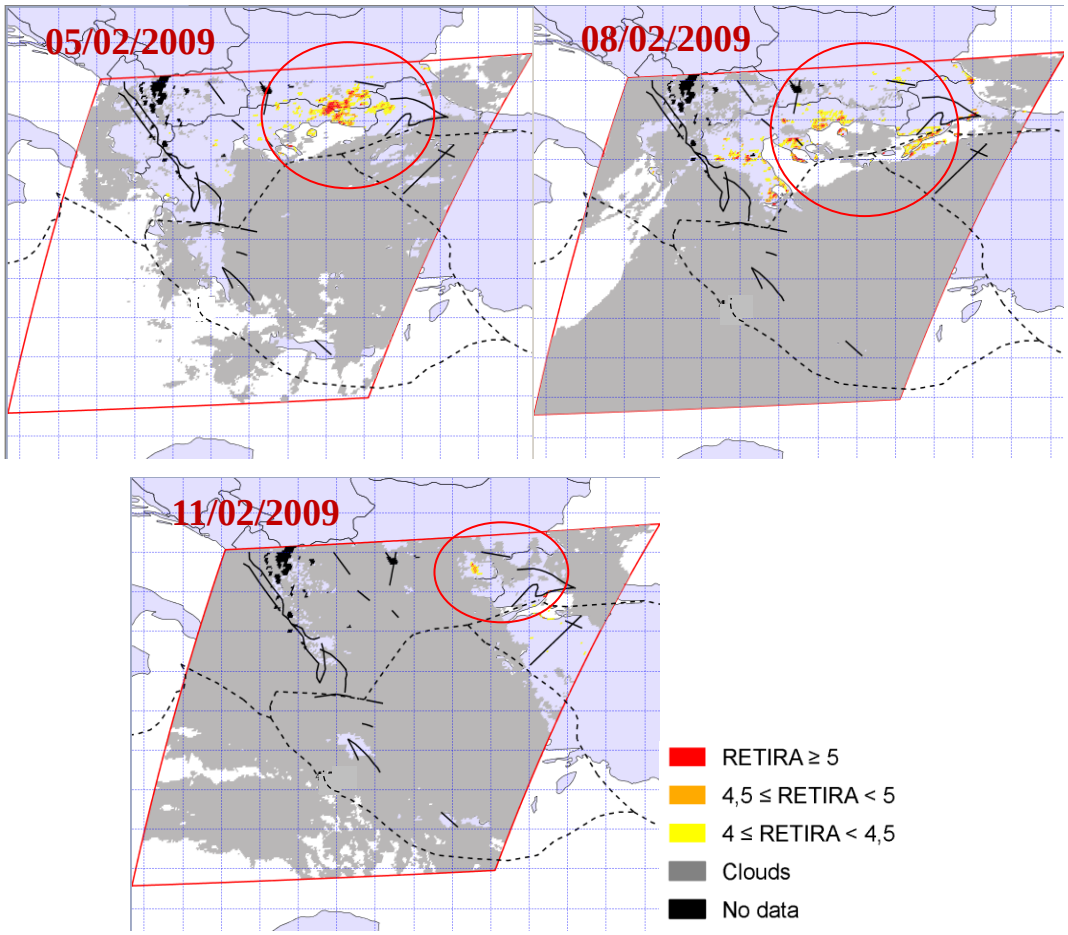

Figure 4. 3 TIR sequence (each square from the grid is 1 degree, black pixel is no data, black lines the faults, and dashed lines the boundaries. The red rectangular is the border of the image and red circle pointing on TIR anomalies)

4.2 Validation rules for the correlation between TIR sequences and Earthquake

In order to distinguish such TIR anomalies (spatially and temporally persistent) are possibly related (or not) to an impending Earthquake, a specific rules (Figure 4.4) are established, these are:

- a minimum magnitude of Earthquake considerable is 4;
- the spatial window is a variable distances (R) from observed TIR anomalies, which depend on the magnitude of expected Earthquake. Following the results obtained in previous work (e.g. Corrado et al., 2005; Genzano et al., 2007), in this work of thesis a radius of $150km \leq R \leq R_D$ has been considered (being $R_D = 10^{0.43M}$ the Dobrovolsky radius; Dobrovolsky et al., 1979);

- the temporal window considered is a time period of 30 days after (pre-seismic TIR anomalies) and 2 weeks before (post seismic TIR anomalies) the occurrence of such anomalies.

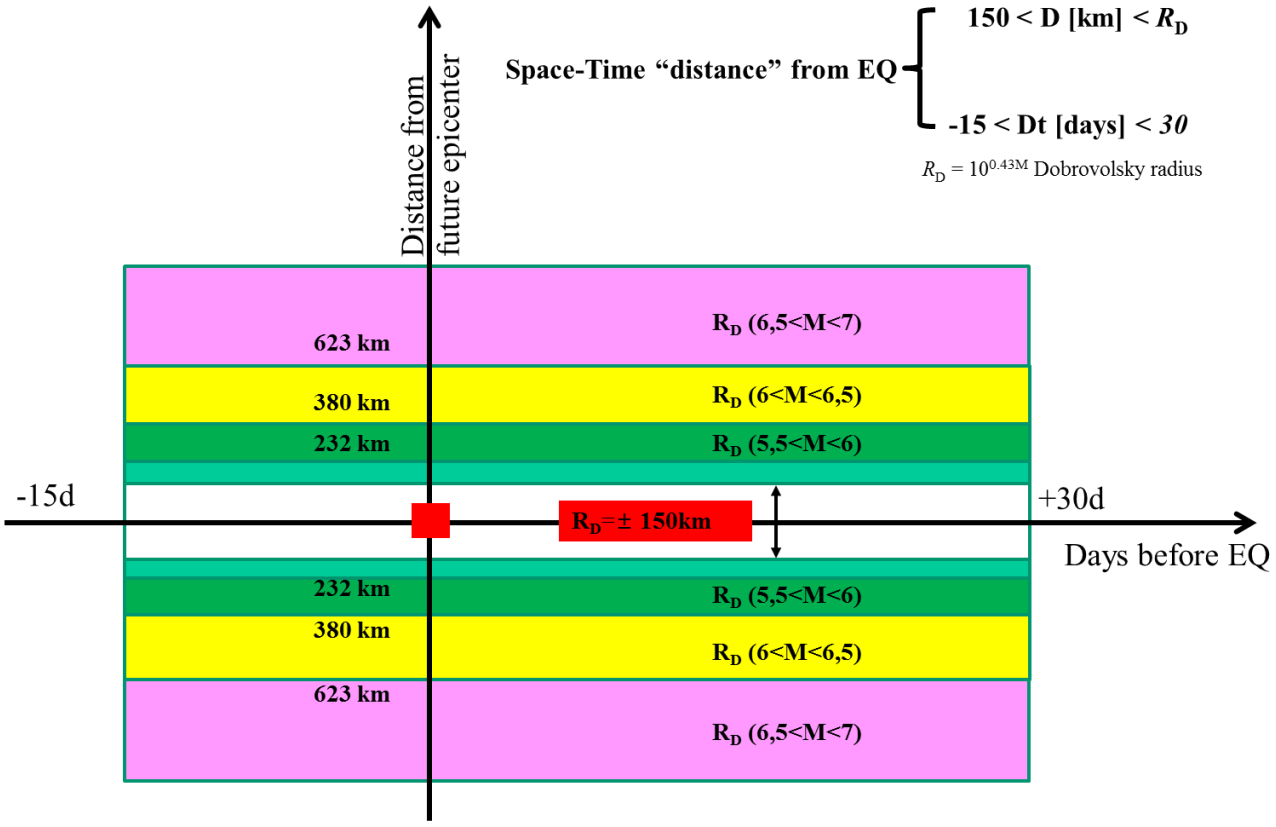

Figure 4. 4 A schematic representation of used rules. The red square in the middle represents the TIR anomaly sequence, on the x axis is represented the temporal windows, instead on the y axis the spatial windows (see text)

For each one of identified TIR sequences (i.e. 62), a dynamic spatial buffer around TIR anomalies was built in ArcGIS using the above mentioned rules. To better understand the constructions of this dynamic buffer, which represent the investigated area, the following represents how the buffer was built for one sequence. In figure (4.5) is the first day of observation of TIR anomaly that appears over Peloponnesus, near the faults. In the next figure (4.6) is the second day of observation with the buffer built for these two days and the last figure (4.7) presents the total buffer for the three days of TIR anomalies.

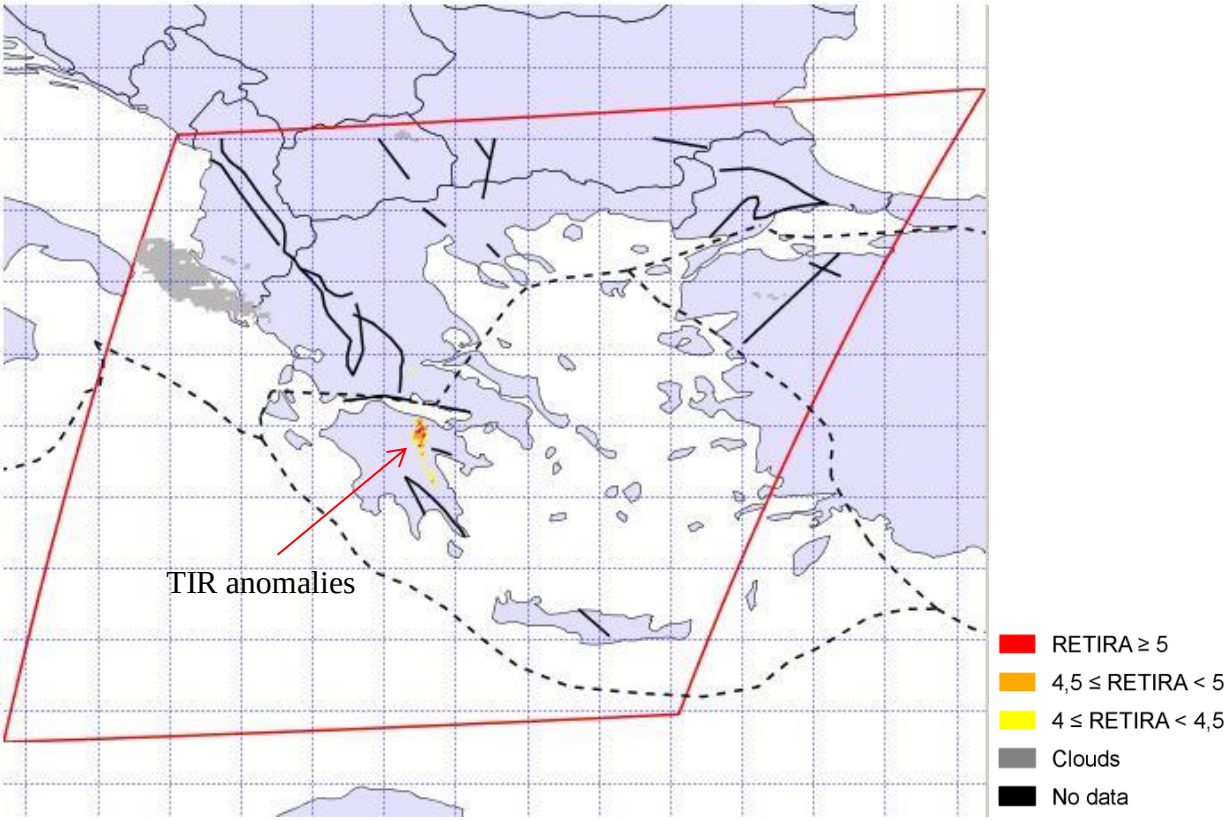

Figure 4. 5 TIR anomalies on 26/06/2007 (00:00 MGT)

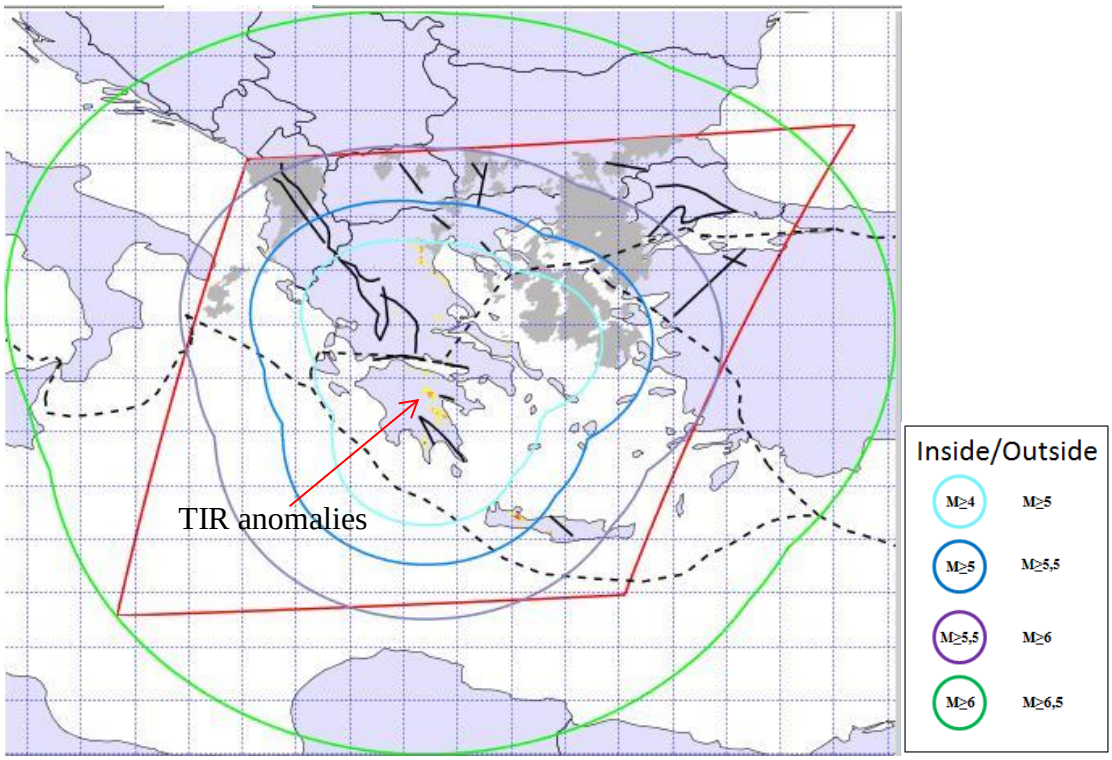

Figure 4. 6 TIR anomalies on 27/06/2007 (00:00 GMT) with buffer built around the first two days of observation

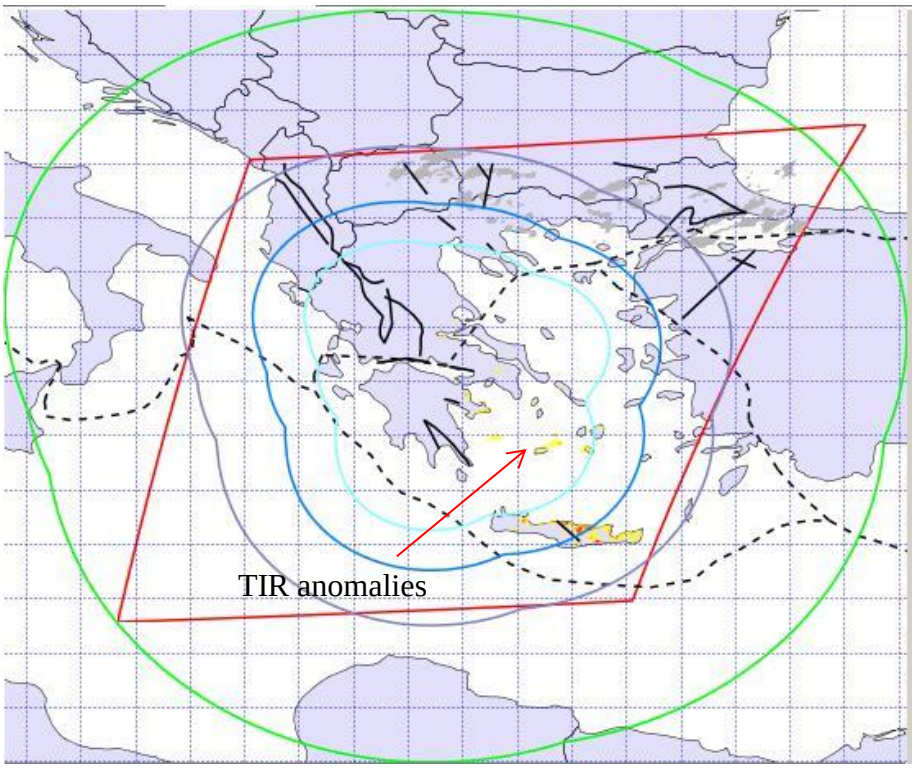

Figure 4. 7 TIR anomalies on 29/06/2007 (00:00 GMT) with total buffer

In the figures 4.6 and 4.7 is possible to see the difference among the buffer around Aegean Sea, these are due to the presence of TIR anomalies only in the third day and therefore the buffer expands in that place. This procedure has been followed for all the TIR sequences and after the creation of buffer, considering the temporal criteria proposed the presence of seismic events inside this area has been verified.

In table (4.1) are summarized the results of the analysis performed in a fixed space-time window, in yellow are reported the first TIR observation, in pink, the next day of the sequence that has a few TIR anomalies, in red, the next day of the sequence that has "normal" TIR anomalies, in grey are reported the images with high cloudy coverage, in black no data, in purple are reported images that identified as spurious effects and in green the Earthquake. The colors applied on the place of occurrence of TIR anomalies represent, with orange that no seismic event occurred before or after the TIR sequence and in blue that the TIR sequence has time persistence more than seven days. Some examples of the TIR anomalies maps will be presented in Annex 1.

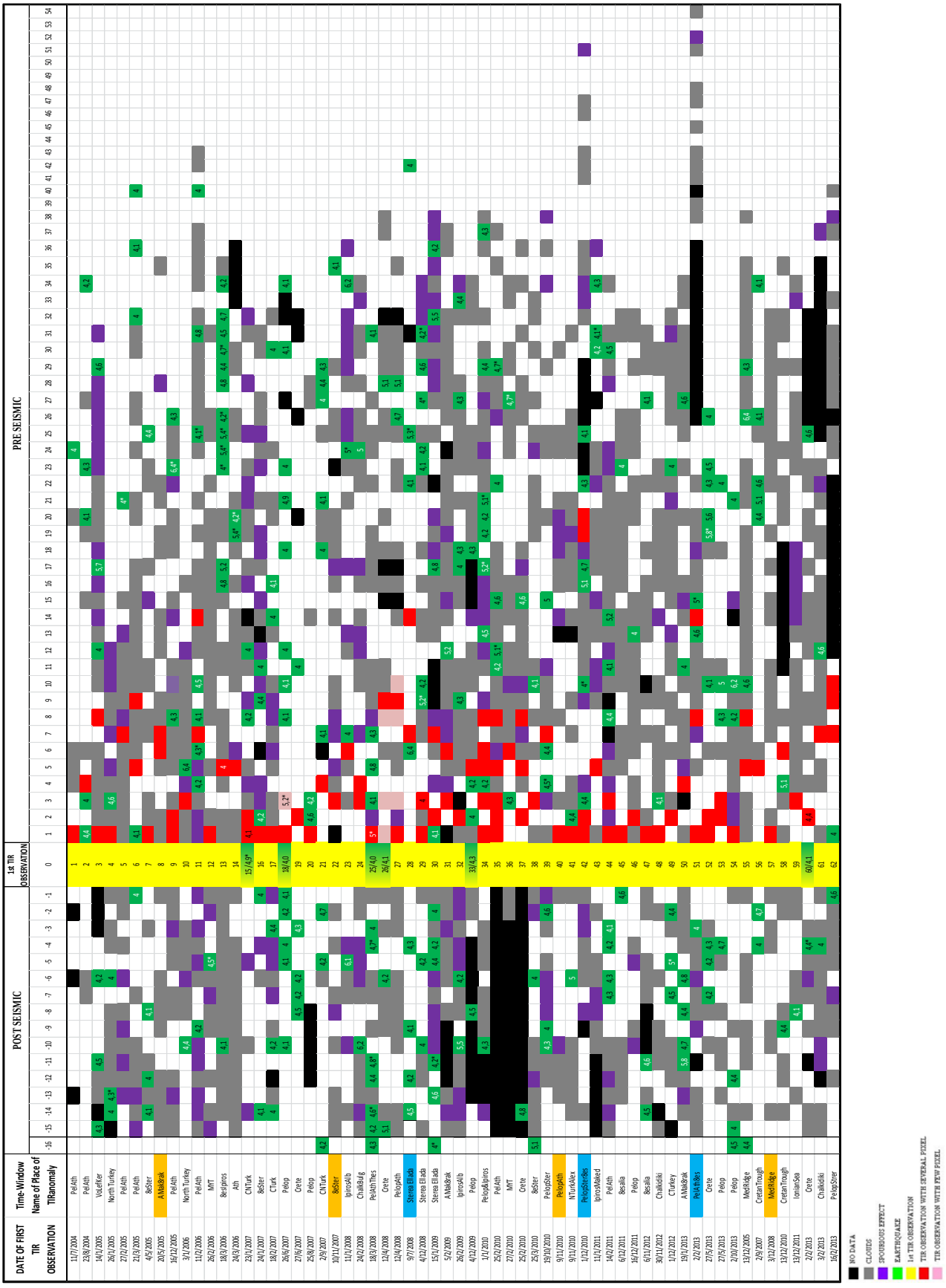

Table 4. 1 Summarized results of TIR observations and Earthquake (on the Place of occurrence, orange color represents no EQ occurrence and light blue TIR anomalies observed more than seven days)

4.3 Results

At the end of the previously described analysis, 62 TIR sequences have been identified over the ten years of TIR observations (Table 4.1), of which the 93,5% (i.e. 58 TIR sequences) are within the established rules and could be considered in a possible relation with seismic events, instead, the remaining 6,5% (i.e. 4 TIR sequences) are independent from seismicity but are caused by other phenomena, representing a false positive (figure 4.8).

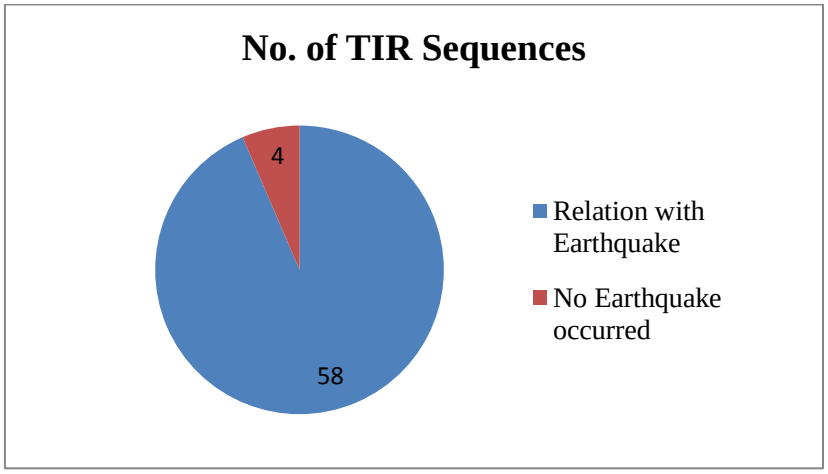

Figure 4. 8 Number of TIR sequences detected as Earthquake related or not

From the 58 identified TIR sequences, it is possible to note that (Figure 4.9):

- 40 (i.e. 69%) significant TIR anomaly sequences occurring before and after the seismic events (PRE-POST seismic TIR sequences);
- 16 (i.e. 27,5%) significant TIR anomaly sequences appearing only before the Earthquake (PRE seismic – TIR sequence);
- 2 (i.e. 3,5%) significant TIR anomaly sequences appearing only after the Earthquake (POST seismic – TIR sequences)

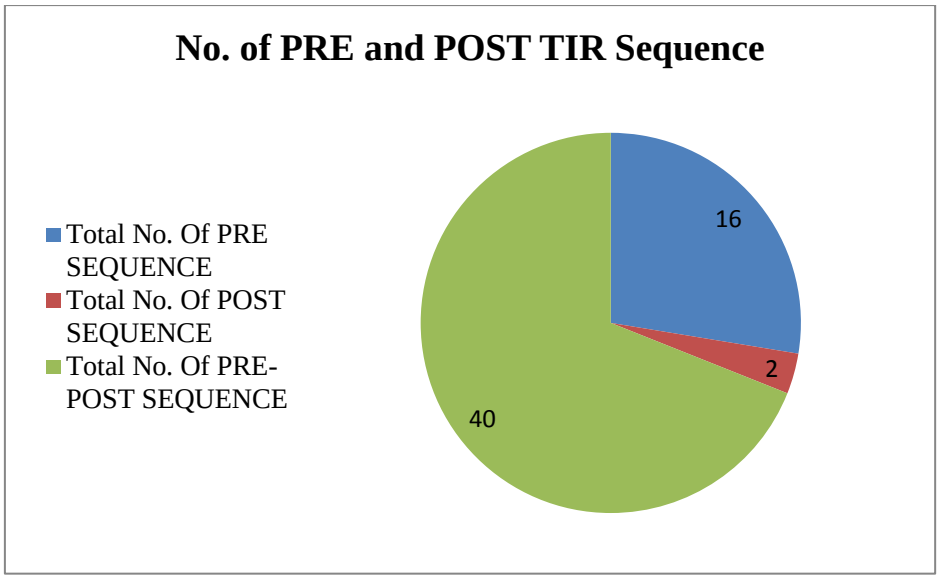

Figure 4. 9 Number of PRE and/or POST TIR sequence

In order to understand the space-time dynamic of TIR anomalies and also to obtain more indications about the genetic process of the thermal anomalies associable to seismic events, some features of the TIR anomalies and Earthquake have been analyzed. The total number of Earthquake (with magnitude greater than or equal 4) associable to the 58 TIR sequences identified is 235. There are 158 (i.e. 67%) Earthquake that occurred after the observed TIR sequences and 77 (i.e. 33%) Earthquake that occurred before the observed TIR sequences (Figure 4.10)

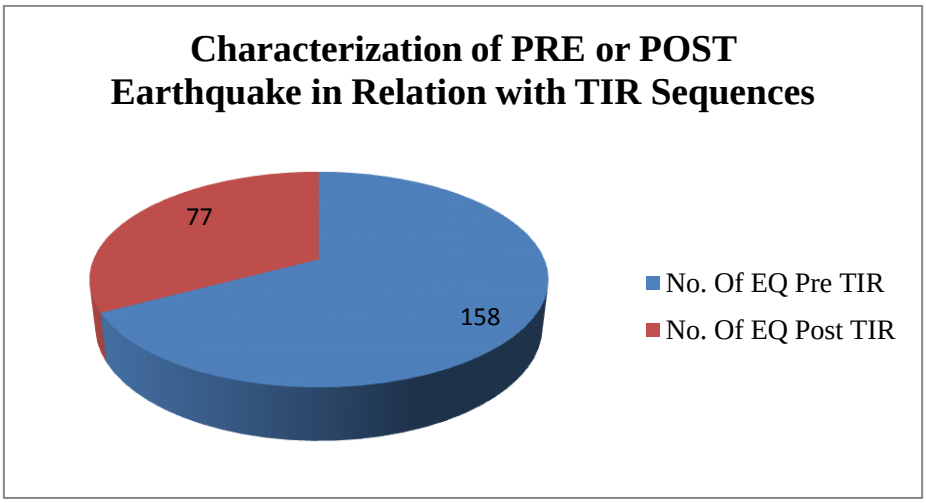

Figure 4. 10 Characterization of PRE or POST Earthquake in Relation with TIR Sequences

Considering the magnitude of these Earthquake, it is possible to note that (Figure 4.11):

- 210 seismic events have $4 \leq M \leq 5$,
- 20 seismic events have $5 < M \leq 6$;
- 5 seismic events have $M > 6$.

Instead, taking in account the depth of these Earthquake, the major part (i.e. 216) of them can be classified as shallow with $D < 60Km$, while 19 as intermediate depth events with $D \geq 60Km$ (Figure 4.12).

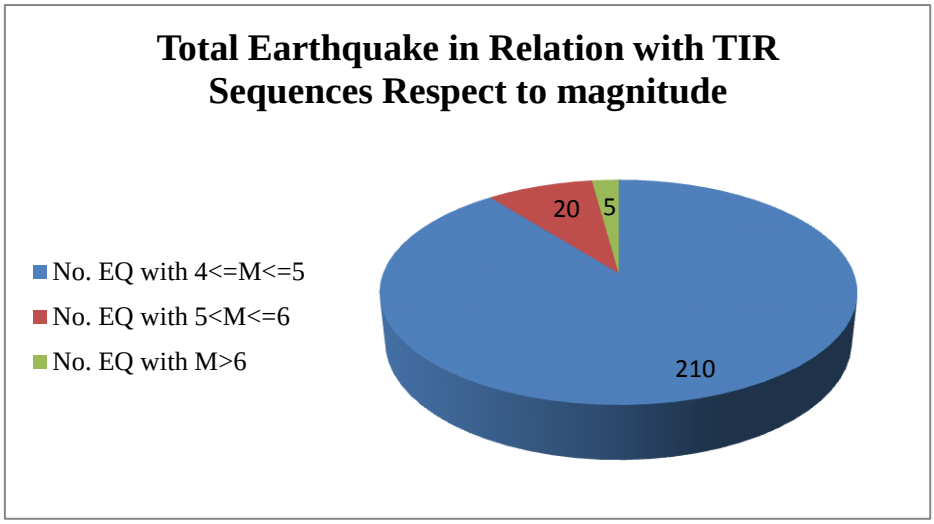

Figure 4. 11 Total Earthquake in Relation with TIR Sequences respect to magnitude

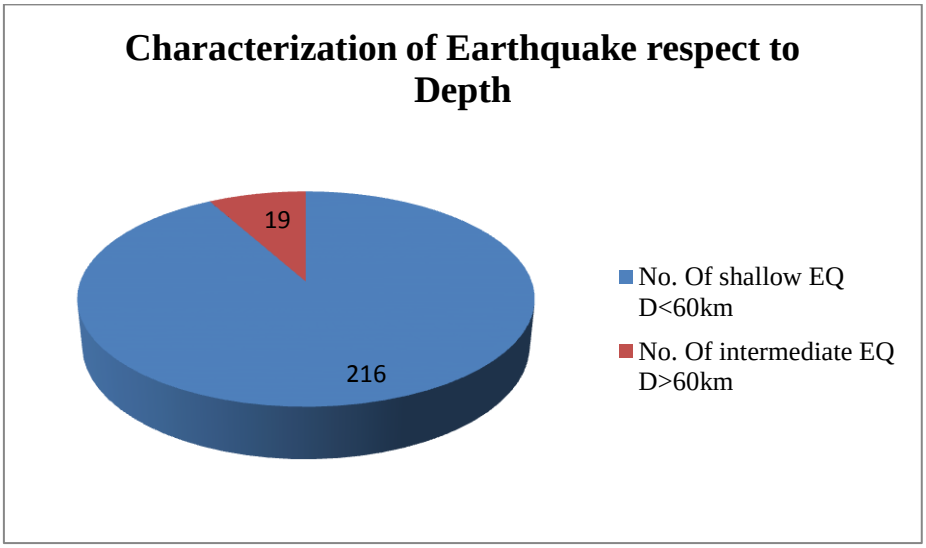

Figure 4. 12 Characterization of Earthquake respect to Depth

In the following figures (4.13 and 4.14) the relation between Earthquake features (i.e. magnitude and depth) and TIR anomalies are show. In figure 4.13, has been plotted the time lag of the Earthquake (with M≥4,5) respect to the date of first TIR observation of the significant TIR sequences. It is possible to note that:

- in the pre-seismic phase, TIR anomalies appear mainly in a temporal windows of 10-30 days before the seismic event;
- in the post-seismic phase, TIR anomalies occur few days after the Earthquake occurrence.

Moreover, it is possible to note that the seismic events with a large magnitude are closed to the day to the first appearances of TIR anomaly.

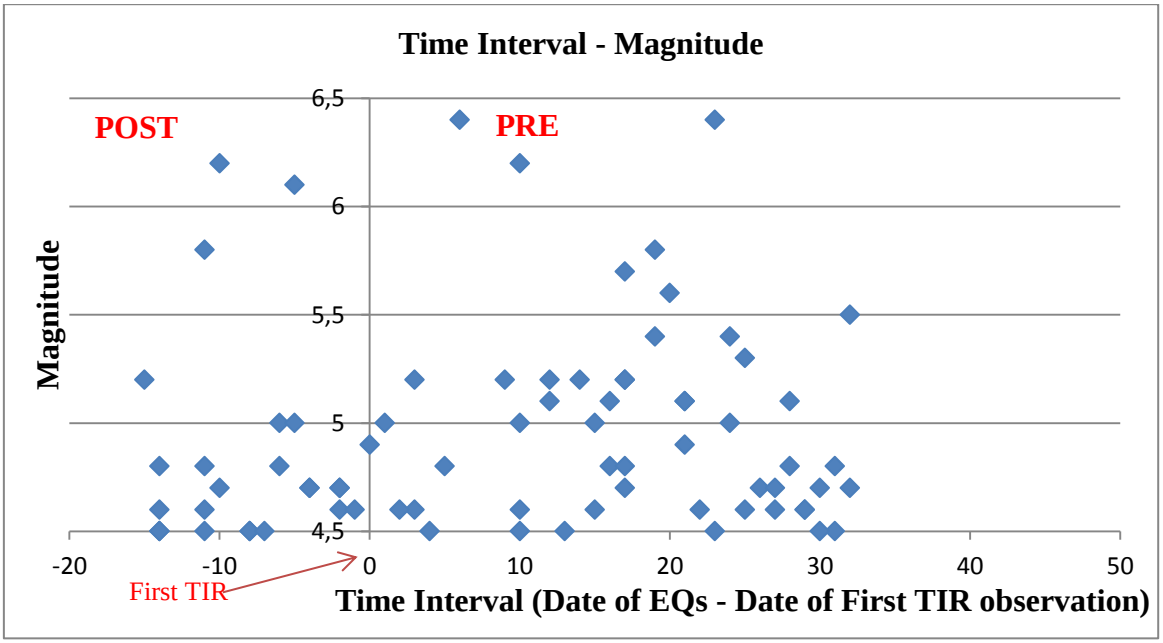

Figure 4. 13 On the left side are the Earthquake at different magnitude occurred before the first TIR observation and on the right Earthquake occurred after

A similar graph, but which take in account the depth of Earthquake rather than the magnitude is shown in figure 4.14. In this case, no particular trend is possible to observe.

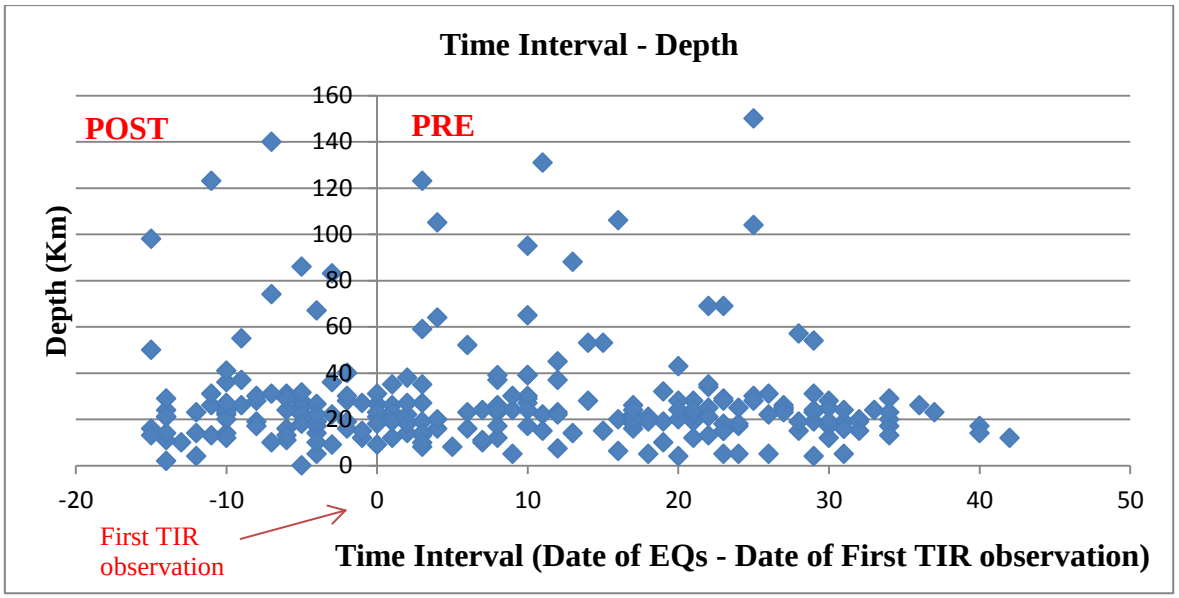

Figure 4. 14 On the left side are the Earthquake occurred before the first TIR observation and on the right Earthquake occurred after respect to Depth

CONCLUSION

In this study, the RST approach and the Robust Estimator of TIR Anomalies (RETIRA) have been used to identify possible connections between space-time fluctuations of Earth's emitted TIR radiation observed from satellite and Earthquake occurrence. The study has been implemented on ten years (May 2004 - December 2013) of MSG-SEVIRI TIR data collected over Greece, the area with the highest level of seismicity in Europe.

Differently from the standard RST approach, which usually analyzes results achieved at short temporal scale (e.g. monthly analysis), in this thesis the whole SEVIRI data-set have been investigated, highlighting the presence of 62 TIR sequences, the most of them near active faults. In order to identify possible relation among Earthquake occurrence and these TIR sequences, a pre-established space-time criteria (mainly based on magnitude of the expected Earthquake with a time window of 2 weeks before the first TIR observation and 30 days after the last TIR observation) was adopted and applied. The 93,5% (i.e. 58 significant TIR sequences) of them were found to have a relation with seismic activity and only the 6,5% (i.e. 4 TIR sequences) resulted independent from seismicity and therefore characterized as false positive.

The TIR anomalies in a such kind connection with seismic events, appear both in the pre- and in the post-seismic phases. In particular:

- 69% occur before and after the seismic events (PRE-POST seismic TIR sequences);
- 27,5% occur only before the Earthquake (PRE seismic TIR sequences);
- 3,5% occur only after the Earthquake (POST seismic TIR sequences).

In addition, in order to better understand the relations TIR anomalies-Earthquake during the different seismic phases, some features of TIR anomalies and Earthquake (e.g. magnitude) have been analysed. The results show that the seismic events with a large magnitude ($M \geq 5,5$) are closed to the day to the first appearances of TIR anomaly. However, in the pre-seismic phases significant TIR anomalies appear mainly in a temporal window of 10-30 days before the occurrence of Earthquake, instead in the post-seismic phases TIR anomalies occur few days after the happening of Earthquake.

Finally, the refined RST approach can provide significant results for the relation between Earthquake occurrences and TIR anomalies observations. In order to be more precise in some kind

of Earthquake predictions, the combined use with other parameters based on observations of different nature (i.e. seismological, geochemical, geodetic, etc.) to create an integrated system with multi-parametric analysis that could be able to provide more information about incoming Earthquake.

REFERENCES

Papazachos, B.K., Karakaisis, G.F. and Chatzidimitriou, P.M., 2005: Introduction in Seismology, ZITI Edit., Thessaloniki.

Muksin, U., Bauer, K. & Haberland, C., 2013a. Seismic Vp and Vp/Vs structure of the geothermal area around Tarutung (North Sumatra, Indonesia) derived from local Earthquake tomography, Journal of Volcanology and Geothermal Research, 260, pp. 27-42.

Lee W.H.K., 2003. Solid Earth geophysics, 547-573 (Seismology, Observational).

Kulhanek Ota, 2005: Seminar on b-value, Dept. of Geophysics, Charles University, Prague, December 10-19, 2005.

UNESCO, 1972, Report of consultative meeting of experts on the statistical study of natural hazards and their consequences, Unesco Document, SC/WS/500, pp.11

Tsuboi C., Wadati K. and Hagiwara T. (1962) Prediction of Earthquakes — Progress to Date and Plans for Further Development. Earthquake Prediction Research Group, Tokyo University, Tokyo.

Geller Robert J., Geophys. J. Int (1997) 131, 425-450, Earthquake Prediction: a critical review. Special Section – Assessment of schemes for Earthquake prediction.

Thanassoulas, C.: Short-term Earthquake Prediction, H. Dounias & Co., ISBN No:978-960-930268-5, 2007.

Weeks J., Lockner D. and Byerlee J.: Change in b-values during movement on cut surfaces in granite. Bulletin of the Seismological Society of America, Vol. 68, No. 2, pp. 333-341, April 1978.

Aggarwal Y.P., Sykes L.R, Armbruster J. and Sbar M.L (1973): Premonitory changes in seismic velocities and prediction of Earthquakes, Nature 241, 101-104.

Semenov A.N. (1969): Variations in the travel time of transverse and longitudinal waves before violent Earthquakes, Bull. Acad. Sci. USSR, Phys. Solid Earth 3, 245-248.

Whitcomb J.H., Garmany J.D., Anderson D.L. (1973): Earthquake prediction: variation of seismic velocities before the San Fernando Earthquake, Science 180, 632-635.

VanWormer J.D., Gedney L.D., Davies J.N. and Condal N.: V_P/V_S and b-values: A test of the dilatancy model for Earthquake precursors. Geophysical Research Letters, Vol. 2, No. 11, November 1975.

Allen C.R. and Helmberger D.V. (1973): Search for temporal changes in seismic velocities using large explosions in Southern California, Proc. Conf. Tectonic Problems of the San Andreas Fault System, Stanford Univ. Publications, Geological Sciences, 13, 436.

Boore D.M., Lindh A.G., McEvilly T.V. and Tolmachoff W.W. (1975): A search for travel-time changes associated with the Parkfield, California Earthquake of 1966, Bull. Seism. Soc. Am. 65, 1407-1418.

Lockner D., Lindh A. and Byerlee J. (1977): Apparent velocity anomalies and their dependence on amplitude (abstract), EOS Trans. Am. Geophys. Union 58,433.

Brace, W. F., B. W. Paulding, Jr., and C. H. Scholz, Dilatancy in the fracture of crystalline rocks, J. Geophys. Res., 71(16), 3939-3953, 1966.

Anderson L. and Whitcomb H.: The dilatancy-diffusion model of Earthquake prediction (1973). Seismological Laboratory, California Institute of Technology Pasadena, California 91109.

Moreau F., Dauteuil O.: Geodetic tools for hydrogeological surveys: 3D-displacements above a fractured aquifer from GPS time series.

Biessy G., Moreau F., Dauteuil O. and Bour O.: Surface deformation of an intraplate area from GPS time series. Journal of Geodynamics 52 (2011) 24-33.

Wang Y., Liu Y. and Su Y.: The study of Japan Earthquake Deformation based on GPS. Procedia Environmental Sciences 10 (2011) 9-13. 2011 3rd International Conference on Environmental Science and Information Application Technology (ESIAT 2011)

Varotsos P. and Alexopoulos K. (1984): Physical properties of the variations of the electric field of the Earth preceding Earthquakes. Tectonophysics, 110 (1984) 73-98.

Lazaridou-Varotsos, Mary S.: Earthquake Prediction by Seismic Electric Signals, The success of the VAN method over thirty years, 2013, XVIII, 254 p., ISBN 978-3-642-24406-3.

Singh S., Kumar A., Bajwa S.B., Mahajan S., Kumar V. and Dhar S.: Radon monitoring in soil gas and ground water for Earthquake prediction studies in North West Himalayas, India. Terr. Atmos. Ocean. Sci., Vol. 21, No. 4, 685-695, August 2010.

Ulomov V.I. and Mavashev B.Z. (1967): A precursor of strong tectonic Earthquake. Dokl. Acad. Sci. USSR, Earth Sci. Sect., 176, 9-11.

Walia V., Virk H.S. and Bajwa B.S.: Radon precursory signals for some Earthquake of magnitude > 5 occurred in N-W Himalaya: An overview. Pure and applied geophysics, 163 (2006), 711-721.

Ghosh P.C. and Bhalla N.S. (1966): A closed circuit technique for radon measurement in water and soil, with some of its applications. Proc. All Ind. Symp. on Radioactivity and Meteorology of Radionuclides, AEET, Bombay, pp. 226-239.

Leick A. 1995: GPS Satellite Surveying, J. Wiley & Sons, New York

Akhoondzadeh M. and Saradjian M.R.: TEC variations analysis concerning Haiti (January 12, 2010) and Samoa (September 29, 2009) Earthquakes. Advances in Space Research 47 (2011) 94-104.

Liu J.Y., Chen Y.I., Chuo Y.J. and Tsai H.F.: Variations of ionospheric total electron content during the Chi-Chi Earthquake. Geophysical research letters, Vol. 28, No. 7, Pages 1383-1386, April 1, 2001.

Němec F., Santolík O., Parrot M. and Berthelier J.J. (2008). Spacecraft observations of electromagnetic perturbations connected with seismic activity, Geophys. Res. Lett., 35, L05109; doi: 10.1029/2007GL032517.

Massonnet D., Rossi M., Carmona C., Adragna F., Peltzer G., Feigl K. and Rabaute T. (1993): The displacement field of the Landers Earthquake mapped by radar interferometry. *Nature*, 364, 138-142.

Lu Z., Kwoun O., and Rykhus R.: Interferometric Synthetic Aperture Radar (InSar): Its Past, Present and Future. Photogrammetric Engineering & Remote Sensing, March 2007 (217-221).

Zoran Maria (2009): Earthquake precursors assessment in Vrancea area, Romania by satellite and Geophysical in-situ data.

Fang Z., Deng M., Qian J., Yin J., Geng N., Liu X., Fan Z. and Jing H.: Study on the application of passive microwave remote sensing technology to Earthquake prediction and its physical mechanisms.

Shake Sally N. and McHone J. Gregory (1986): Topographic Lineaments and their Geologic significance in central New England and adjacent New York.
Saraf A.K. and Choudhury S.: Thermal remote sensing technique in the study of pre-Earthquake thermal anomalies, J. Ind. Geophys. Union, 9 (3), 197–207, 2005c.

Ouzounov D., Liu D., Chunli K., Cervone G., Kafatos M. and Tylor P.: Outgoing long wave radiation variability from IR satellite data prior to major Earthquakes. Tectonophysics 431 (2007) 211-220.
Guo X., Zhang Y., Zhong M., Shen W. and Wei C.: Variation characteristics of OLR for the Wenchuan Earthquake, Chinese J. Geophys., 53 (6), 980–988, 2010.

Singh R.S., Dey S., Bhoi S., Sun D., Cervone G. and Kafatos M.: Anomalous increase of chlorophyll concentrations associated with Earthquakes. Advances in Space Research 37 (2006) 671-680.

Jones, V.T. and Drozd, R.J. (1983) Predictions of Oil or Gas Potential by Near Surface Geochemistry. AAPG Bull. Vol. 67, No. 6, p. 932-952.

Qiang Z.J., Xu X.D. and Dian C.G.: Thermal infrared anomaly precursor of impending Earthquakes, Chinese Sci. Bull., 36(4), 319–323, 1991.

Tramutoli V., Di Bello G., Pergola N. and Piscitelli S.: Robust satellite techniques for remote sensing of seismically active areas, Ann. di Geofis., 44(2), 295–312, 2001.

Tramutoli V., Cuomo V., Filizzola C., Pergola N. and Pietrapertosa C.: Assessing the potential of thermal infrared satellite surveys for monitoring seismically active areas: The case of Kocaeli (İzmit) Earthquake, August 17, 1999, Remote Sens. Environ., 96(3-4), 409–426, doi:10.1016/j.rse.2005.04.006, 2005.

Tramutoli V., Aliano C., Corrado R., Filizzola C., Genzano N., Lisi M., Martinelli G. And Pergola N.: On the possible origin of thermal infrared radiation (TIR) anomalies in Earthquake prone areas observed using robust satellite techniques (RST), Chem. Geol., 339, 157–168, doi:10.1016/j.chemgeo.2012.10.042, 2013.

Pulinets S. and Ouzounov D.: Lithosphere-Atmosphere-Ionosphere Coupling (LAIC) model – An unified concept for Earthquake precursors validation. Journal of Asian Earth Sciences 41 (2011) 371-382.

Freund, F. T.: Pre-Earthquake signals – Part I: Deviatoric stresses turn rocks into a source of electric currents, Nat. Hazards Earth Syst. Sci, 7, 535–541, 2007a.

Ouzounov D. and Freund F.: Mid-infrared emission prior to strong Earthquakes analyzed by Remote sensing data. Advances in Space Research 33 (2004) 268-273.

Freund Friedmann T., Kulahci Ipec G. Cyr G., Ling J., Winnick M., Tregloan-Reed J. and Freund Minoru M.: Air ionization at rock surfaces and pre-Earthquake signals. Journal of Atmospheric and Solar-Terrestrial Physics 71 (2009) 1824-1834.

Pulinets, S. A.: Lithosphere-Atmosphere-Ionosphere Coupling (LAIC) model. in Electromagnetic Phenomena Associated with Earthquakes, in Transworld Research Network, edited by M. Hayakawa, pp. 235–254, Kerala, India., 2009.

Freund F.: Pre-Earthquake signals: Underlying physical processes. Journal of Asian Earth Sciences 41 (2011) 383-400.

Gorny, V. I., Salman, A. G., Tronin, A. A. and Shilin, B. B.: The Earth outgoing IR radiation as an indicator of seismic activity, in Proceeding of the Academy of Sciences of the USSR 301, pp. 67–69., 1988.Qiang, Z. J., Dian, C. G., Wang, X. J. and Hu, S. Y.: Satellite Thermal Infrared Anomalous Temperature Increase and Impending Earthquake Precursor, Chinese Sci. Bull., 37(19), 1642–1646, 1992.

Qiang Z., Xu X. and Dian C.: Thermal Infrared Anomaly Precursor of Impending Earthquakes. Pure and Applied Geophysics 149 (1997) 159-171.

Tronin Andrew A., Hayakawa M. and Molchanov Oleg A.: Thermal IR satellite data application for Earthquake research in Japan and China. Journal of Geodynamics 33 (2002) 519-534.

Ouzounov D., Bryant N., Logan T., Pulinets S. and Taylor P.: Satellite thermal IR phenomena associated with some of the major Earthquakes in 1999-2003. Physics and Chemistry of the Earth 31 (2006) 154-163.

Bleier T., Dunson C., Maniscalco M., Bryant N., Bambery R. and Freund F.: Investigation of ULF magnetic pulsations, air conductivity changes, and infrared signatures associated with the 30 October Alum Rock M5.4 Earthquake. Natural Hazards and Earth System Sciences, 9, 585-603, 2009.

Piroddi L. and Ranieri G.: Night Thermal Gradient: A new Potential Tool for Earthquake Precursors Studies. An Application to the Seismic Area of L'Aquila (Central Italy). IEEE Journal of Selected Topics in Applied Earth Observations and Remote Sensing, Vol. 5, No. 1, February 2012.

Saradjian M.R. and Akhoondzadeh M (2011a).: Thermal anomalies detection before strong Earthquakes (M>6.0) using interquartile, wavelet and Kalman filter methods. Natural Hazards and Earth System Sciences, 11, 1099-1108, 2011.

S. K. Panda, S. Choudhury, A. K. Saraf & J. D. Das (2007): MODIS land surface temperature data detects thermal anomaly preceding 8 October 2005 Kashmir Earthquake, International Journal of Remote Sensing, 28:20, 4587-4596.

Tramutoli, V.: Robust AVHRR Techniques (RAT) for Environmental Monitoring: theory and applications, in Proceedings of SPIE, vol. 3496, edited by E. Zilioli, pp. 101–113., 1998.

Filizzola, C., Pergola, N., Pietrapertosa, C. and Tramutoli, V.: Robust satellite techniques for seismically active areas monitoring: a sensitivity analysis on September 7, 1999 Athens's Earthquake, Phys. Chem. Earth, 29(4-9), 517–527, doi:10.1016/j.pce.2003.11.019, 2004.

Aliano C., Corrado R., Filizzola C., Genzano N., Pergola N. and Tramutoli V.: Robust TIR satellite techniques for monitoring Earthquake active regions: limits, main achievements and perspectives. Annals of Geophysics, Vol. 51, N. 1, February 2008.

Genzano, N., Aliano, C., Corrado, R., Filizzola, C., Lisi, M., Mazzeo, G., Paciello, R., Pergola, N. and Tramutoli, V.: RST analysis of MSG-SEVIRI TIR radiances at the time of the Abruzzo 6 April 2009 Earthquake, Nat. Hazards Earth Syst. Sci., 9, 2073–2084, 2009a.

Genzano, N., Aliano, C., Corrado, R., Filizzola, C., Lisi, M., Paciello, R., Pergola, N., Tsamalashvili, T. and Tramutoli, V.: Assessing of the robust satellite techniques (RST) in areas with moderate seismicity, in Proceedings of Multitemp 2009, pp. 307–314, Mistic, Connecticut, USA, 28-30 July 2009., 2009b.

Genzano, N., Aliano, C., Filizzola, C., Pergola, N. and Tramutoli, V.: Robust satellite technique for monitoring seismically active areas: The case of Bhuj-Gujarat Earthquake, Tectonophysics, 431, 197–210, 2007.

Genzano N. (2014): Robust Satellite Techniques (RST) for seismically active area monitoring: improvements and long term validation on nine years (2004-2012) of MSG-SEVIRI TIR observations over Italy (PhD, thesis).

Corrado R., Caputo R., Filizzola C., Pergola N., Pietrapertosa C. and Tramutoli V.: Seismically active area monitoring by robust TIR satellite techniques: a sensitivity analysis on low magnitude Earthquakes in Greece and Turkey. Natural Hazards and Earth System Sciences (2005) 5: 101-108.

Bath, M.: The Seismology of Greece, Tectonophysics, 98, 165–208, 1983.

Galanopoulos, A. G. and Deliabasis, N.: 1972, Map of maximum observed intensities in Greece (period 1800-1970), Athens.

Papaioannou, C. A.: 1984, Attenuation of seismic intensities and seismic hazard assessment for the Greek and the surrounding area, PhD thesis, Univ of Thessaloniki.

Drakopoulos, J. and Macropoulos, K.: 1983, Seismicity and hazard analysis studies in the area of Greece, Publ. Seismol. Lab., Univ. of Athens 1.

Papazachos C.B., Kiratzi A.A., and Papazachos B.C.: Rates of active crustal deformation in the Aegean and the surrounding area. J. Geodynamics Vol. 16, No. 3, pp. 147-179, 1992.

Papazachos B.C., Kiratzi A.A., Hatzidimitriou P.M. and Rocca A.C.: Seismic faults in the Aegean area. Tectonophysics, 106 (1984) 71-85.

Papazachos B.C.: Seismicity of the Aegean and surrounding area. Tectonophysics, 178 (1990) 287-308.

Papaioannou, Ch. A. and Papazachos, B. C.: Time-Independent and Time-Dependent Seismic Hazard in Greece Based on Seismogenic Sources, Bull. Seism. Soc. Am., 90, 1, 22–33, 2000.

Tsapanos, T.M., Mantyniemi, P. and Kijko, A., (2004). A probabilistic seismic hazard assessment in Greece and the surrounding region including site-specific considerations. Annals of Geophysics, 47 (6), 1675–1688.

Papadopoulos, G., Ganas, A., and Pavlides, S. The problem of seismic potential assessment: Case study of the unexpected Earthquake of 7 September 1999 in Athens, Greece. Earth Planets Space, pgs. 9-18, vol. 54, 2002.

Papazachos, B.C., Papazachou, C.B., 1997. The Earthquakes of Greece. Ziti Publ., Thessaloniki, Greece, 304 pp.

Burton P.W., Xu Y., Qin C., Tselentis G.A. and Sokos E.: A catalogue of seismicity in Greece and the adjacent areas for the twentieth century. Tectonophysics 390 (2004) 117-127.

Pietrapertosa, C., Pergola, N., Lanorte, V. and Tramutoli, V.: Self adaptive algorithms for change detection: OCA (the one-channel cloud-detection approach) an adjustable method for cloudy and clear radiances detection, in Technical Proceedings of the Eleventh International (A)TOVS Study Conference (ITSC-XI) Budapest, Hungary, 20-26 September 2000, Bureau of Meteorology Research Centre, edited by J. D. (Eds. . Le Marshall, J.F., Jasper, pp. 281–291, Melbourne, Australia., 2001.

Cuomo, V., Filizzola, C., Pergola, N., Pietrapertosa, C. and Tramutoli, V.: A self-sufficient approach for GERB cloudy radiance detection, Atmos. Res., 72, 39–56, 2004.

Dobrovolsky, I. P., Zubkov, S. I. and Miachkin, V. I.: Estimation of the size of Earthquake preparation zones, Pure Appl. Geophys. PAGEOPH, 117, 1025–1044, doi: 10.1007/BF00876083, 1979.

WEBSITES

USGS: http://earthquake.usgs.gov/learn/kids/eqscience.php

EUMETSAT: http://www.eumetsat.int/website/home/Satellites/index.html

The Berkeley course in applied geophysics: http://appliedgeophysics.berkeley.edu/

National Academy of Sciences, 1966: http://www.pnas.org

NASA: http://www.nasa.gov/

List of figures

List of tables

Annex 1

The following figures represent TIR anomalies sequences in relation with Earthquake. Thermal anomalies (i.e. pixels with RETIRA≥4) are depicted in different colors, while clouds, no data pixels and Earthquake epicenter as shown in the legend below. The grid on the maps is 1º, black lines represent the main faults, dashed lines the boundaries and the buffer follows the magnitude range as reported above. The number of each TIR sequence follows the table 4.1 shown above.

Figure 4. 15 ***Sequence 18*** *– 26, 27, 29/06/2007 - Thermal anomalies over Peloponnesus*

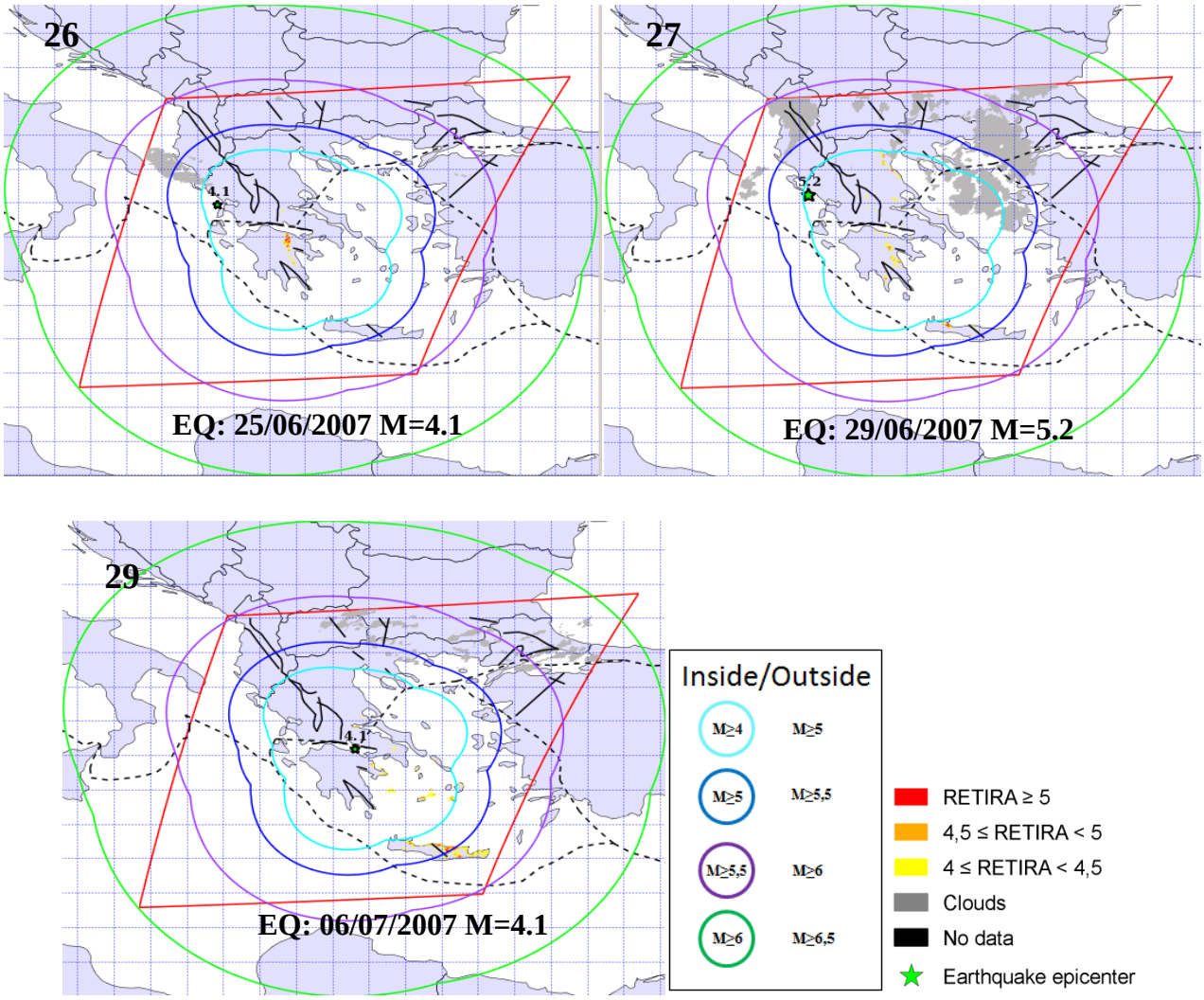

Figure 4. 16 **Sequence 19** - 27, 29/06/2007 - Thermal anomalies over Crete

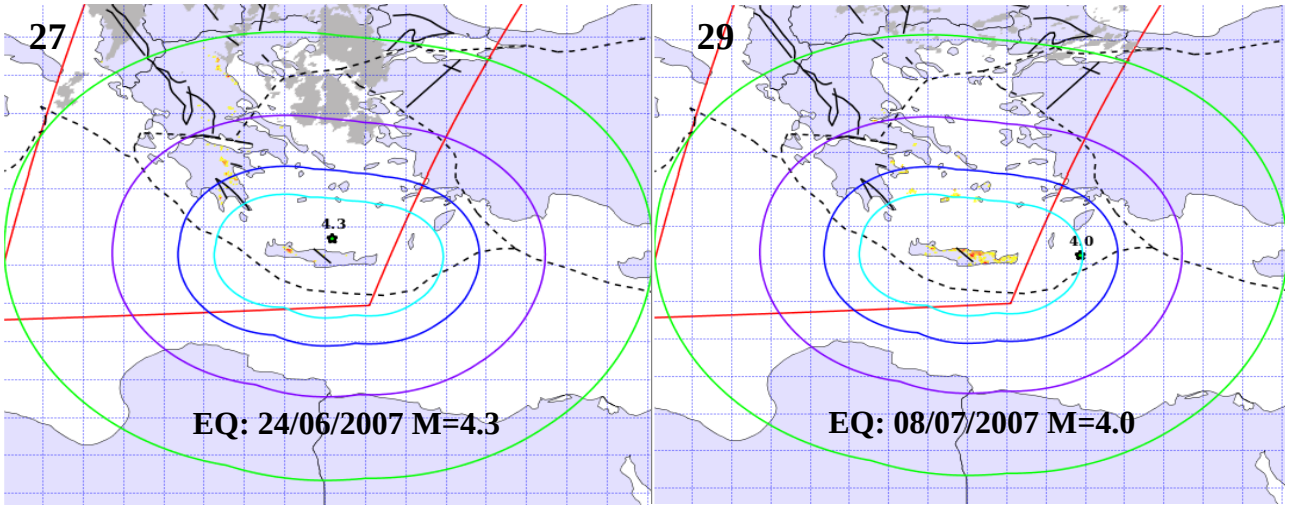

Figure 4. 17 ***Sequence 28*** *- 9, 16, 23/07/2008 - Thermal anomalies over Sterea Ellada*

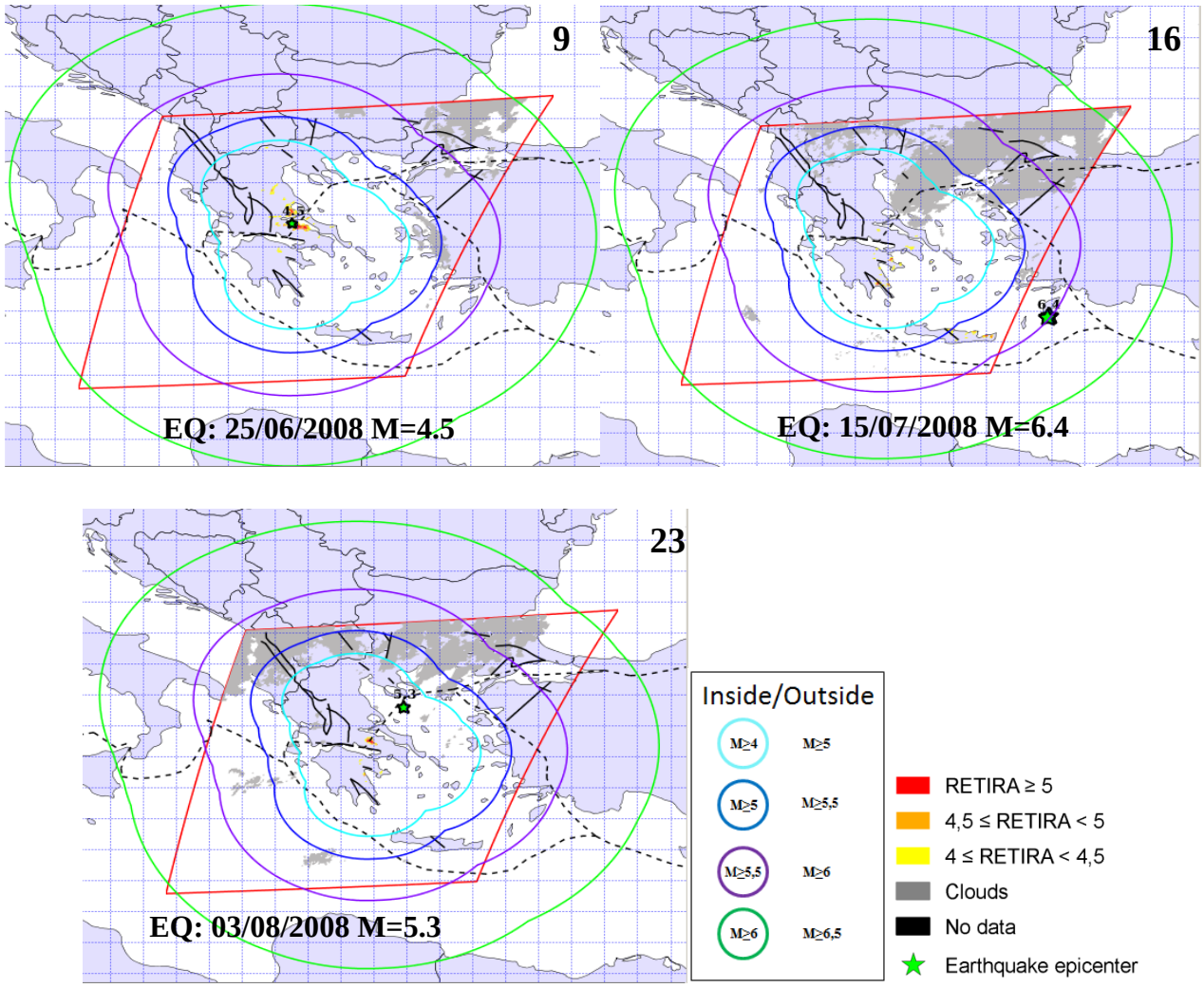

Figure 4. 18 ***Sequence 55*** *- 13, 18, 21/12/2005 - Thermal anomalies over Med Ridge*